EXPERIMENTAL STUDY OF SURFACE DISSOLUTION FEATURES ON KIMBERLITE INDICATOR MINERALS

Elizabeth M. McIsaac

Submitted in Partial Fulfilment of the Requirements
For the Degree of Bachelor of Sciences, Honours
Department of Earth Sciences
Dalhousie University, Halifax, Nova Scotia
April 2009

DALHOUSIE UNIVERSITY
Inspiring Minds

Department of Earth Sciences
Halifax, Nova Scotia
Canada B3H 4J1
(902) 494-2358
FAX (902) 494-6889

DATE: April 24, 2009

AUTHOR: Elizabeth M. McIsaac

TITLE: Experimental Study of Surface Dissolution Features on Kimberlite Indicator Minerals

Degree: BSc Convocation: May Year: 2009

Permission is herewith granted to Dalhousie University to circulate and to have copied for non-commercial purposes, at its discretion, the above title upon the request of individuals or institutions.

Signature of Author

ABSTRACT

Kimberlite magmas entrain mantle minerals, including chromites, ilmenites, garnets and diamonds, during their ascent to the Earth's surface. Kimberlite magma partially dissolves these minerals during their ascent producing characteristic surface features. Previous studies established that diamond surface features can be used to infer the chemical composition of magmatic fluid. Similarly, an examination of more complex mantle minerals, such as chromites and ilmenites, could provide additional information on the chemical composition of fluid systems in magmas. The purpose of this study was to experimentally investigate the dissolution of chromites and ilmenites in melts with C-O-H fluid. Natural mineral grains were manually rounded and placed in a synthetic mixture of Ca-Mg-Si-C-H-O with 0, 5, 13, 15, and 31% (w/w) H_2O, and 0, 5, and 27% (w/w) CO_2. The surface features produced under these conditions were compared to the surface features on naturally-occurring minerals recovered from kimberlites. High pressure experiments were conducted using a piston-cylinder apparatus (1350-1400°C and 1 GPa). Scanning electron microscopy was used to evaluate the surface features on the resulting product. Angular step-like dissolution surfaces common among natural kimberlitic chromites were only observed in the presence of an H_2O-rich fluid phase. The reaction between chromite and dry melt resulted in the smoothing of chromite surfaces. Chromite dissolution in CO_2-rich melts produced rounded and polyhedral relief features, which are not typical for natural kimberlite-hosted chromite grains. Ilmenite underwent rapid dissolution under our experimental conditions. In H_2O-rich fluid, ilmenite adopted "pyramidal" surface features previously described as the most common surface feature for naturally-occurring kimberlitic ilmenites. A comparison to natural minerals recovered from Misery and Grizzly kimberlites (NWT, Canada) revealed that Misery chromites and ilmenites possess features similar to those produced experimentally in the presence of H_2O-rich fluid. This statement is supported by recent data comparing the surface features of diamonds in H_2O-rich fluids to those of Misery diamonds. The surface features of Grizzly chromites were unlike any observed in our experiments and warrant further investigation. This study supports the hypothesis that xenocrystic minerals surfaces can provide information about the composition of volatiles in mantle-derived magmas. These results suggest that kimberlites that contain chromites that show angular step-like surfaces indicate the presence of an H_2O-rich fluid during emplacement, and may be associated with high quality diamonds.

Key Words: kimberlite, chromite, ilmenite, magmatic fluid, surface features

TABLE OF CONTENTS

TABLE OF TABLES

TABLE OF FIGURES

ACKNOWLEDGEMENTS

I would like to express thanks to my supervisor, Dr. Yana Fedortchouk, for her guidance and support in this project; to thank Luke and Ashley Hilchie for their help with many aspects of this project; to Dr. Dan MacDonald for his electron microprobe expertise; to Pat Scallion for her endless help with the scanning electron microscope; to Dr. John Gosse and Guang Yang for use of their facilities and hydrofluoric acid; to V.P. Afanasiev, N.N. Zinchuk, and N.P. Pokhilenko for the use of their images of mineral grains; to NSERC for funding, and to BHP Billiton for mineral concentrates. Finally, I would like to thank Dr. Jacob Hanley for his extensive revision of this manuscript, and his numerous suggestions concerning methods and future work.

CHAPTER 1

INTRODUCTION

1.1 General Information

Kimberlites are volcanic igneous rocks, ultramafic in composition, and derived from the mantle (Winter 2001). They are believed to be rich in volatiles such as CO_2 and H_2O, which contribute greatly to their explosive emplacement (Dawson 1980). These rocks represent a small portion of the material present at the Earth's surface, but much attention is given to them because of their economic importance. Kimberlites transport diamonds and other mantle derived xenocrysts from depths of 100-300 km to the surface of the Earth. Kimberlite eruptions are one of the only ways to sample mantle material (Dawson 1980; Scott Smith 1996). Kimberlitic magmas rapidly ascend from the mantle source. Emplacement at Earth's surface takes only hours or days (Canil and Fedortchouk 1999; Kelley and Wartho 2000).

1.2 Kimberlite Mineralogy

Mineralogically, kimberlites are very complex due to the nature of their emplacement. There are four mineral sources in kimberlite: mantle xenocrysts, crustal xenocrysts, products of crystallization from the primary melt, and secondary minerals produced during alteration. Kimberlites that occur in the same geographic region can vary widely in bulk composition (Scott Smith 1996), but generally have similar textures. Most kimberlites consist of macrocrysts and megacrysts in an aphanitic groundmass. Since kimberlites have several mineral sources, the terms macrocryst and megacryst are

used specifically so that a genetic interpretation is not specified during the mineralogical description (Scott Smith 1996).

The mega/macrocryst assemblage includes olivine, magnesian ilmenite, Cr-poor titanian pyrope, phlogopite, enstatite, and Ti-poor chromite. The phases from primary crystallization include monticellite, phlogopite, perovskite, spinel, apatite, calcite and minor dolomite, and serpentine. Olivine is commonly altered to serpentine. Close to the surface, clinopyroxene and diopside can form, as the upper crust causes extensive silica contamination of the ascending melt (Mitchell 1996a; Scott Smith 1996).

Many hypotheses propose that kimberlites form from the partial melting of the mantle. If so, there must be a significant proportion of xenocrystic olivine to account for the extremely high MgO content (Kopylova et al. 2007). Currently, there is no way to accurately determine the primary melt composition of kimberlite, due to the extensive contamination and alteration it experiences during emplacement.

1.3 Kimberlite Occurrence

Worldwide kimberlite distribution, shown in Figure 1.1a, includes pipes in Southern and Western Africa, Siberia, India, Australia, Northern Canada and Greenland, South-West U.S.A., Western Europe, Argentina, and Brazil (Dawson 1980). The distribution of kimberlites in Canada is shown in Figure 1.1b.

Kimberlites occur only in continental intraplate settings, and often within cratons. Cratons are rigid and stable, and form as a combination of very old rocks (>2.4 Ga) and deformed younger rocks (<1 Ga). Cratons show minimal mineralogical and structural changes from plate tectonics (Mitchell 1986). Group 2 kimberlites and diamondiferous

Group I kimberlites ordinarily form within cratons, while barren Group 1 kimberlites may form off cratons (Mitchell 1995).

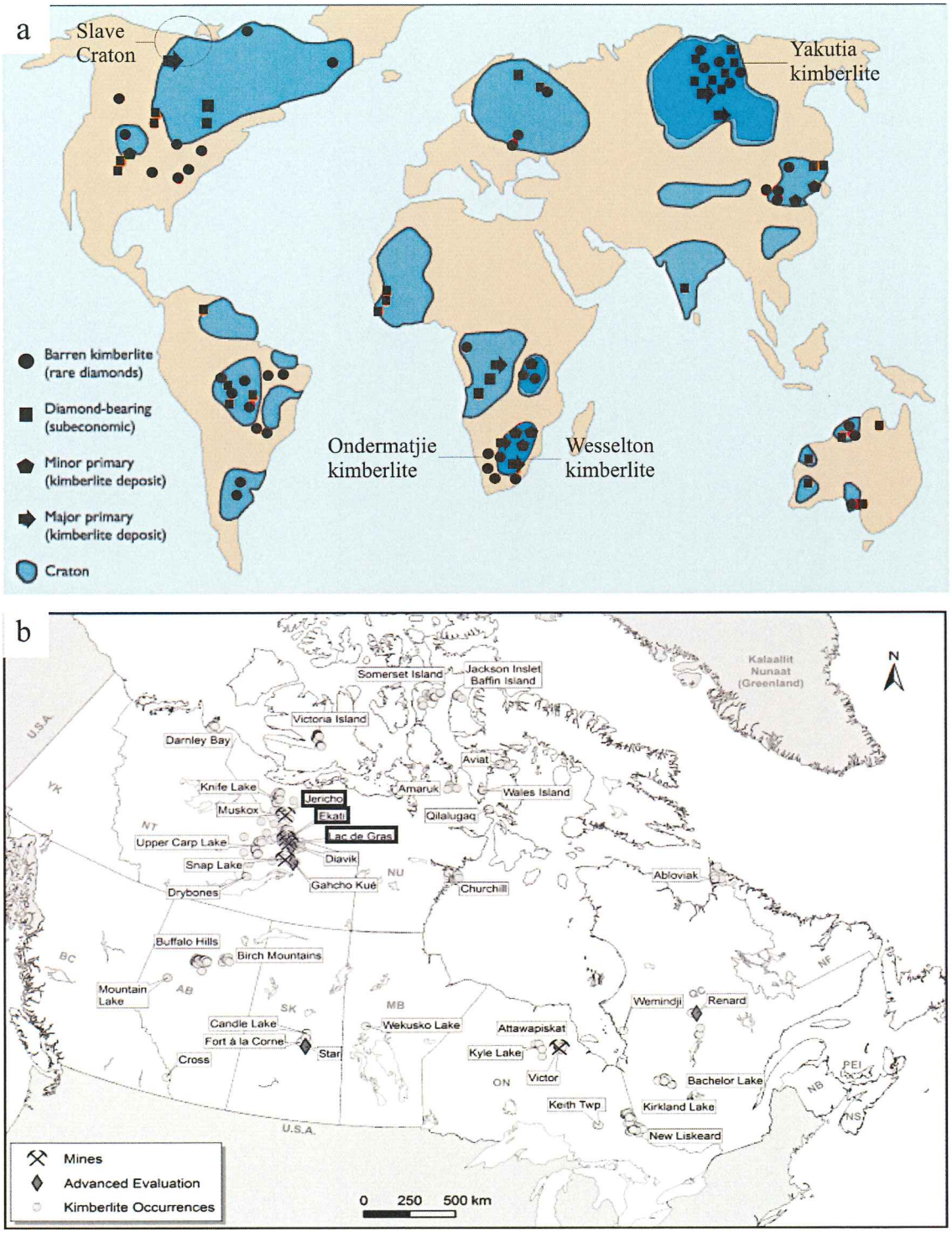

Figure 1.1a) Map showing the distribution of kimberlites worldwide after (Eckstrand 2002). b) Map showing the distribution of kimberlites in Northern Canada from (Scott Smith 2008).

1.4 Kimberlite Groups

Kimberlites are broken into two groups: Group 1 kimberlites are the most common and well studied. Group 1 kimberlites are widely distributed on and off cratons, and sample the asthenosphere during their ascent. Group 2 kimberlites, also referred to as orangeites, are less common and contain abundant mica and primary diopside. They occur almost exclusively within cratons, and do not sample below the lithosphere. The majority of Group 2 kimberlites are composed only as dikes and sills, and usually do not show diatreme and crater facies, described below, shown by many Group 1 kimberlites. Furthermore, (Mitchell 1995). Furthermore, Group 2 kimberlites have Sr isotopic compositions which are greater than, and Nd isotopic compositions which are less than bulk Earth at the time of emplacement, while Group 1 kimberlites have low amounts of radiogenic Sr and a comparatively higher amount of Nd. This is believed to be a result of magma derivation from sources isolated from the convecting mantle for greater than 1 billion years (Mitchell 1996b).

1.5 Kimberlite Facies

There are three facies in the generalized kimberlite model: the crater, the diatreme, and the root zone (Mitchell 1986). This structure is typical for kimberlites in South Africa. Each zone is structurally distinct yet part of the same overall system, although it can be difficult (in practice) to distinguish these zones. A schematic representation of this classic (Class 1) kimberlite model is provided in Figure 1.2 (Scott Smith 1996; Scott Smith 2008).

The crater facies is exposed at the surface of the Earth, and is filled with volcaniclastic kimberlite (VK), resedimented volcaniclastic kimberlite (RVK), or pyroclastic kimberlite (PK). Often volcaniclastic kimberlite contains more diamonds than other kimberlite types. The main difference between Canadian and South African kimberlites is the occurrence and preservation of this facies (Field and Scott Smith 1998).

The diatreme facies is the "carrot-shaped" zone of a kimberlite body. The diatreme underlies the crater facies, is conical and tapers downward, and terminates 1-2 km below surface. The kimberlite-country rock contacts are sharp, dip steeply at 75-80°, and show little contact metamorphism (Mitchell 1986). By definition, the diatreme is composed of tuffistic kimberlite breccia (TKB), characterized by the presence of pelletal lapilli and country rock xenoliths that are set in a fine grained inter-clast matrix (Field and Scott Smith 1998).

The root facies underlies the diatreme facies. This zone contains minerals from primary crystallization under fluid-rich conditions (Field and Scott Smith 1998). There are no pyroclastic textures present, although xenoliths of country rock may be present. Dykes and sills containing hypabyssal kimberlite (HK) are abundant in this facies (Mitchell 1986).

1.6 Emplacement Mechanism and Geology

Kimberlite structures are divided into three general classes. Class 1 kimberlites are composed of a root, diatreme, and crater facies, filled with HK, TKB and VK respectively. Class 2 kimberlites have shallowly dipping crater facies filled with VK or

PK, and Class 3 kimberlites have steep crater zones containing VK or RVK (Field and Scott Smith 1998; Skinner and Marsh 2004).

Generally, South African kimberlites are Class 1, Canadian kimberlites within the Prairies are Class 2, and Canadian kimberlites within the Slave Craton are Class 3. A schematic representation of the three classes of kimberlites is given in Figure 1.2. (Field and Scott Smith 1998; Scott Smith 2008). Class 2 and 3 kimberlites in Canada have prominent crater facies, compared with Class 1 kimberlites in South Africa that are dominated by the tuffistic kimberlite breccia in the diatreme facies. This can be attributed to the nature of formation, described below, and to the extent of weathering in each area. Canadian kimberlites have not been subjected to the extensive erosion experienced by the South African kimberlites (Field and Scott Smith 1998).

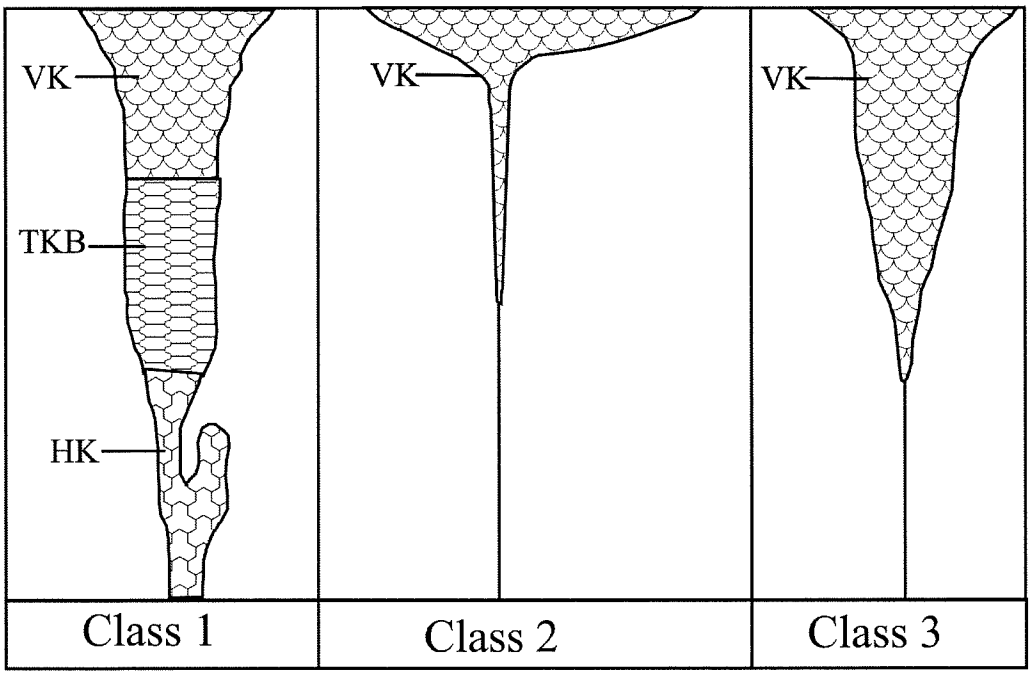

Figure 1.2 Profile of the three classes of kimberlites, after (Field and Scott Smith 1998; Scott Smith 2008). Class I consists of the root, diatreme, and crater facies filled with hypabyssal kimberlite (HK), tuffictic kimberlite breccia (TKB), and volcaniclastic kimberlite (VK), respectively. Class II consists of a shallowly dipping crater faces filled with VK. Class III consists of a steeply dipping crater facies filled with VK.

The origins of the different classes of kimberlites are currently uncertain. One hypothesis states that the content and composition of volatiles in the ascending magma dictates what type of structure is present (Skinner and Marsh 2004). A second theory states that kimberlite structure depends on the country rocks (Field and Scott Smith 1998).

The first hypothesis attributes the formation of Class 1 kimberlites to the rapid exsolution of volatiles from the melt in the hypabyssal facies. This causes an explosion which propagates downward, creating the carrot shape diatreme. This also causes fracturing of the cap rock, causing the explosive extrusion that creates the crater facies (Skinner and Marsh 2004).

Class 2 and 3 kimberlites are heavily influenced by the fluid composition of the melt. According to this view Class 2 kimberlites are formed by CO_2-rich, water-poor melts. The depth of exsolution of CO_2 is shallower that that of H_2O, so the explosion caused by exsolution will be closer to the surface. Since magma reaches shallower depths, the likelihood of phreatomagmatism due to groundwater interaction is much greater. This theory of formation is consistent with the absence of a diatreme facies in Class 2 kimberlites (Skinner and Marsh 2004).

Class 3 kimberlites have steep-sided craters, which can contain magmaclasts composed of earlier-formed hypabyssal kimberlite. Although it remains poorly explored, the hypothesis is that the melt is H_2O rich. H_2O exsolution occurs at a deeper level than CO_2, so the explosion caused by fluid exsolution will occur at a deeper depth. H_2O exsolution may also cause the deep crystallization of an initial kimberlite that will act as a

cap for later ascending magmas. This process leads to an enormous pressure build-up upon the exsolution of later volatiles, causing a large explosion and forming of a deep crater (Skinner and Marsh 2004).

In contrast, the second view considers the dominant effect on kimberlite structure to be the near surface geology and the type of the country rocks. Class 1 kimberlites form when a resistant or impermeable stratigraphic layer stops an ascending melt. As the magma accumulates, the pressure exerted by the exsolved volatiles causes the overlying rock to rupture. These rupture events propagate upwards, expanding the diameter of the diatreme, and explaining the distinctive 'carrot-shaped' appearance of this zone. The crater is formed when the final stratigraphic barrier is breached, and rapid exsolution of volatiles causes a violent explosion. In this theory, volatiles are responsible for the ascent, but the geological setting determines the overall structure of the pipe (Field and Scott Smith 1998).

The prominent crater facies of Class 2 kimberlites, typical of kimberlites located in the Canadian Prairies, is also attributed to phreatomagmatism due to melt/groundwater interaction. Thus, the occurrence of a Class 2 kimberlite should be spatially associated with an aquifer; the ideal near-surface rock type for emplacement of this class of kimberlite is poorly consolidated sediments (Field and Scott Smith 1998). It is proposed that Class 2 kimberlites form in a two-step process. The first step is a large explosion, and the second step is the infilling of the empty hole.

The second theory does not propose a method of emplacement for Class 3 kimberlites, but it is suggested that formation most likely occurs in basement rocks overlain by poorly-consolidated sediments.

To summarize, the volatile content and composition play an important role in the mechanism of magma emplacement and the structure and composition of kimberlites. To understand the nature of this rock type, it is necessary to constrain their fluid content and composition.

1.7 Constraining Parental Composition

The depth associated with kimberlite formation has not been shown to exceed 300 km (Dawson 1980). Below 300 km there should be a phase change of olivine to ringwoodite. Ringwoodite xenoliths in kimberlites have not been reported (Dawson 1980). Due to the extensive contamination between the formation of kimberlite at depth and the emplacement at Earth's surface, the primary composition of kimberlite melts are very poorly understood.

There are two main approaches used to constrain parental kimberlite composition. The first method uses experimental petrology to place compositional limits on kimberlite melts that can be created at geologically-realistic pressure, temperature and emplacement conditions. The second method of constraining parental composition of kimberlite applies analytical techniques to aphanitic kimberlites, such as Wesselton kimberlite, South Africa (Edgar et al. 1988) and Jericho kimberlite, Canada (Price et al. 2000), to determine parental magma composition. Currently, there is poor consistency between the results of these studies, even those which analyze kimberlites from the same areas.

Research in experimental petrology, using high purity oxides and carbonates, indicates that kimberlite melts can originate from the partial melting (0.6-1%) of carbonated garnet lherzolite, at 60 kb (Dalton and Presnall 1998). In this study, isobaric invariant points where liquid coexists with olivine, orthopyroxene, clinopyroxene, garnet and carbonate were determined for the CaO-MgO-Al_2O_3-SiO_2-CO_2 system.

In contrast, other experimental research on natural samples shows that the Ondermatjie Kimberlite, South Africa, was derived from high degrees of partial melting of metasomatized asthenospheric mantle, composed of carbonate veins in a lherzolite/harzburgie substrate (Mitchell 2004). Similarly, it is reported that Wesselton kimberlite, South Africa may have been derived from highly metasomatized mantle where $CaCO_3$ and olivine coexist (Edgar et al. 1988).

A method of constraining SiO_2 content in a magma by determining distribution coefficients (K_D) of Mg and Fe at pressures and temperatures of interest has been proposed (Canil and Bellis 2008). When applied to a variety of phenocrystic olivines from natural kimberlite pipes, the experimentally determined K_D for Mg-Fe exchange between olivine and melt provides the Mg/Fe ratio of the melt from which the olivine crystallized. From this data, the SiO_2 content can be determined. When this method is applied to kimberlites in the Lac De Gras area, this method suggests a SiO_2 composition of the liquid to be 10-25 mol%. In the mantle, liquid of this composition could contain up to 30 wt% CO_2, and significant CaO (Canil and Bellis 2008).

Other methods of constraining primary composition focus on analyzing the composition of aphanitic varieties of hypabyssal kimberlite. The Jericho kimberlite pipe

is located northwest of Lac De Gras, on the Slave Craton. This pipe is fresh and shows quench textures, indicating rapid cooling of the melt. This method assumes that the aphanitic assemblage represents the parental magma composition (Price et al. 2000; Kopylova et al. 2007).

This method uses an electron microprobe to measure the chemical composition. Analyses of aphanitic kimberlite from Jericho yielded a parental magma composition of 26-29.5 wt% SiO_2, ~7 wt% of FeO_T , 25.7-28.7 wt% MgO, 11.2-15 wt% CaO, 8.3-11.3 wt% CO_2, 7.6-9.4 wt% H_2O (Kopylova et al. 2007).

X-ray fluorescence was used to measure major and trace elements in the Jericho kimberlite. This method found the kimberlite to have a parental composition that contained 20-25 wt% MgO, and a CO_2 content of 10-17 wt%, 5.3-7.5 wt% H_2O, differing significantly from the previous analysis of the same kimberlite (Price et al. 2000).

The biggest flaw of this method is the assumption that the melt was able to ascend from its mantle source, without significant contamination. On its ascent, the kimberlite entrains and assimilates significant foreign material (Mitchell 2008). As the melt nears the surface its composition contains a significant amount of olivine xenocrysts. The olivine is transported by a carbonate-silicate melt which is rich in Ti and Mg, and poor in Al (Mitchell 2008). This study also indicates that the volatile content, consisting of CO_2, CH_4, and H_2O is unknown but 'high' (Mitchell 2008). This composition is interpreted to be the result of the parental melt interaction with mantle-derived lherzolite and harzburgite (Mitchell 2008).

Since there is so much uncertainty in the effects of ascent on kimberlite composition, the results from this type of analysis are inherently limited. The ongoing uncertainty regarding parental compositions of kimberlite melts was the motivation for undertaking the current project.

1.8 Experimental Petrology

A method of determining kimberlite fluid composition has been proposed, which correlates natural dissolution-features on diamonds with features experimentally produced in synthetic kimberlite melts (Fedortchouk et al. 2008). The fluid phase is the reactive medium in kimberlitic magma responsible for the formation of these surface features. The study of diamonds with experimental dissolution features has established a correlation between fluid composition and content, and the presence and morphology of surface features. These results, applied to diamonds found in natural kimberlites, can constrain the fluid composition of the kimberlite magma during emplacement (Fedortchouk et al. 2007).

The limitation of this method is that the simple chemical composition of diamonds does not allow for the correlation of the depth of their entrainment in kimberlite magma with the specific surface features recorded on diamonds. Moreover, diamonds are rare accessory minerals not found in all kimberlites (Dawson 1980). Kimberlites will entrain other minerals at different depths, thus recording different information about the composition and amount of fluid in the ascending magma. A more complete understanding of fluid and melt history will result from the examination of dissolution features of minerals with more complex chemical compositions.

1.9 Natural Surface Features

Previous studies of natural kimberlites indicate that chromites and ilmenites each have different types of dissolution surfaces produced in kimberlititc magmas (Afanasiev et al. 2001). Ilmenites exhibit 'pyramidal' surface features or 'rough' surface features, although in the examined kimberlites the 'pyramidal' features are much more pervasive. The pyramids on the surface of ilmenite are variable in size, but display the same shape (Fig. 1.3).

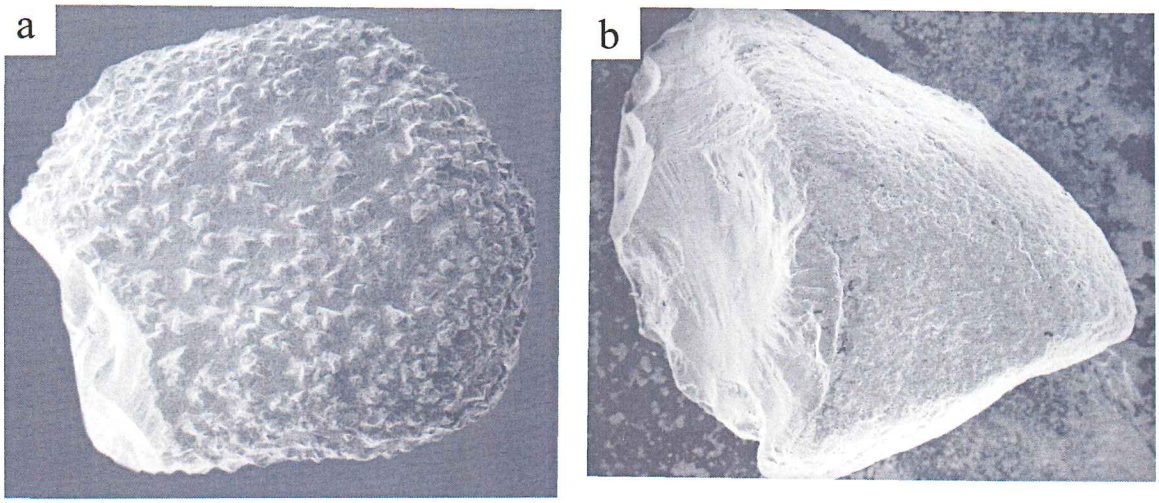

Fig 1.3. Ilmenites from Siberian kimberlites, from Afanasiev et al. 2001 a) Pyramidal surface features (75x). b) Rough surface features (50x).

Chromites also exhibit variable surface features (Afanasiev et al. 2001). The first type of surface feature is 'regular steps' which form on the edges and corners of chromite, preserving the 111 faces. The second type of surface feature is an 'irregular' type which forms on all areas of the grain (Fig. 1.4).

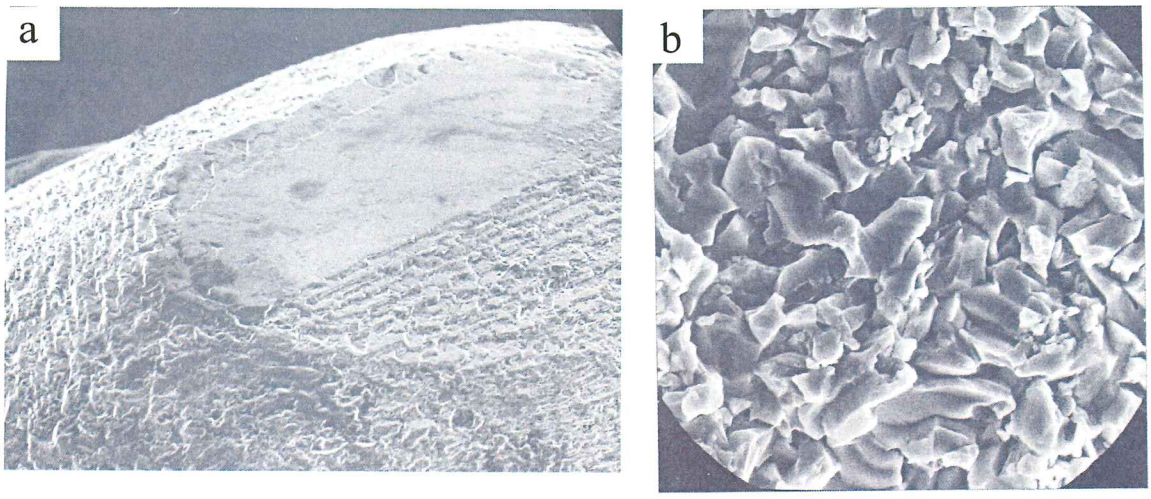

Fig. 1.4. Chromites from Siberian kimberlites, from Afanasiev et al. 2001. a) Regular step like features (180x) b) Irregular features (350x).

Based on previous studies of diamond surface features, it is proposed that these differences in surface features of chromite and ilmenite also result from differing magmatic fluid compositions. By experimentally examining the cause of the varying surface features observed in previous studies, it is possible to determine more information about the fluid composition of kimberlite magmas. Garnet forms a kelyphitic rim through the reaction with kimberlite magma, which complicates interpretation of its surface features. Furthermore, chromite was chosen for this study, because the kinetics of its dissolution in similar magmas was experimentally defined (Brearley and Scarfe 1986).

1.10 Brief Introduction to Project

This project investigates the surface features of chromite and ilmenite - mantle xenocrysts which are much more abundant in kimberlite than diamond (Mitchell 1986). Grains were selected from heavy mineral concentrates, from Misery and Grizzly kimberlites, EKATI Mine Property, NWT, Canada. These grains were imaged for naturally occurring surface features. These natural surface features were removed, and the selected grains were exposed to high pressures and temperatures, using synthetic

compositions close to diopside ($CaMgSi_2O_8$) and wollastonite ($CaSiO_3$) as kimberlite analogues. These compositions are chosen because the proportion of Ca-Mg-Si is similar to the estimates on kimberlite composition, the simple composition allows examining the effect of volatiles on the reaction, and because melting points and water solubility for these compositions are well-known.

Varying amounts of H_2O and CO_2 were included with the analogues to explore fluid behaviour and interaction with the mineral grains at the pressure and temperature conditions of kimberlite emplacement. The resulting surface features were analyzed and correlated with the content and composition of fluid used to induce the surface features. These results are then applied to natural kimberlites, to place additional constraints on fluid content and composition during emplacement. Also, these results may provide a tool for the diamond exploration industry, as diamond quality may be predicted using the morphology of kimberlite indicator minerals.

CHAPTER 2
MATERIALS AND METHODS

2.1 Grain Selection

The chromites and ilmenites used in this project were natural mineral grains, recovered from heavy mineral concentrates of exploration samples from the Misery and Grizzly kimberlites, EKATI Mine Property, N.W.T., Canada. Grains of ilmenite and chromite were selected from the concentrate under a binocular microscope, and analyzed using Energy-Dispersive Spectroscopy (EDS), on a Hitachi S-4700 FEG Scanning Electron Microscope (SEM) or a JEOL 8200 Electron Microprobe (EMP), to confirm their composition.

The chromites were grouped into three categories based on their relative proportions of chromium: high chromium (group 1), medium chromium (group 2), and low chromium (group 3). Grouping of the ilmenites was not necessary, as their compositions were much less variable. Representative EDS spectra of ilmenite and the three chromite groups are given in Figure 2.1. The naturally-occurring surface features of the selected grains were imaged using SEM; selected images can be found in Chapter 3.

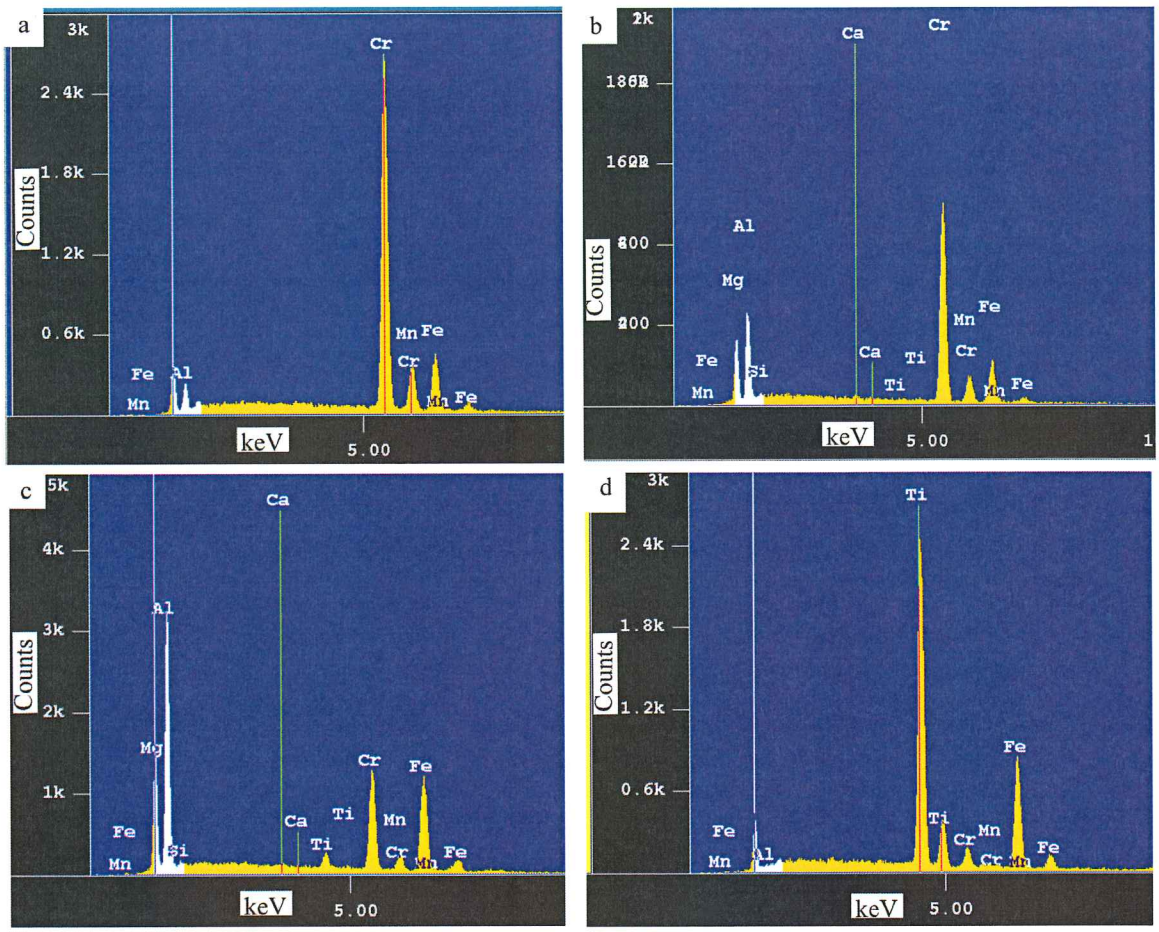

Figure 2.1 Representative Energy-Dispersive Spectra of a) Group 1 (high) chromite b) Group 2 (medium) chromite c) Group 3 (low) chromite, and d) ilmenite.

Since the goal of this study was to investigate the effect of fluids on chromite and ilmenite surface features, the naturally occurring surfaces were removed before the experiments were performed. This was achieved by buffing the grains with 320 grit Buehler-Met®II Paper Disks for 20-45 min. After this process, each grain was examined using reflected light microscopy to ensure that it was properly rounded. Also, one rounded grain was imaged using SEM, which confirmed the rounding technique was adequate. SEM images of a rounded grain are shown in Figure 2.2. For comparison, natural surface features are shown in Chapter 3.

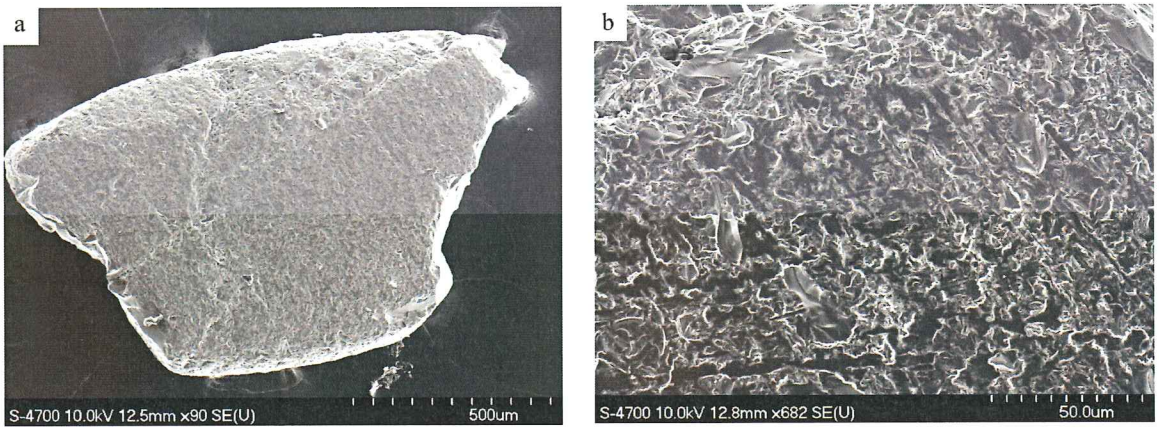

Figure 2.2 Images of a chromite grain with its natural surface features removed, in preparation for a piston-cylinder experiment. a) Low magnification image showing the full grain b) High magnification image showing an irregular surface, with no natural surface features remaining.

2.2 Melt Synthesis

2.2.1 General Information

Experiments were done in a synthetic CaO-MgO-SiO_2-H_2O-CO_2 system. The experiment capsules contained three components during the run. The first was a powdered kimberlite analogue existing above its melting point at the chosen experimental conditions that was used to approximate the chemical composition of a natural kimberlite during its ascent. It is composed of powdered oxides in the proportions corresponding to the composition of diopside or wollastonite (referred to as a diopside or wollastonite analogue). The second component was a volatile, which was added in varying proportions to the melt. Volatiles are dissolved in the melt until the reach the saturation limit to form a free fluid phase. This fluid is responsible for the explosive nature of kimberlite in a natural system (Scott Smith 1996). The final component added was a chromite or ilmenite with the naturally occurring surface features removed.

Water solubility in diopside melts is around 10 wt% for the conditions of this study (Eggler and Burnham 1984). For the starting materials volatiles were reported as

wt% added to the system regardless of forming a fluid phase or being completely dissolved in the melt (Eqn. 2.1):

wt % volatiles = [mass of volatiles / (mass of volatiles + mass of matrix)]*100% (2.1)

At the conditions of this study when H_2O is below 10 wt% in a diopside melt it is dissolved in the diopside melt. When the value of H_2O exceeds 10 wt%, a free fluid phase which is in equilibrium with the melt forms.

2.2.2 Chemical Systems Used

Table 2.1 shows the composition of each experiment. Kimberlite analogues used in this project were diopside ($CaMgSi_2O_6$) and wollastonite ($CaSiO_3$). The two fluids examined were water (H_2O) and carbon dioxide (CO_2).

2.2.3 Experiments Containing Water

Water was added using two methods. The first method used liquid water, added to the capsule before welding, using a microsyringe. When this method was used, the capsule was weighed before and after welding, to ensure no fluid was lost. The second method used the high temperature degradation of brucite to produce magnesium oxide and water, shown in Equation 2.2:

$$Mg(OH)_2 \rightarrow MgO + H_2O \quad (2.2)$$

The brucite water source was used in preference, because the risk of water loss during welding was less. However, this method was not used for water contents higher than 5 wt%, because the contribution of MgO exceeds what can be accommodated in the bulk composition of diopside. Equation 2.3 below describes the composition of

experiments PC-30, and PC-39, which contained 5 wt% H_2O. The left hand side describes the components added to the capsule before the experiment, and the right hand side describes the system after the experiment:

$$Mg(OH)_2 + MgO + CaO + 2SiO_2 \rightarrow CaMgSi_2O_6 + H_2O \quad (2.3)$$

Equation 2.4 describes the fluid/melt system used in experiments PC-29 and PC-32, which respectively examined 15 wt% and 13 wt% H_2O:

$$MgO + CaO + 2SiO_2 + H_2O \rightarrow CaMgSi_2O_6 + H_2O \quad (2.4)$$

Experiment PC-42 contained 31 wt% H_2O, the highest possible concentration allowed by the decomposition of brucite, according to Equation 2.2.

2.2.4 Experiments Containing Carbon Dioxide

The next fluid examined, CO_2, was produced by the in-situ decomposition of calcium carbonate, according to Equation 2.5:

$$CaCO_3 \rightarrow CaO + CO_2 \quad (2.5)$$

Note that all of the CaO used in this project was produced from the decomposition of $CaCO_3$. The $CaCO_3$ was heated in a Vulcan™ 3-550 oven at 900°C for 12 hours, in an open system, to drive Equation 2.5 to completion.

Experiment PC-35 contained 5 wt% CO_2 in a diopside-analogue composition, achieved by using the reaction described in Equation 2.6:

$$CaCO_3 + CaO + MgO + 2SiO_2 \rightarrow CaMgSi_2O_6 + CO_2 \quad (2.6)$$

The final system used in this project contained 27 wt% CO_2 in a wollastonite-analogue composition, the highest concentration allowed by the system described in Equation 2.7. This system was used in experiments PC-37 and PC-38:

$$CaCO_3 + SiO_2 \rightarrow CO_2 + CaSiO_3 \quad (2.7)$$

The composition and masses of chemicals used to make the above systems are indicated in Table 2.1:

Table 2.1 Synthetic Matrix Compositions

Chemical	**$CaMgSi_2O_6$ + 0 wt% fluid**	**$CaMgSi_2O_6$ + 5 wt% H2O**	**$CaMgSi_2O_6$ + 5 wt% CO_2**	**$CaSiO_3$ + 27 wt% CO_2**
SiO_2	4.1618	1.4818	0.9738	0.7504
MgO	1.3964	0.1824	0.3266	-
CaO	1.0883	0.6918	0.3368	-
$Mg(OH)_2$	-	0.4550	-	-
$CaCO_3$	-	-	0.2101	1.2499
Total mass	6.6465	2.8110	1.8473	2.0003
Fluid mass	0	0.1405	0.0924	0.5496

** all measurements in grams*

The chemicals for the synthetic melts were weighed using an analytical balance. All mixtures were ground in alcohol for 20 minutes, with mortar and pestle, to ensure complete mixing. All synthetic mixtures containing CaO were kept in glass vials wrapped in parafilm, and stored in a glass desiccator. This method was used to minimize exposure to CO_2, because Equation 2.4 is reversible, and $CaCO_3$ has greater stability than CaO. Synthetic mixtures that did not contain CaO were stored in an oven at 100°C.

The systems described above were composed of high purity chemicals from Alfa Aesar®, a supplier of research chemicals. Table 2.2 gives the specifications of each chemical:

Table 2.2 Purity of Chemicals

Chemical	Purity
$CaCO_3$	99%
MgO	99%$^+$ (metals basis)
$Mg(OH)_2$	95-100.5%
SiO_2	99.5%, 325 Mesh Powder

2.3 Reaction Assembly

Experimental pressure-temperature cells were assembled by welding a 10 mm platinum cylinder shut at one end, using a Miller Maxstar® STH welder. The rounded and ultrasonically-cleansed grain was placed in the cylinder, along with the melt of interest. Any liquid water used in the experiment was added with a micro-syringe at this point. The top of the cylinder was clamped, minimizing the free space in the capsule and welded shut, creating a closed system. This capsule was flattened at both ends using a hammer.

The welded platinum capsule was placed into a MgO holder the same length as the capsule, but larger in diameter. Two more MgO pieces were cut for the cell assembly. The first piece was placed above the capsule, and accommodated the thermocouple. The second piece was solid, and was placed below the capsule. The upper was 12 mm long, and all three pieces together were 32 mm long. A small alumina disk was placed on top of the capsule, which prevented direct contact of the Pt capsule with the thermocouple.

The pieces described above were placed inside a cylindrical graphite furnace. The experiment was heated by passing a current through this furnace. The bottom of this assembly was glued to a circular graphite base, and the furnace was placed inside a

barium carbonate ($BaCO_3$) pressure cell. The $BaCO_3$ pressure cell is chosen based on its ability to tolerate high temperatures and its high thermal insulation. Literature calls for a pressure correction of 5% for this material, because of the effect of friction (Watson et al. 2002). Pressure calibration experiments in the Fedortchouk lab using the melting of NaCl also indicate a 5% friction correction is appropriate (Fedortchouk and Hilchie). The $BaCO_3$ cell also offers a moderate oxygen fugacity buffer. Oxygen fugacity is assumed to be constant in all the experiments because the reaction assembly is the same.

The complete assembly was then wrapped in lead foil, which provided lubrication at high pressures and temperatures. Figure 2.3 shows the final assembly. The dimensions of each component are given in Table 2.3.

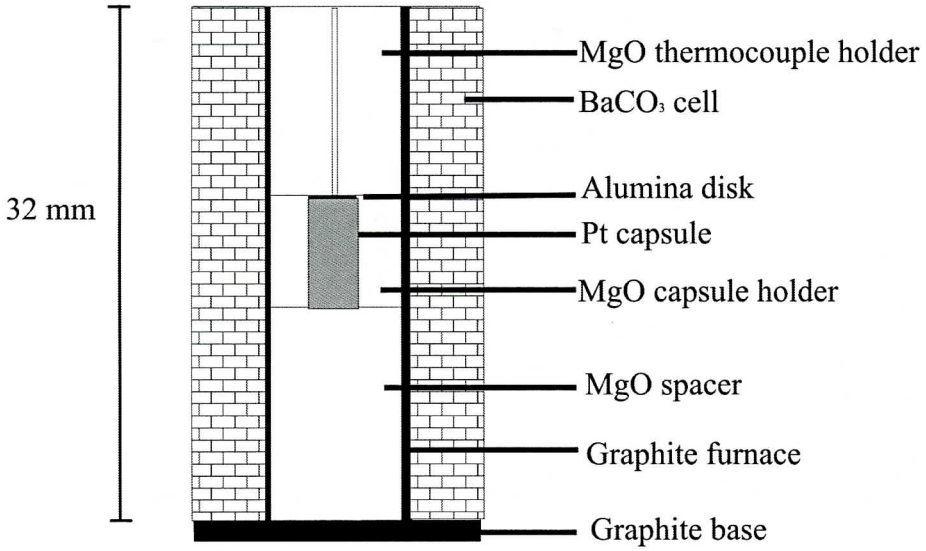

Figure 2.3 A complete reaction assembly for a piston cylinder experiment.

Table 2.3 Experiment Assembly Dimensions

Component	Height /mm	Diameter /mm
$BaCO_3$ cell	32	12
Graphite furnace	32	8
Al_2O_3 Thermocouple casing	49	1.5
MgO Thermocouple holder	12	7
MgO spacer and capsule holder	20	7
Al_2O_3 disk	1	3
Graphite base	2	11
Platinum cylinder	10	2

Temperature during the experiment was determined using a C-type thermocouple, made of $W_{5\%}Re/W_{25\%}Re$. A 49 mm alumina cylinder was used to hold the thermocouple wires. A digital wall unit converted the voltage created by the thermocouple into a temperature reading. The reading gave the temperature at the junction of the two wires, which was directly adjacent to the capsule. Thermocouples work by conversion of the voltage created at the junction of the two dissimilar metals into a temperature, using a voltmeter inserted between the two wires connecting to the wall unit. The temperature difference between the junctions is recorded because the voltage will be proportionately different (Boyer 1995).

Next, the piston-cylinder apparatus was assembled. Figure 2.5 shows the piston-cylinder apparatus. Table 2.5 contains the labels for this diagram.

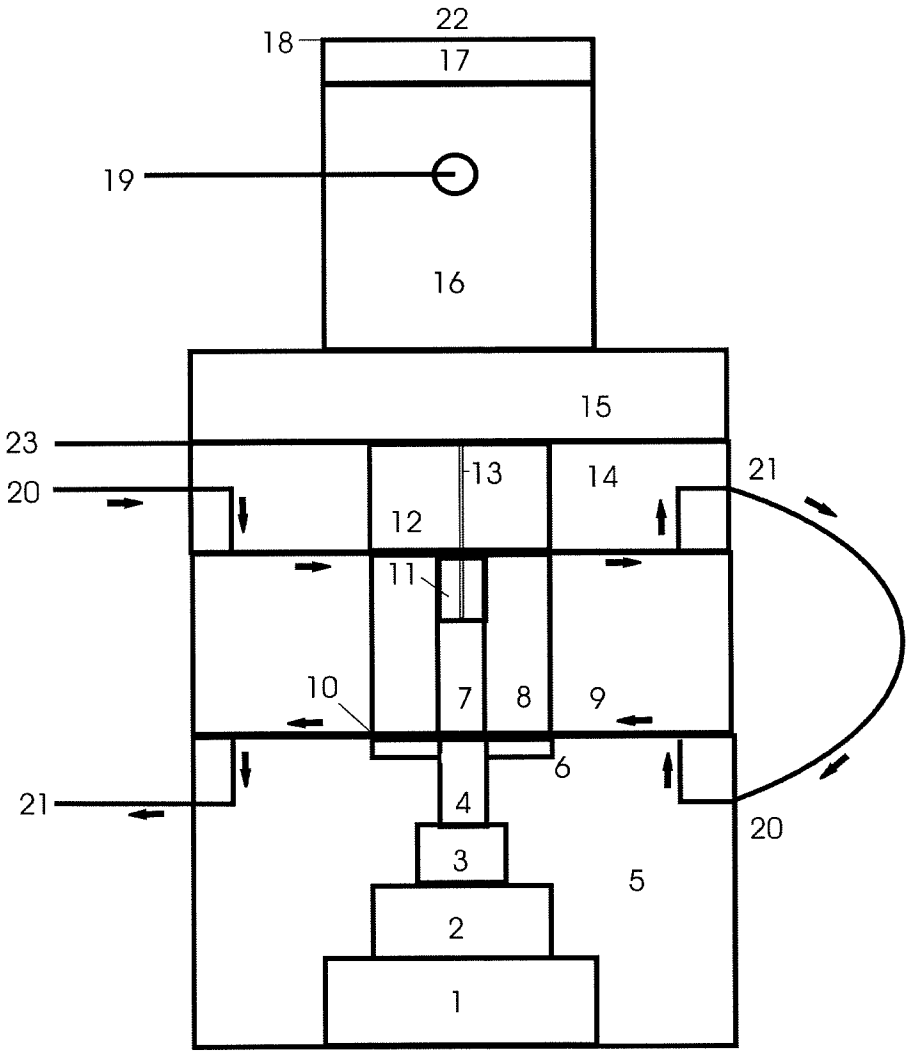

Figure 2.4 A schematic diagram of the piston cylinder apparatus, used to achieve high pressure and temperature for experiments. Table 2.4 defines the numbered pieces above.

Table 2.4 Piston Cylinder Assembly

Number	Piston Cylinder Piece	Number	Piston Cylinder Piece
1	Lower ram	13	Thermocouple
2	Main ram spacer	14	Stainless steel top plate
3	Push piece	15	Slotted thermocouple plate
4	Piston	16	End load spacer
5	Bridge	17	Upper end load spacer
6	Bridge piece	18	Mylar sheet
7	Sample cell	19	Power connection
8	WC core of pressure vessel	20	Water in
9	Stainless steel pressure vessel	21	Water out
10	Mylar sheet	22	Upper ram
11	Base plug	23	Thermocouple connection
12	WC core of top plate		

The piston cylinder apparatus was assembled by stacking several components between the upper and lower ram. The upper and lower ram were controlled by a hydraulic pump that used oil to apply pressure to the system. The upper ram stabilized the system, and prevented lateral fracture of the experimental assembly described above. The lower ram pressed upward, transferring pressure sequentially to the main ram spacer, push piece, piston, and experimental assembly. The ratio of areas from the lower ram to the piston was 100:1, so the pressure of the lower ram multiplied by 100 was the pressure exerted on the assembly at any time.

A base plug was placed on top of the experimental cell inside of the pressure vessel, and the pressure vessel was covered with the top plate. A mylar sheet was used to separate the pressure vessel from the top plate. Both the base plug and the top plate had holes which were used to accommodate the thermocouple. The thermocouple was inserted through the top plate, base plug, and MgO holder so it was in direct contact with the Al_2O_3 disk which separated the tip of the thermocouple from the platinum capsule. The thermocouple wires were held between the top plate and the slotted thermocouple plate, and were then attached to the wall unit which gave the temperature of the system. Two spacers were placed on top of the slotted thermocouple plate. The lower and larger of the two had a power connection, necessary for heating the sample. The top spacer was separated from the upper ram using another mylar sheet. The top plate and the bridge each had a water inlet and outlet, utilized when cooling the system with running water. This cooling limited the thermal expansion of the pieces surrounding the WC cores.

2.4 Experimental Procedure

After the piston-cylinder apparatus was assembled, experiments were begun. First, the upper ram was used to supply end load pressure of 0.14 kbar, and the lower ram was used to apply 2.8 kbar pressure to the assembly. At this point the system was heated to 600°C, where it remained for 6 minutes. During this time the end load was increased to its final pressure of 10 kb, plus a 5% friction correction (Watson et al. 2002). After this interval, the system was heated at 100°C/min to the final temperature. At 1000°C, and at the final temperature (1350-1400°C), the lower ram pressure was corrected to 10 kbar + 5%. Table 2.5 gives the conditions for each experiment. These conditions were chosen to simulate the near surface emplacement of kimberlites; 10 kbar corresponds roughly to 30 km depth.

After 60 minutes had elapsed, the power supply was turned off and the sample was quenched at an approximate rate of 100°C/s. The experimental capsule was then removed from the assembly and opened using pliers, or the entire capsule was cut in half using a diamond wafering saw. The reaction matrix, which for experiments PC-32, 35, 37 and 42 included a portion of the grain, was encased in a mount composed of Buehler Epoxycure Resin. All mounts were ground with a Buehler-Met®II 180 Grit Paper Disk until the reaction area of interest was exposed, then ground for 5 min each with 240 grit, and then 320 grit paper. The mount was then polished using Buehler 9, 3, and 0.1 μm diamond polishing paper. Between each of these incremental decreases in grit size, the grain mount was ultrasonically cleansed to ensure the smaller grit was not contaminated with the larger grit.

Table 2.5 Experimental Conditions

Experiment	Mineral Compositon (grain)	Melt Composition	Temperature /°C	Pressure /kbar	Heating Rate/ (°C/min)	Duration /min
PC-45	Group 3 chromite (R1aG13)	$CaMgSi_2O_6$ + 0 wt% fluid	1400	10.6	100	60
PC-30	Group 1 chromite (R1aG11)	$CaMgSi_2O_6$ + 5 wt% H_2O	1400	10.5	100	60
PC-32	Group 1 chromite (R1aG6)	$CaMgSi_2O_6$ + 13 wt% H_2O	1400	10.7	100	62
PC-29	Group 1 chromite (R1aG1)	$CaMgSi_2O_6$ + 15wt% H_2O	1350	10.6	100	63
PC-35	Group 2 chromite (R1bG14)	$CaMgSi_2O_6$ + 5 wt% CO_2	1400	10.5	100	60
PC-37	Group 2 chromite (R1bG2)	$CaSiO_3$ + 27 wt% CO_2	1400	11.2	100	61
PC-39	Ilmenite (R1aG3)	$CaMgSi_2O_6$ + 5 wt% H_2O	1400	10.4	100	61
PC-38	Ilmenite (R1aG2)	$CaSiO_3$ + 27 wt% CO_2	1400	10.5	100	61
PC-42	Ilmenite (R1aG7)	MgO + 31 wt% H_2O	1400	10.5	100	60

Experiments PC-37, 35, 32, and 45 had matrix adhered to the surface of the experimental grains that was not easily removable using tweezers. These grains were placed in concentrated hydrofluoric acid overnight to dissolve the residual matrix and recover the chromite grains.

The mounts and grains were examined using optical microscopy, SEM, and EMP. See Appendix B for EMP standards, and Appendix C for raw EMP data. SEM and optical microscopy images are given in Chapter 3. The silicate analysis uses an accelerating voltage of 15.0 kV, a 2 μm beam width, and a probe current of 1.998×10^{-8} Å. The silicate analysis is not corrected for the V-Ti signal overlap. The oxide analysis used an accelerating voltage of 15.0 kV, a 3 μm beam width, and a probe current of 1.998×10^{-8} Å. These analyses are corrected for the V-Ti and Cr-V signal overlaps.

The instruments used are a Hitachi S-4700 FEG Scanning Electron Microscope located at the Facility for Materials Characterization, which is managed by the Institute for Research in Materials, and a JEOL 8200 electron microprobe located in the Robert MacKay Electron Microprobe Laboratory. Both facilities are located at Dalhousie University.

CHAPTER 3
RESULTS

3.1 Naturally Occurring Surface Features

3.1.1 Chromite Surface Features, Misery Pipe

Many chromite grains from the Misery kimberlite showed natural surface features that resulted from dissolution in kimberlite magma. Eight of these grains were examined using SEM, and the resulting images are shown in Figures 3.1 to 3.4. There was little variation in surface features between grains from the Misery Pipe. The most common surface features on these grains were protruding angular trigons.

Naturally-formed surface features on chromite R1aG6 are shown in Figure 3.1. This chromite had a large fracture on its exposed surface, but showed natural surface features acquired during kimberlite emplacement on the non-fractured surfaces (Fig 3.1a). Surrounding the fracture were abundant surface features which were protruding, regularly-repeating, and triangular (Fig. 3.1b-e). When grains were viewed at 25 000x magnification, the early stages of development of trigonal depressions and etch pits could be observed (Fig. 3.1e,f).

Magmatic dissolution features on chromite R1aG11 are shown in Figure 3.2. Although this chromite had extensive fractures (Fig. 3.2a), the non-fractured surfaces showed abundant triangular natural surface features (Fig 3.2b-f). In Figures 3.2c-e, the same protruding triangles shown in Figure 3.1 occurred on the surface of the grain. In Figures 3.2b,d,f the triangular features laid flat against the surface of the grain.

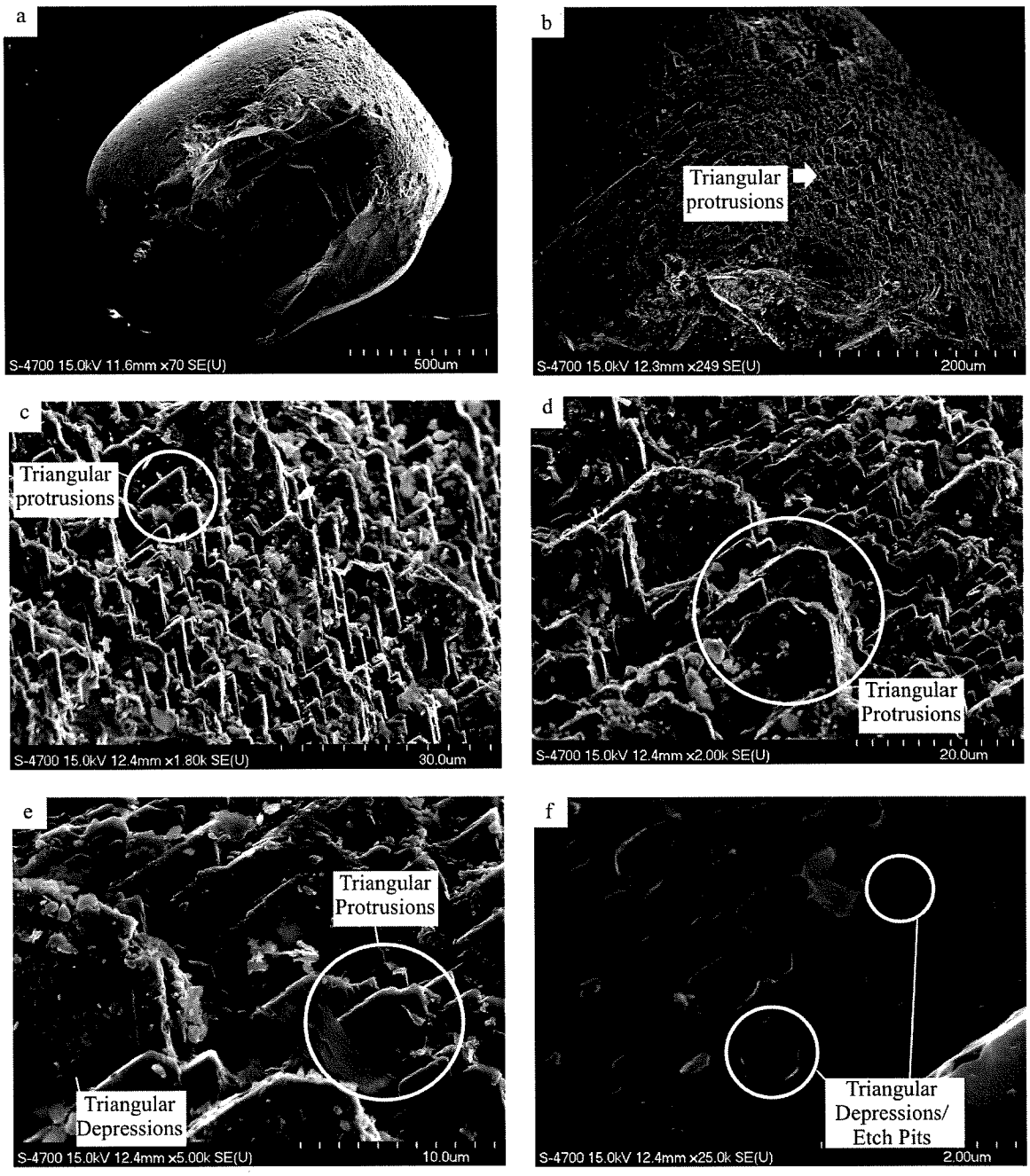

Figure 3.1 SEM Image of chromite grain R1aG6, from the Misery kimberlite a) View of the full grain. b-d) Triangular protruding surface features e)Triangular protruding surface features containing trigonal depressions. f) Development of etch pits and triangular depressions.

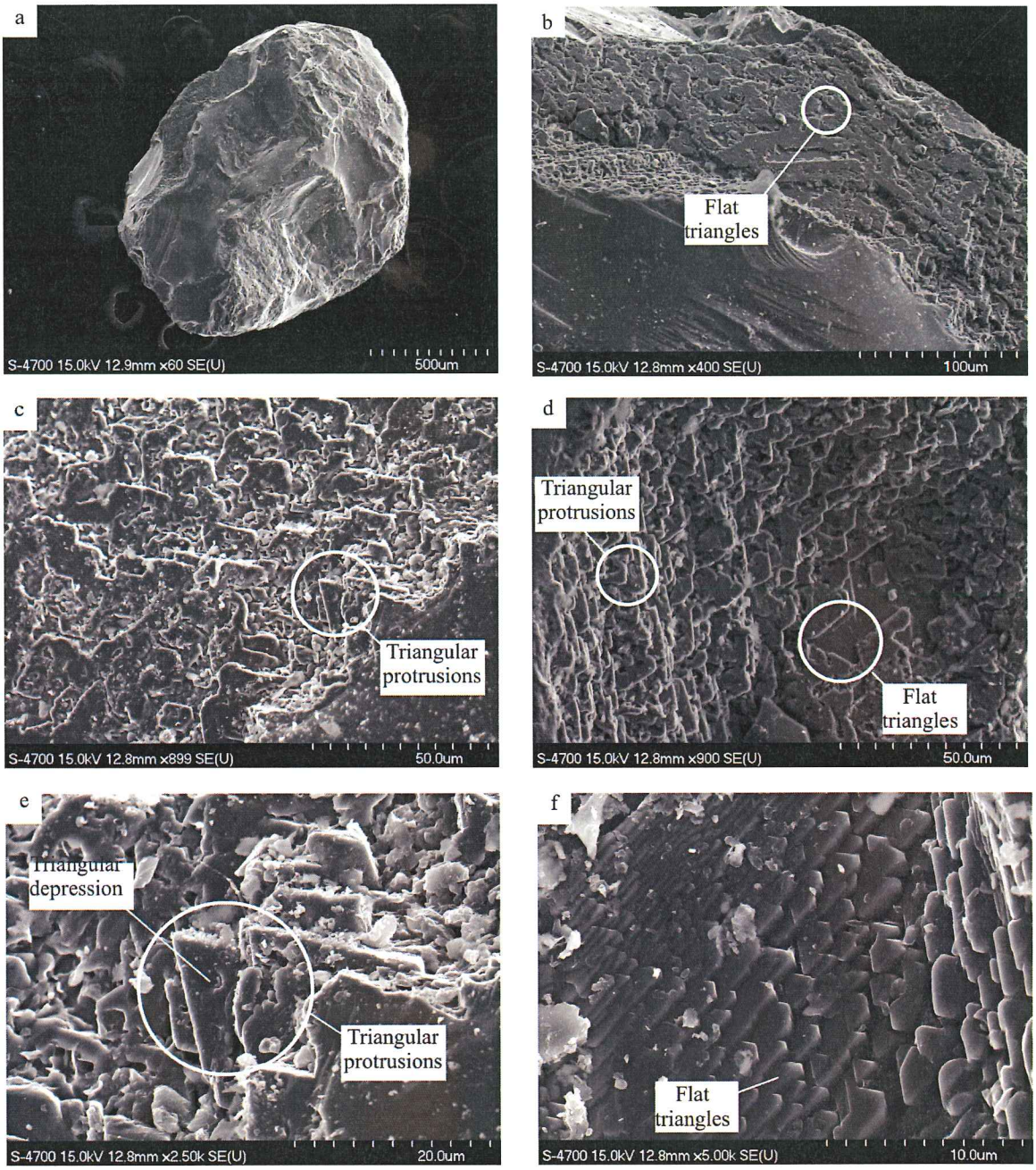

Figure 3.2 SEM images of chromite grain R1aG11, from the Misery kimberlite a) View of the full grain b) Flattened triangular surface features. c-e) Protruding triangular surface features. f) Shallow triangular surface features.

Natural dissolution features from the chromite R1bG5 are shown in Figures 3.3a-c. There was a foreign mineral grain stuck to the surface of the chromite, so this area was avoided during imaging. The natural chromite surface was preserved around the edge of the grain. This area displayed surface features which differed from the surface features on chromites R1aG11 and R1aG6. These surfaces were highly textured and more irregular than on previous grains. Figures 3.3d,e show chromite R1bG12, which also had a foreign mineral grain stuck to its surface. Images of this chromite show a surface with many protruding triangular surface features.

Images from chromite R1bG14 are shown in Figure 3.4. Figure 3.4a shows the full grain, which was extensively fractured, and Figure 3.4b shows a closer view of the grain edge which had maintained the original triangular surface features.

Images of chromite R1aG13 are contained in Figure 3.4c-e. Figure 3.4d shows protruding angular surface features on the top half of the image, and shallow triangular surface features on the bottom half. Figure 3.4e shows a closer view of the shallow triangular surface features shown in Figure 3.4d. Figure 3.4f shows more protruding triangular surface features that occurred on chromite R1bG1.

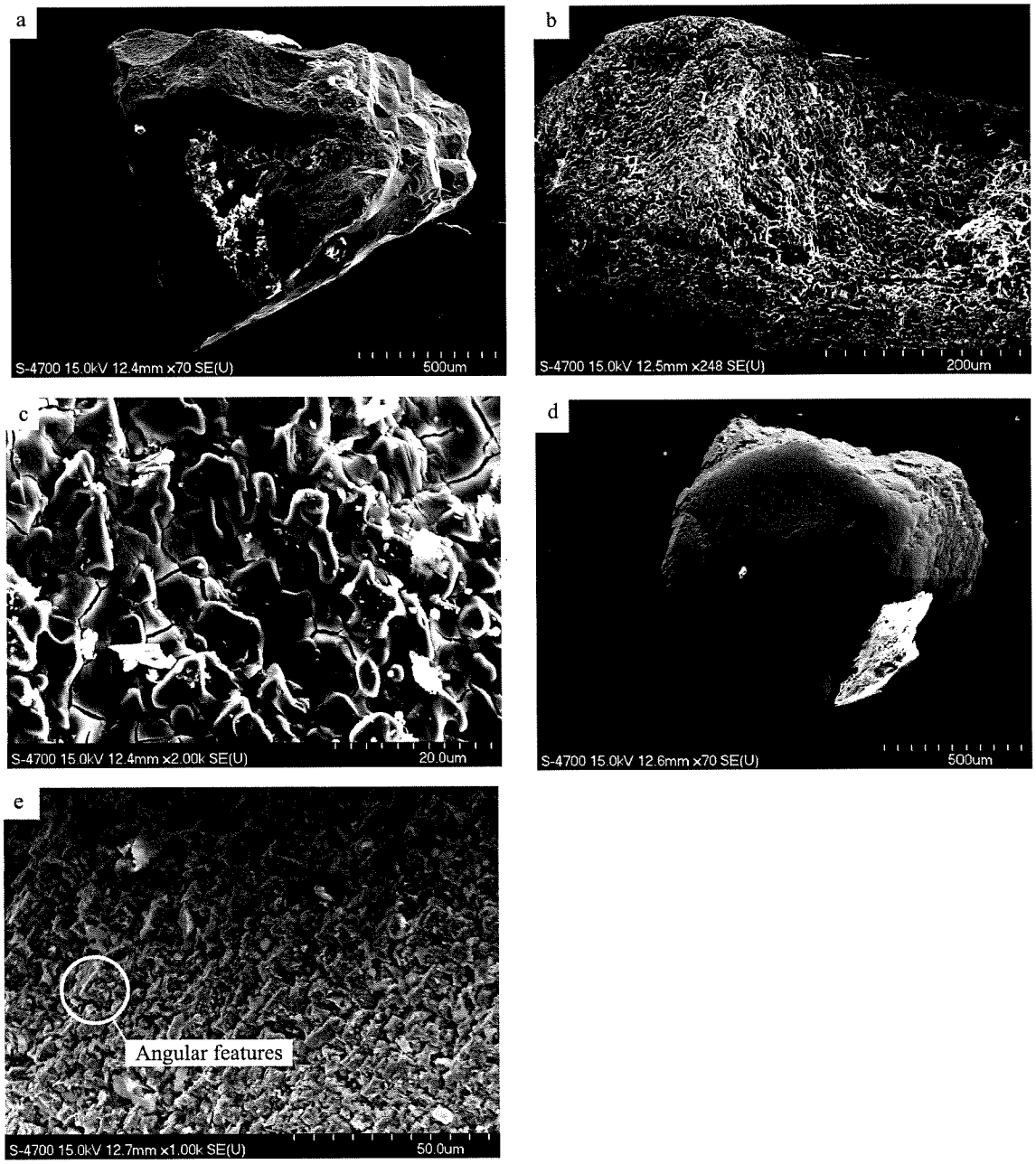

Figure 3.3 SEM images of chromite grains R1bG5 and R1bG12, from the Misery kimberlite. a) View of the grain, R1bG5. b,c) Irregular, rough surface of R1bG5. d) View of the grain, R1bG12. e) Grain R1bG12 showing irregular rough surfaces, with development of angular step-like features.

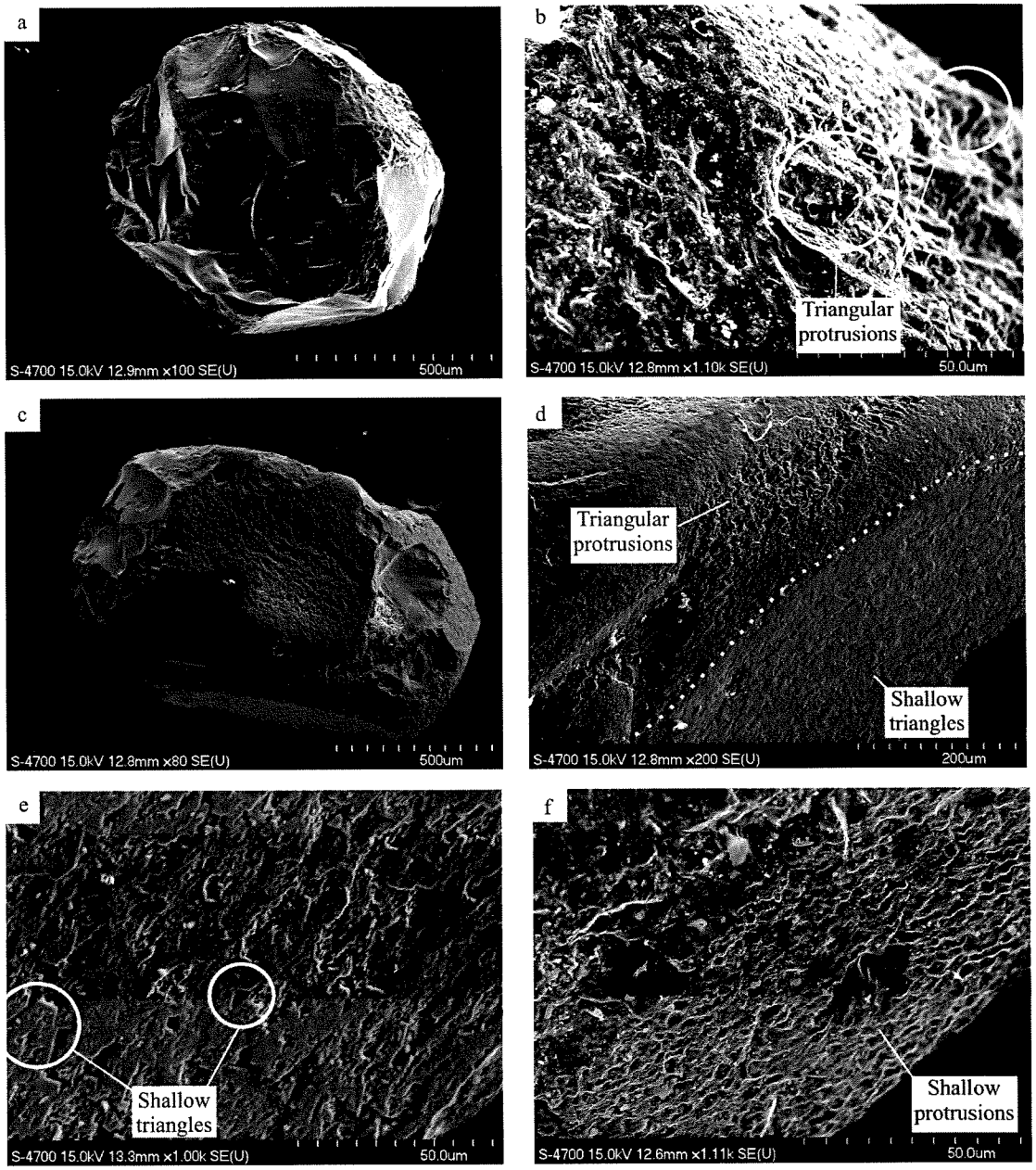

Figure 3.4 SEM images of chromite grains R1bG14, R1bG13, R1bG1, from the Misery kimberlite. a) View of the grain R1bG14. b) Protruding triangular surface features on R1bg14. c) View of the grain R1aG13. d) Protruding triangular surface features and shallow angular surface features on R1aG13. e) Shallow angular surface features on R1aG13. f) Triangular surface features on R1bG1.

3.1.2 Grizzly Pipe Chromite Surface Features

Three chromites from the Grizzly kimberlite were examined using SEM for the presence of magmatic dissolution-features (Fig. 3.5-3.7). There was significant variation in surface features among grains from the Grizzly kimberlite. In comparison to the Misery kimberlite, most Grizzly chromites had surface features which were less regular, and more rounded. Diamond data indicates that the Grizzly kimberlite had low water content at the time of emplacement (Fedortchouk et al. 2008).

Grizzly chromite G1 had a highly textured and angular surface with few ordered features (Fig. 3.5b,c,e). The features which had an ordered orientation were rare, inconsistent in size, and rounded (Fig. 3.5d-f). Chromite G2 also had an irregular surface (Fig 3.6). Some of the surface features were round, and showed repetition (Fig. 3.6c-d). In addition to the rounded surface features, some poorly-formed protruding trigons are shown in Figures 3.6e,f. Trigons are a shape with three-fold rotational symmetry, with no reference to the angularity of its apicies. Rounded trigons have rounded apicies, and triangles have angular apicies. These features were round, but the orientation and form were distinguishable. Chromite G5 (Fig. 3.7) was similar to chromite G2, in that the surface features were mostly poorly formed trigons (Fig. 3.7c-e). The surface shown in Figure 3.7f was very angular, but lacked the well-developed step-like forms observed on Misery chromites.

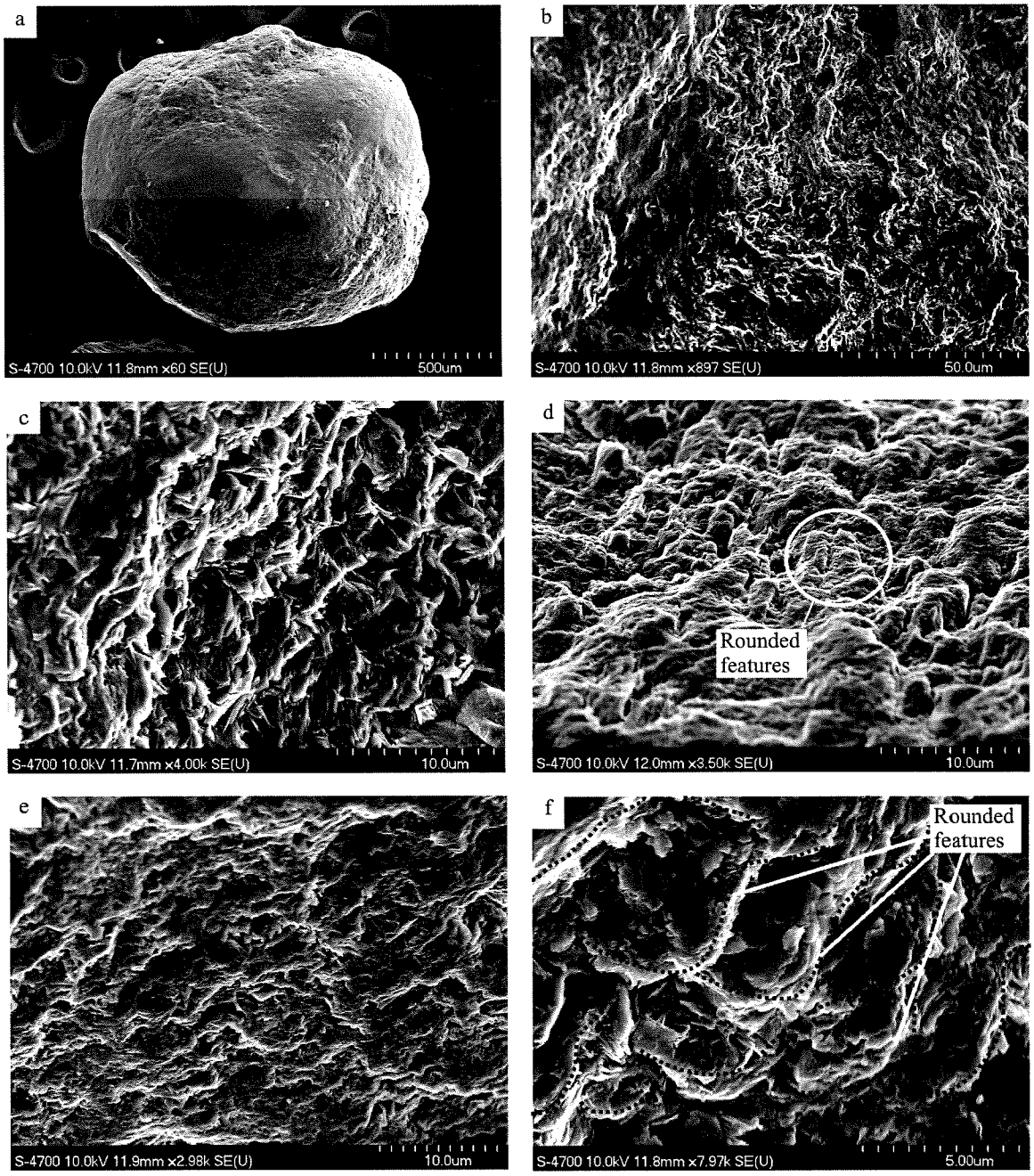

Figure 3.5 SEM images of chromite grain G1, from the Grizzly kimberlite. a) Grain G1, which had an octahedral shape. b,c) Angular, irregular surface features. d) Rounded, irregular surface features. e,f) Rounded surface features

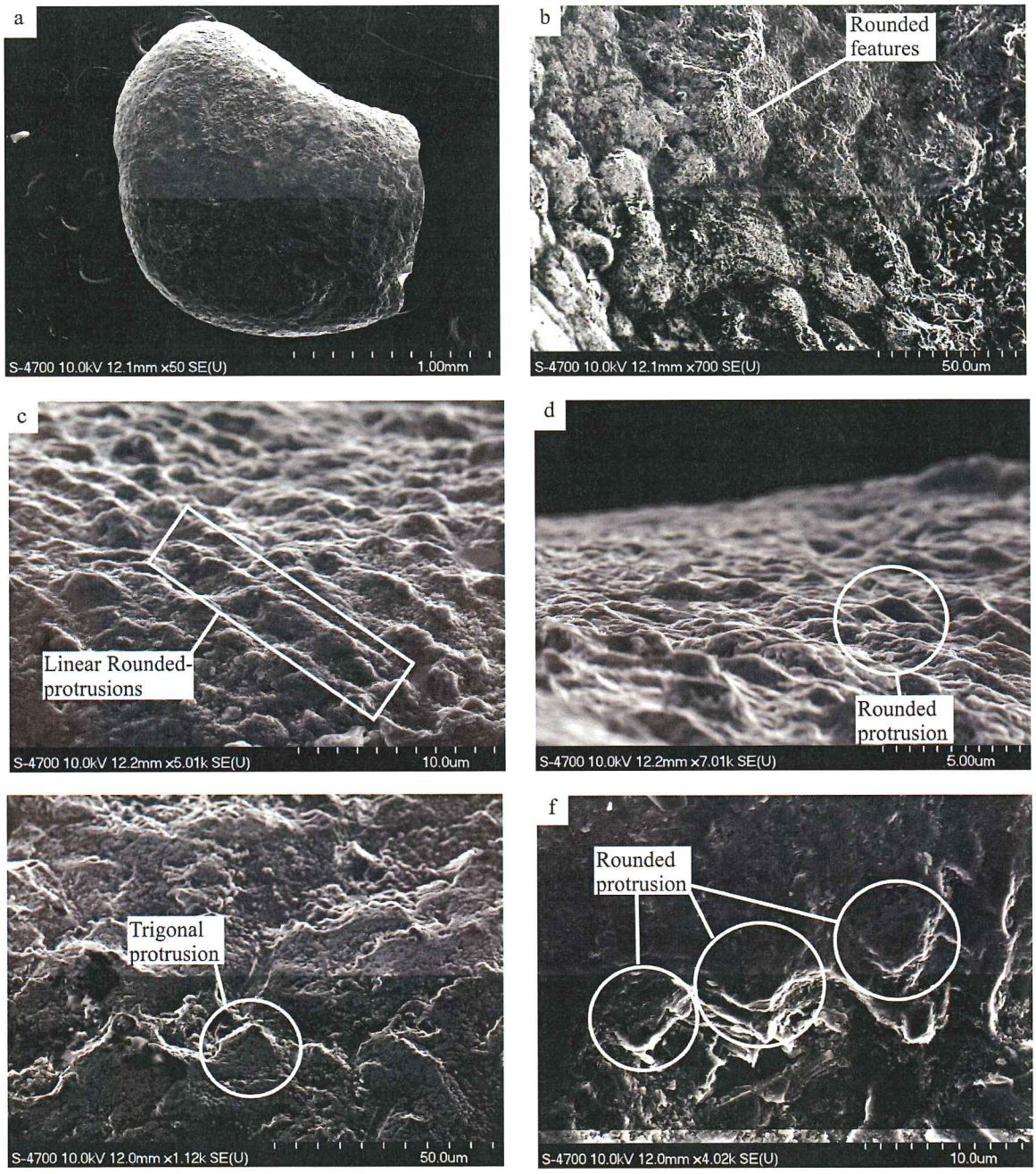

Figure 3.6 SEM images of chromite grain G2, from the Grizzly kimberlite. a) Grain G2 b) Irregular, rounded surface features c,d) Regularly-oriented, rounded surface features. e) Poorly formed trigonal surface features. f) Rounded, protruding trigonal surface features.

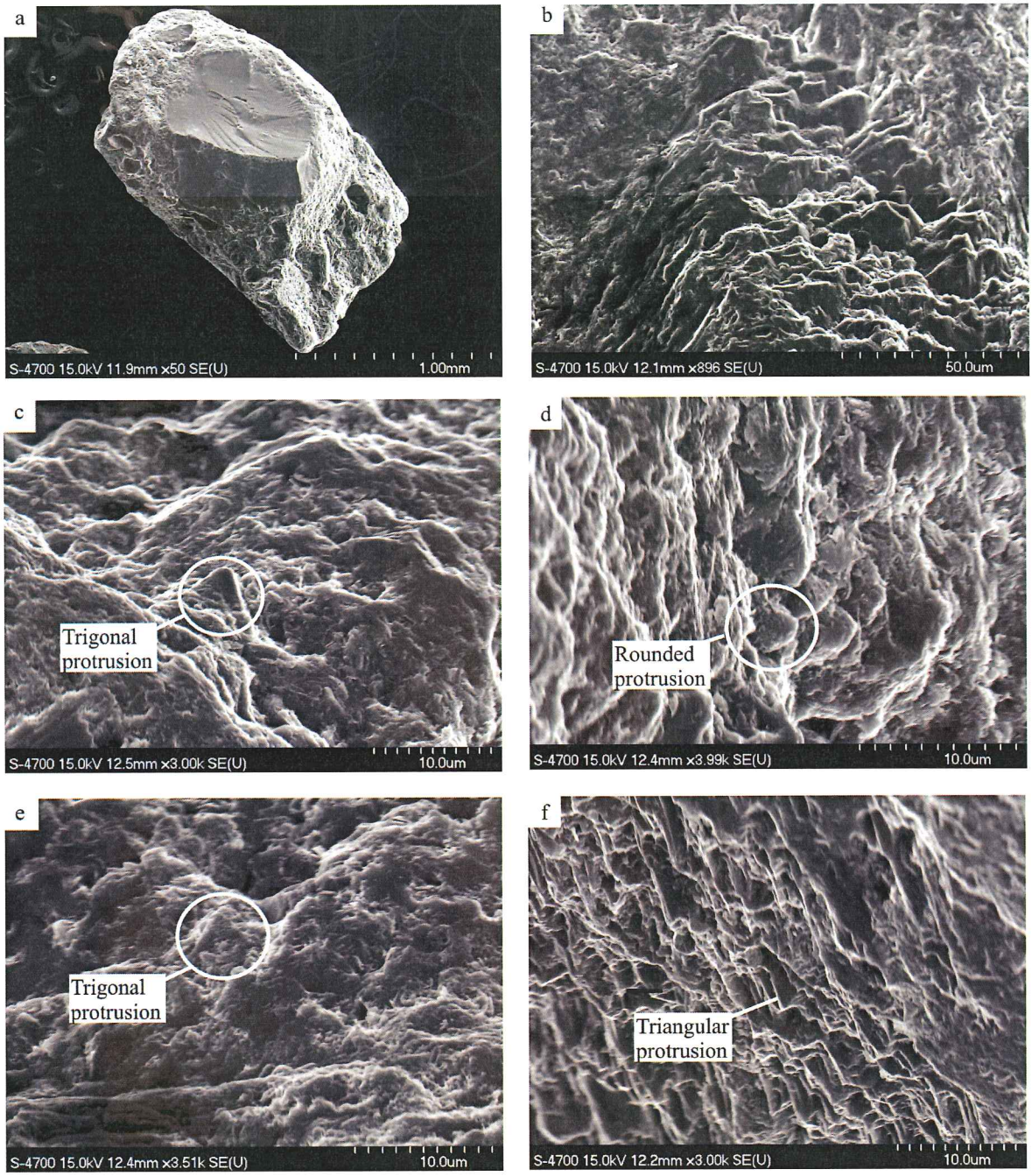

Figure 3.7 SEM images of chromite grain G5, from the Grizzly kimberlite. a) Grain G5 b) Irregular surface features. c,d) More rounded surface features. e) More poorly formed trigons. f) Angular surface features.

3.1.3 Ilmenite Surface features

All natural ilmenite grains examined in this project were from the Misery kimberlite, as the heavy mineral concentrate from the Grizzly kimberlite did not contain this mineral. Compared to chromites extracted from the Misery kimberlite, ilmenites showed a large variation in naturally formed surface features (Fig. 3.8-3.11). The features were highly variable and irregular, and showed no regularly repeating or similar forms. The most abundant surface features were lamellae on ilmenite R1aG4 (Fig. 3.9a,c,e). The most interesting features were the protrusions on the surface of the ilmenite R1aG7 (Fig. 3.10c,d). They resembled the pyramidal shaped surface features shown in Chapter 4 that were described in Afanasiev et al. (2001), although they were much smaller. Ilmenite R1aG9 had a textured and irregular surface (Fig. 3.11).

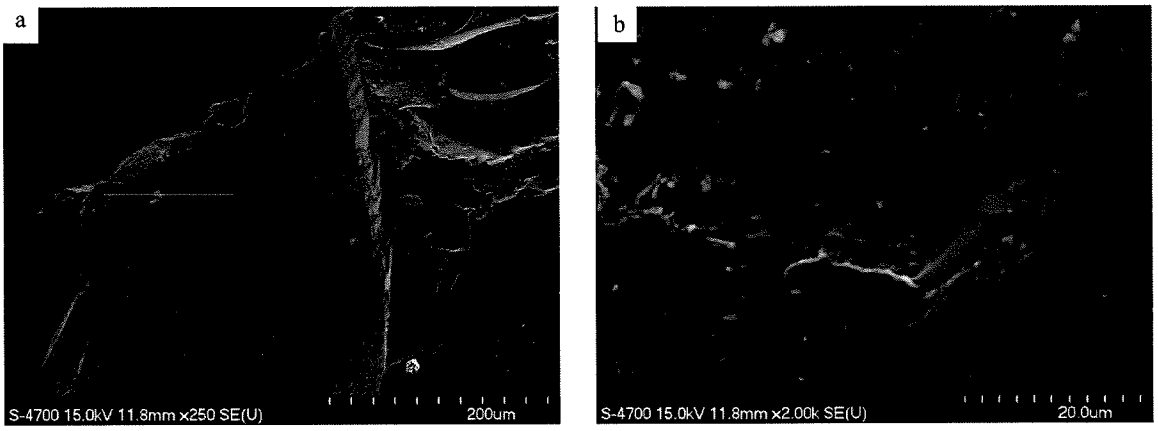

Figure 3.8a-e. SEM images of fractured ilmenite grain R1aG3, from the Misery kimberlite.

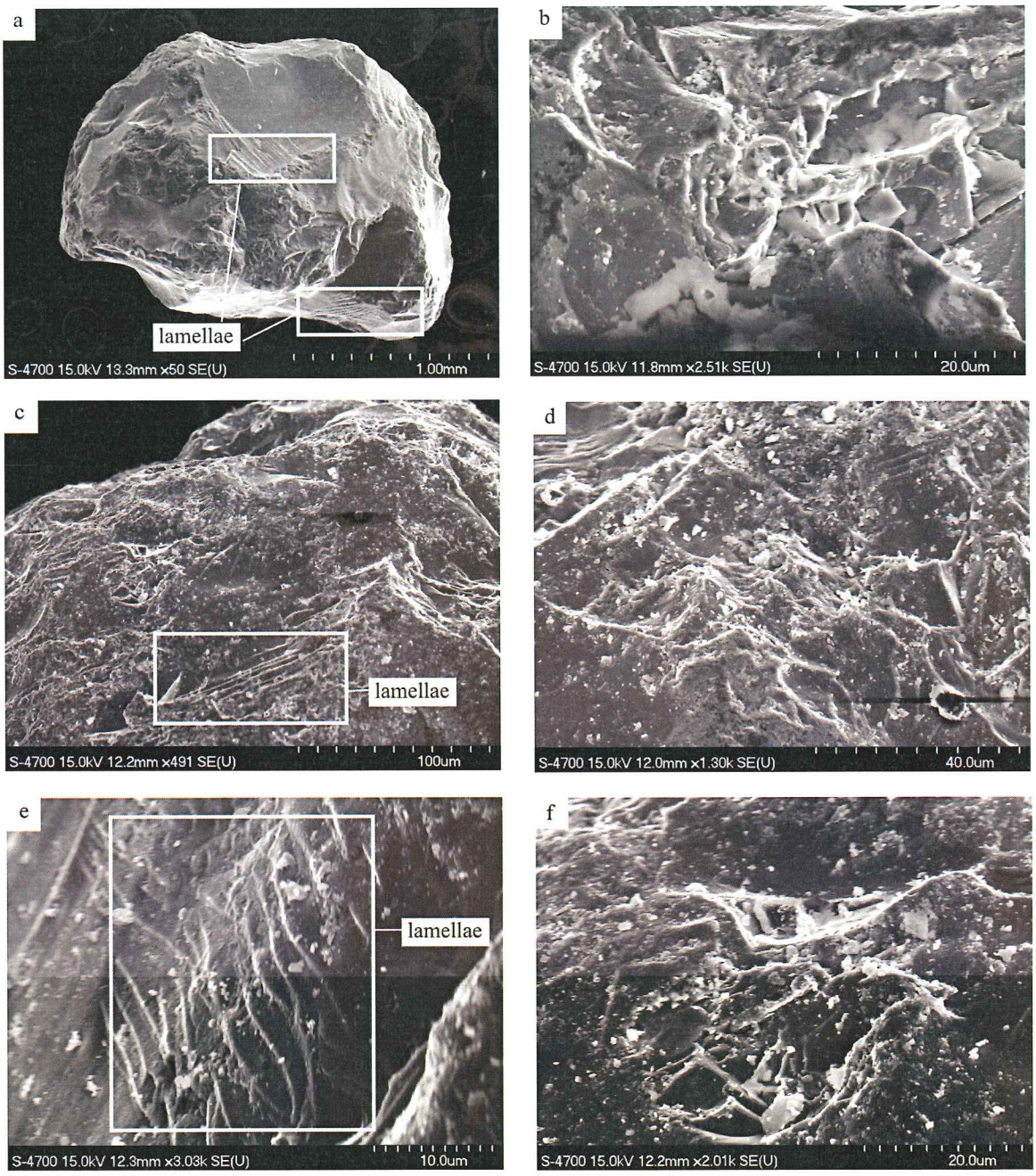

Figure 3.9. SEM images of ilmenite grain R1aG4, from the Misery kimberlite**.** a) Lamellae b) Irregular surface features. c) Irregular surface features and lamellae. d) Irregular surface features. e) More lamellae. f) Irregular surface features.

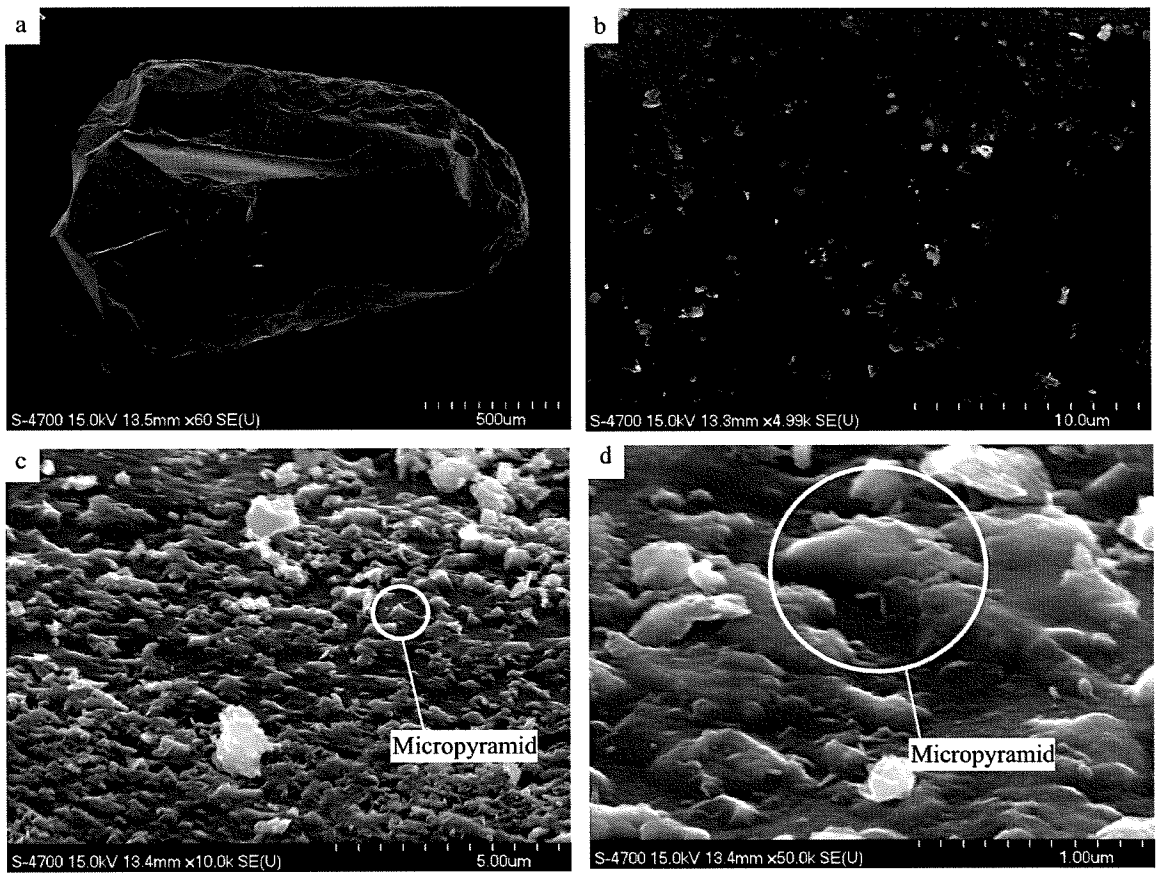

Figure 3.10 SEM images of ilmenite grain R1aG7, from the Misery kimberlite. a) The full grain. b) A smoothed surface. C,d) Micropyramidal surface features.

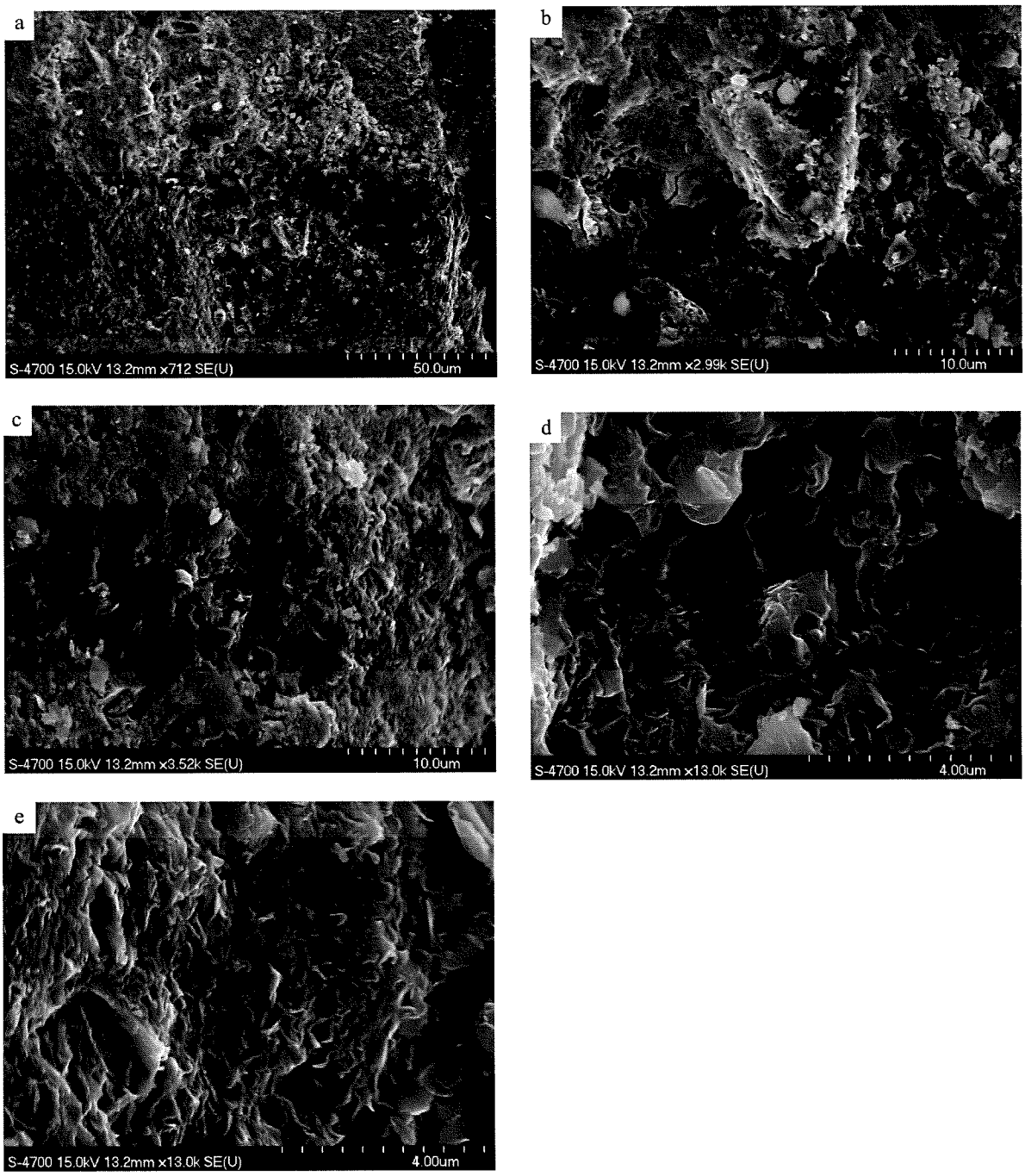

Figure 3.11a-e. SEM images of irregular surface features on ilmenite grain R1aG9, from the Misery kimberlite.

3.2 Experiments with Chromite

3.2.1 CaO-MgO-SiO_2-H_2O System

All experiments were performed using the chemical systems described in Chapter 2. The effect of H_2O on the dissolution of chromite was examined at 0, 5, 13, and 15 wt% H_2O (Fig. 3.12). At 0 wt% the system was anhydrous, and had no water present. At 5 wt% water (bulk composition), the water was dissolved in the melt during the experiment. At 13 and 15 wt% (bulk composition), there was free fluid in equilibrium with the melt. Based on the value of 10 wt% water solubility in diopside melts (Eggler and Burnham 1984), the amount of free H_2O was 3 and 5 wt% (bulk composition) respectively. The phase of the fluid, free vs. dissolved, is also indicated by the appearance of the matrix. Large vesicles which are not associated with quench crystals indicate the presence of a free-fluid phase during the experiment. Small vesicles which form along the boundaries of quench crystals form as a result of natural exsolution of fluids from the melt at lower temperatures and pressures, and do not indicate a free-fluid phase.

The surface features which were created from the interaction of chromite with the fluid were trigonal in shape, and resembled natural surface features from the Misery kimberlite. The general trend observed was that with increasing water content, surface trigons became more angular. The experiment involving a dry diopside analogue produced no surface features (Fig. 3.12a). The experiment involving H_2O undersaturated melt (5 wt% H_2O) produced trigonal, but very rounded surface features (Fig. 3.12b). The experiments conducted at 13 and 15 wt% H_2O both had free H_2O-fluid present in the

system. They produced triangular, protruding surface features which were highly ordered (Fig. 3.12c,d).

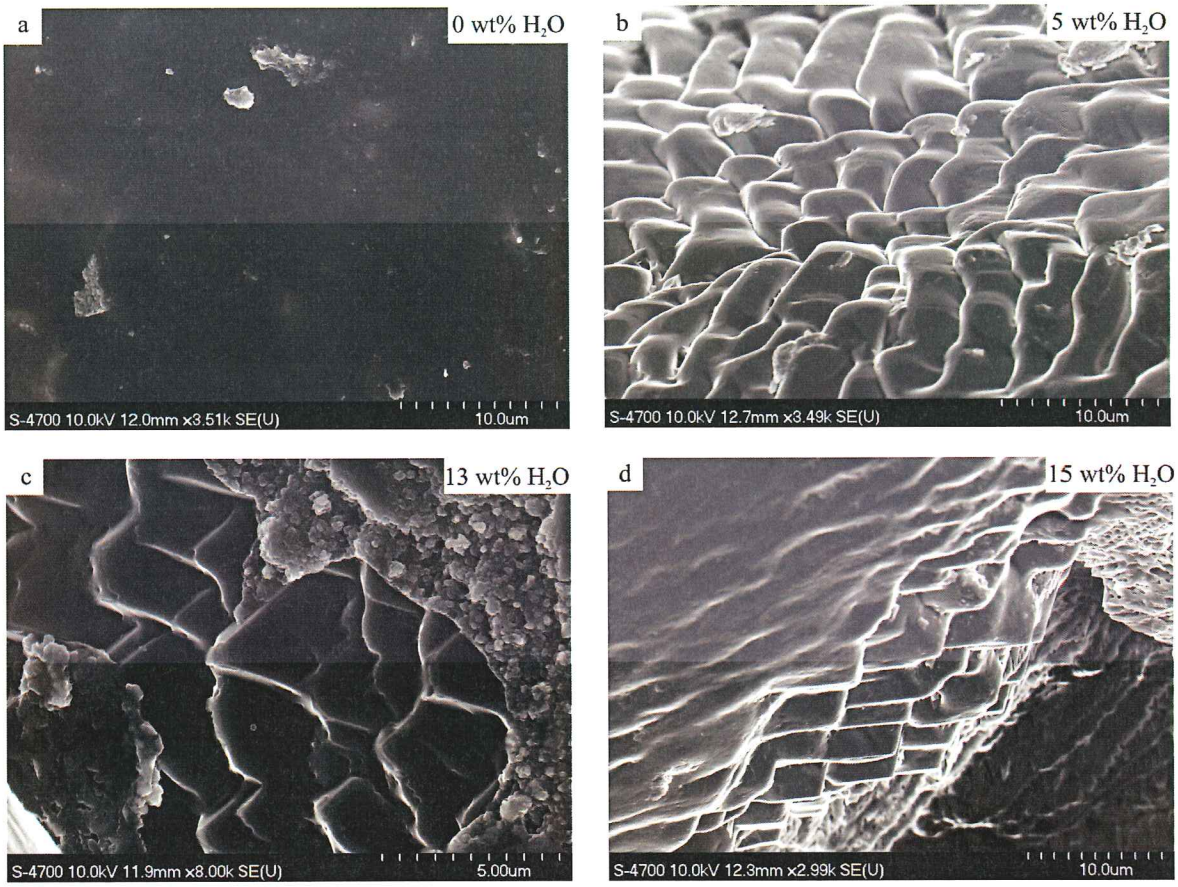

Figure 3.12. Experimentally produced surface features resulting from interaction of chromite and H_2O. a) Images of 0 wt% H_2O run (PC-45), showing a smooth grain free of surface features. b) Images of 5 wt% H_2O run (PC-30), showing rounded trigonal surface features, and wavy step features. c) Images of 13 wt% H_2O run (PC-32), showing protruding triangular surface features with smaller trigonal depressions. d) Images of 15 wt% H_2O run (PC-29), showing protruding triangular surface features.

H_2O- Free Run

In order to be sure that the surface features which resulted from the 5, 13, and 15 wt% H_2O experiments actually arose from interaction with volatiles, the effect of a matrix of anhydrous diopside analogue was determined. This run determined that surface features developed only as a result of interaction with a fluid or volatile component.

Experiment PC-45 examined chromite in a matrix of fluid-free diopside analogue. The matrix is poorly consolidated when the capsule is opened at the end of the run, indicating that it did not melt completely. The chromite fractured easily, so HF was used for grain recovery. A piece of the exterior of the chromite was recovered for imaging with SEM.

Images of the chromite surface features which resulted from this experiment are shown in Figure 3.13. Linear fractures were apparent, but the chromite had an otherwise smooth, recrystallized surface.

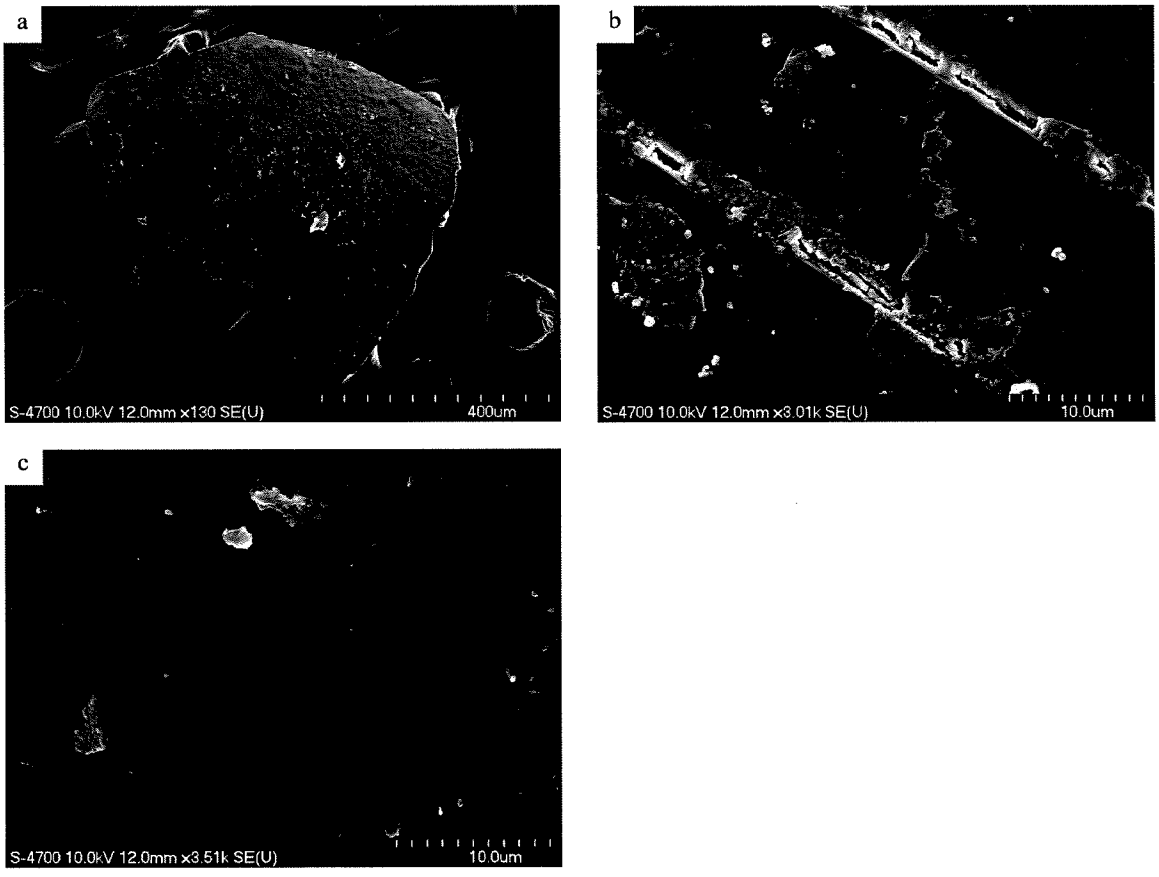

Figure 3.13a-c. SEM images of experimentally produced surface features on chromite in dry diopside analogue (PC-45). The grain surface is smooth and free of surface features.

5 wt% H_2O

The experiment in diopside melt with 5 wt% H_2O had a matrix which consisted of light green quench crystals, with some dark green glass, indicating the material was molten during the run (Fig.3.14). The quench comprised elongate areas of alternating dark and light crystals. These could be clearly distinguished from the glass, as the glass had a very homogeneous appearance (Fig. 3.14 c-e). This matrix does not show vesicles, indicating that there was not a free fluid phase during the experiment. The Pt capsule is shown in many of these images.

Most of the chromite surface was smooth and recrystallized, with surface features developed only along the top edge of the chromite (Fig. 3.15a). The surface features were step-like, and showed a gradational change into rounded surface features (Fig. 3.15b-e). The rounded surface features were the most common feature on the chromite; images of the finer details are shown in Figures 3.15c,e. These features resembled the features of natural chromites, except that these were more rounded.

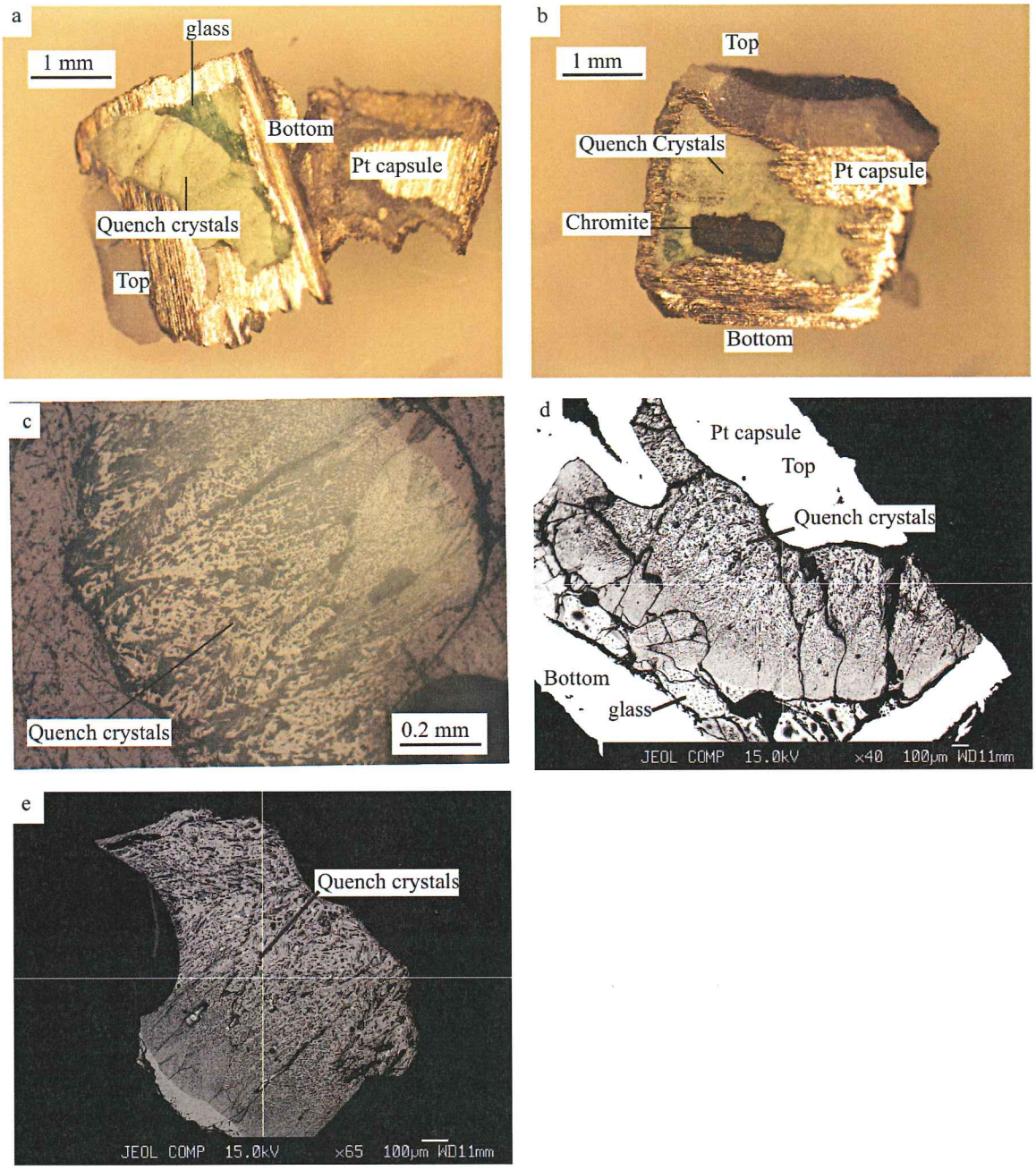

Figure 3.14. Capsule with the sample cut in half after the run in diopside melt with 5 wt% H_2O (PC-30) a) Light green diopside quench crystals and dark-green glass b) Light green diopside quench crystals, dark green glass, and the chromite grain. c) Reflected-light image of a polished section of the matrix, showing diopside quench crystals d,e) Back-scattered images of a polished section of the matrix, showing diopside quench crystals and glass.

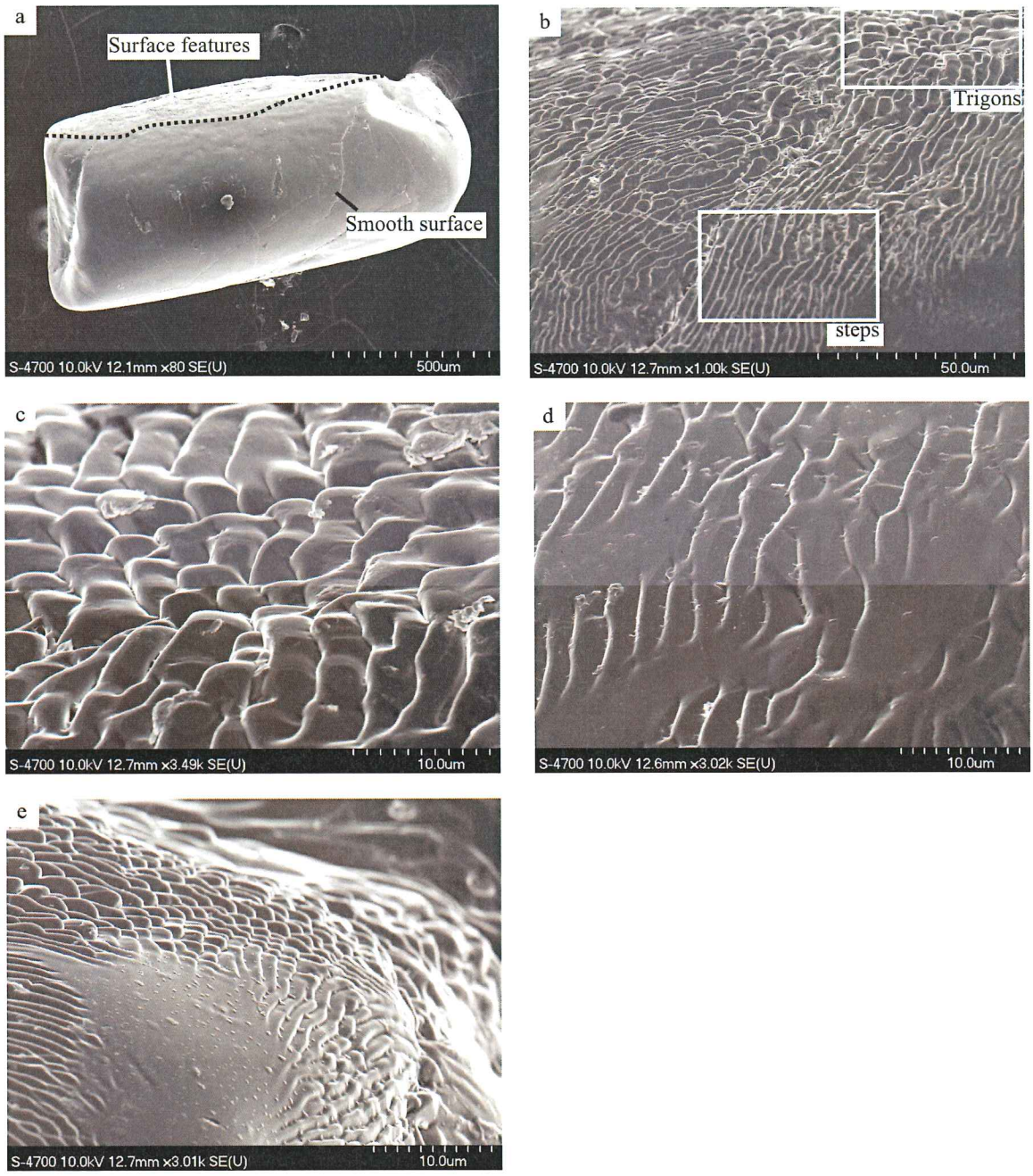

Figure 3.15. SEM images of experimentally-produced dissolution surface features on chromite, from the run in diopside melt with 5 wt% H_2O (PC-30). a) Rare surface features along the top edge. b) Wavy step-like features, and rounded, trigonal surface features. c) Rounded, trigonal surface features. d) Wavy step-like features. e) More rounded dissolution-features.

13 wt% H_2O

Experiment PC-32 examined the effect of 13 wt% H_2O on the surface of chromite. After the experiment, the capsule appeared to have expanded. This indicated that there was no fluid loss during the run. If there was no outward pressure from fluid exsolution upon cooling, then the capsule would have a collapsed appearance. Also, when the capsule was punctured, a smell escapes which has previously been associated with a free fluid phase during the run (Fedortchouk 2009. P. Comm).

After the run, the matrix was green (Fig.3.16 a-d). Light green quench crystals surrounded the chromite grain, and dark green glass surrounded the quench crystals (Fig. 3.16a,b). In the figures, the phase boundary is marked by a red line. The polished section of the matrix examined in reflected light showed many vesicles that were not associated with the quench crystals (Fig. 3.16c-f). This indicated that there was a free fluid phase during the run.

Surface features that resulted from chromite dissolution in 13 wt% H_2O are shown in Figure 3.17. The majority of the chromite was covered in surface features (Fig. 3.17a). The chromite had a large amount of matrix attached to its surface that was avoided during imaging. A closer view of the textured surfaces showed the emergence of more protruding triangular surface features. These features were abundant and had a common orientation (Fig. 3.17c-f). There were also linear step features which were analogous to the wavy steps in the experimental chromite from 5 wt% H_2O (Fig. 3.17c,d). The high proportion of fluid here allowed for the development of more surface features, so trigons and steps became more regular. Protruding triangular surface features were common on

the surface of this grain, and the trigonal depressions observed on the natural chromites developed during this experiment (Fig 3.17e,f).

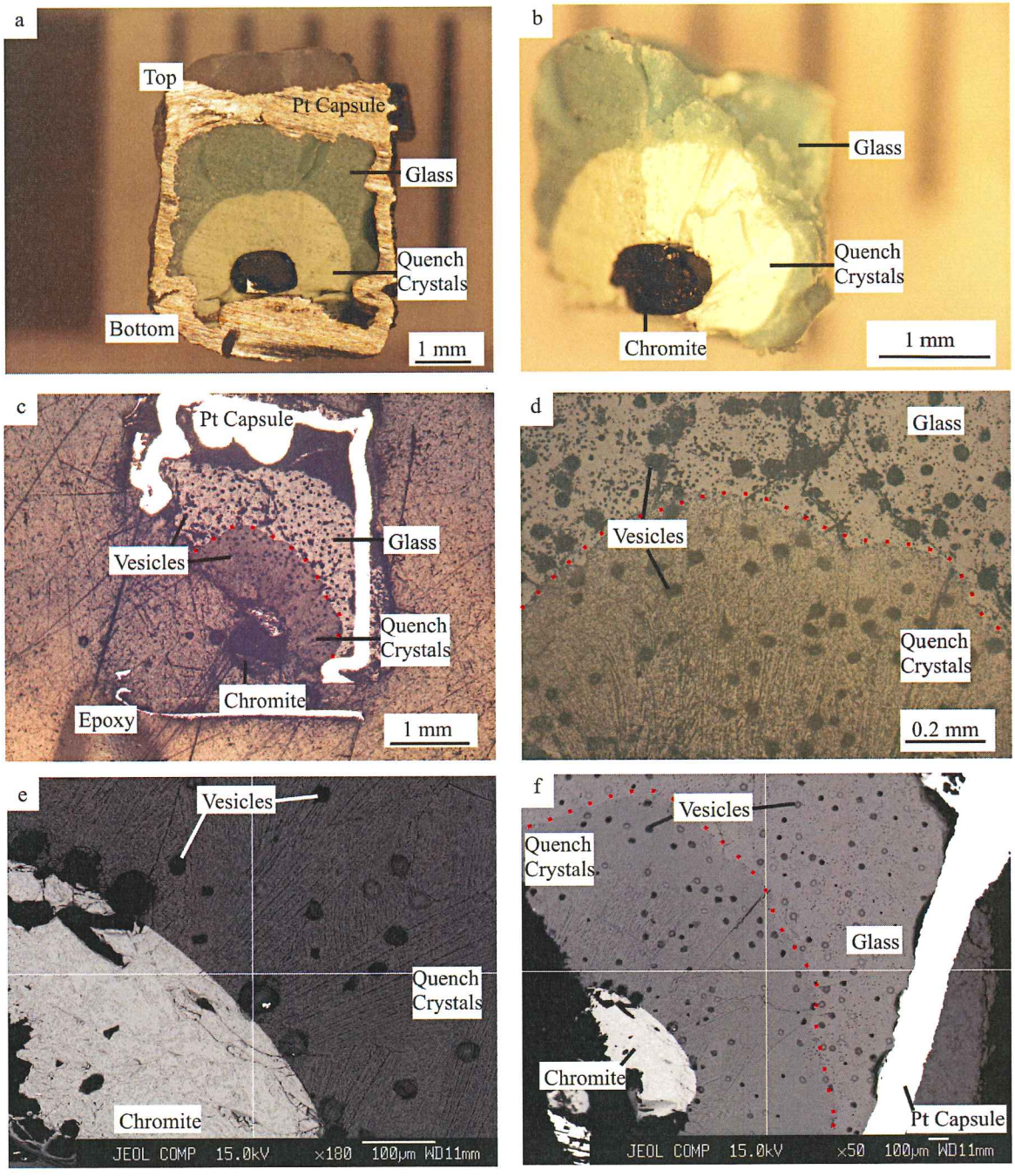

Figure 3.16 Images of experimental results of run PC-32, which studied chromite dissolution in diopside melt with 13 wt% H_2O. a,b) Light green diopside quench crystals, dark green glass, and the chromite grain. c) A polished section of the capsule in reflected light. d) A polished section showing vesicles in the matrix. e) Back-scattered image of the chromite grain, diopside quench crystals, and vesicles. f) Back-scattered image, showing vesicles in the matrix.

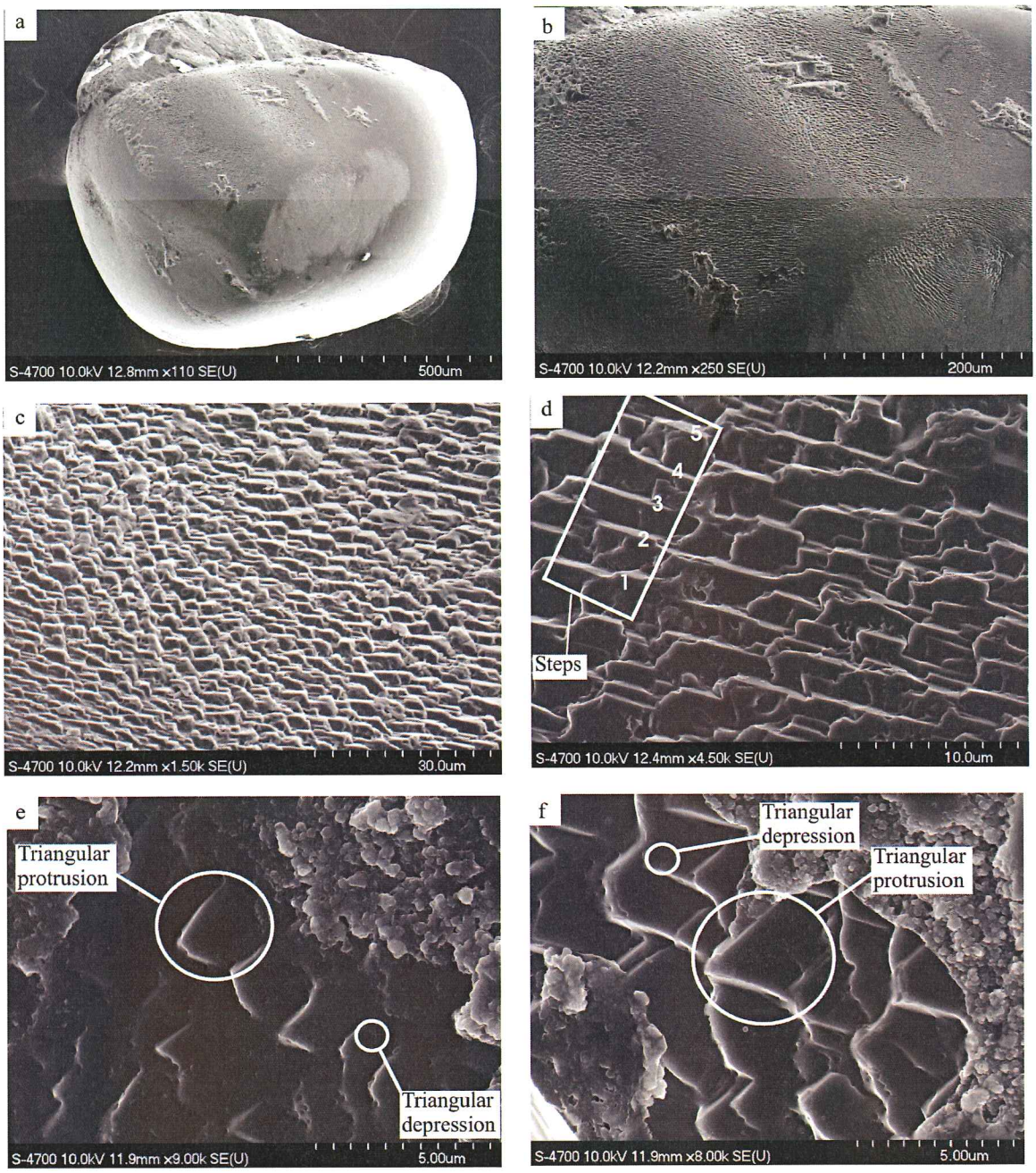

Figure 3.17 SEM images of experimentally surface features on chromite in diopside melt with 13 wt% H_2O (PC-32). a) Full view of the experimental grain. b) The highly textured chromite surface. c) Protruding, well-ordered, triangular surface features. d) Angular step-like features e) Protruding,, triangular surface features. f) Triangular surface features, with trigonal depressions.

15 wt% H_2O

Experiment PC-29 examined the effect of 15 wt% H_2O on the surface of chromite. The matrix in this run was entirely light green and opaque, with no glass (Fig. 3.18a,b). Back-scattered (Fig. 3.18e,f) and reflected light (Fig. 3.18c,d) images of a polished section of matrix show quench crystals. The presence of quench crystals indicated the matrix was molten during the run.

The experimental chromite had a flat surface that resulted from cutting open the capsule, and a fracture surface, which was also formed during the capsule opening process (Fig. 3.19a). The rest of the grain developed rounded (Fig. 3.19b) and triangular dissolution-features during the experiment (Fig. 3.19c). The angular surface features had a consistent orientation, and the rounded features were more randomly oriented. Surface features were sparse on this chromite. Most of the surface was shiny and recrystallized (Fig. 3.19a). Wavy step-like features (Fig. 3.19d), and trigonal and circular depressions (Fig. 3.19e,f) were also apparent on this chromite.

The regular step-like features were similar to those developed during chromite dissolution in diopside melt with 13 wt% H_2O, and likely developed from chromite interaction with free H_2O fluid. The round and smooth features possibly resulted from a partial fluid loss in this run.

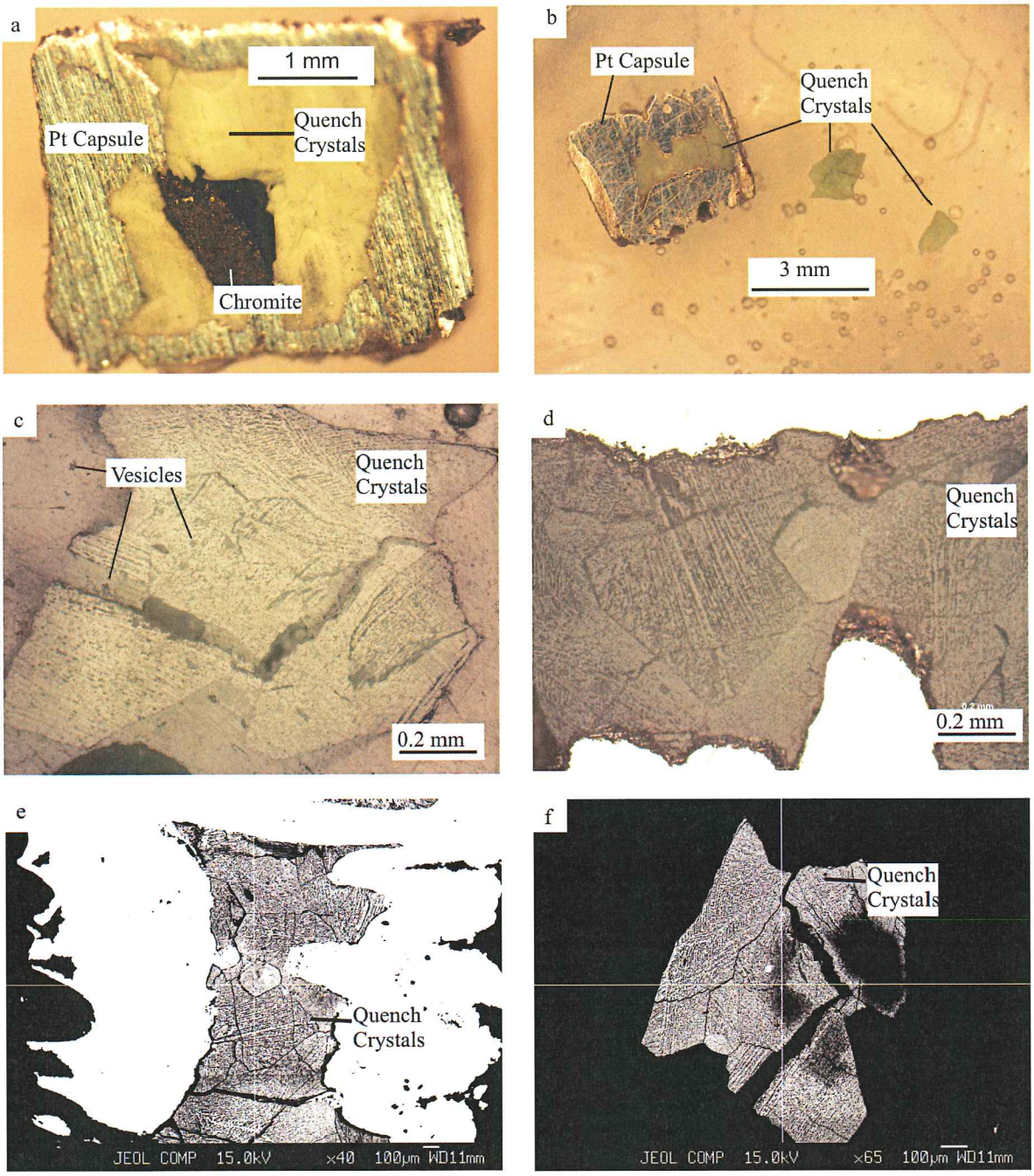

Figure 3.18 Images of experimental results of run PC-29, studying chromite in diopside analogue with 15 wt% H_2O. a) Chromite grain in light green diopside quench crystals. b) Light green diopside quench crystals. c,d) Polished section of diopside quench crystals in reflected light. e,f) Back-scattered images of diopside quench crystals.

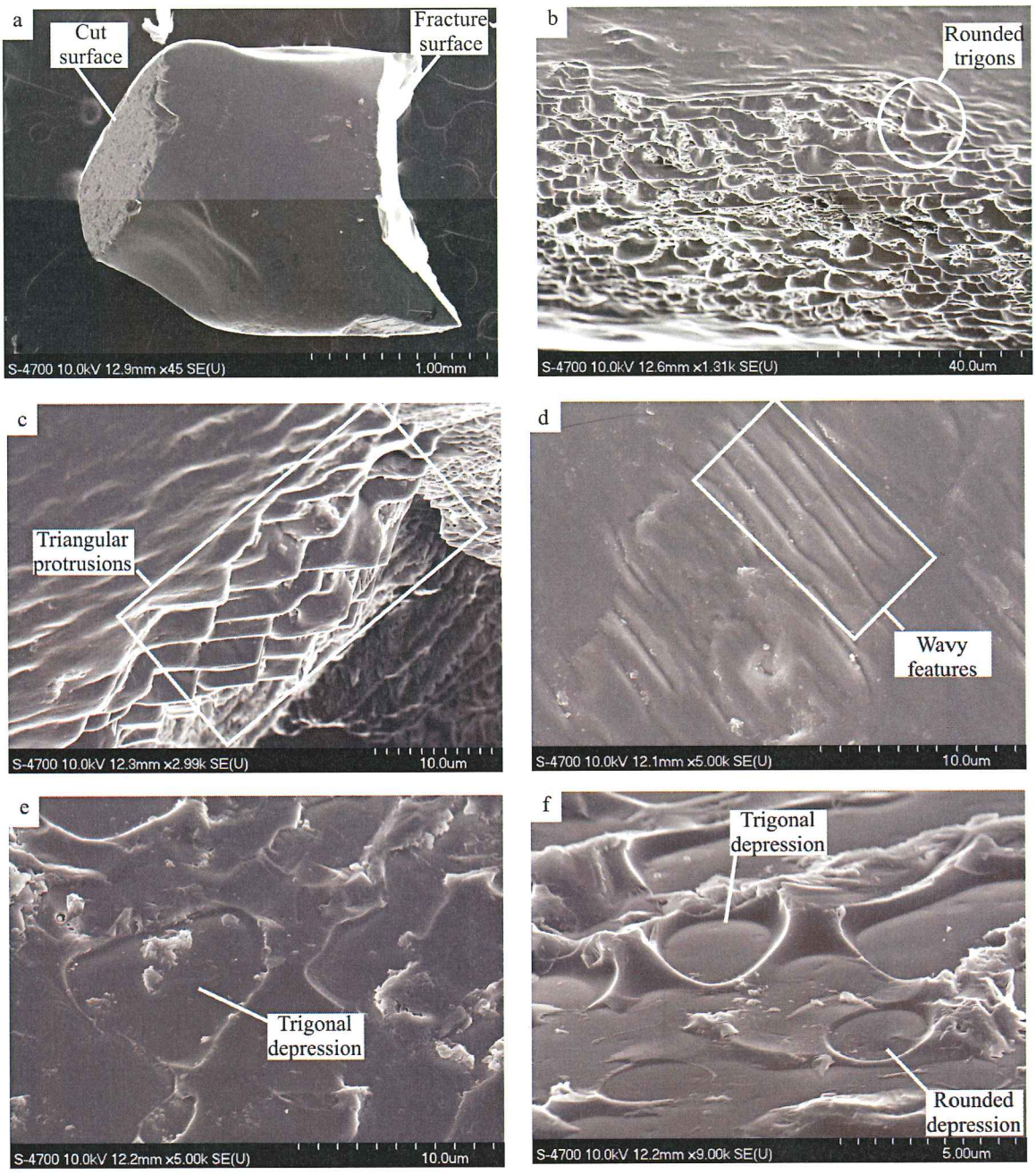

Figure 3.19 SEM images of experimental surface features from the study of chromite in a matrix of diopside analogue, plus 15 wt% H_2O (PC-29). a) The full grain. b) Rounded trigonal surface features, with variable orientation. c) Well-ordered, protruding, triangular surface features. d) Wavy step-like structures. e) Trigonal depressions f) Trigonal and circular depressions.

3.2.2 CaO-MgO-SiO_2-CO_2 System

Two experiments examined the effect of CO_2 fluid on chromite dissolution. Experiment PC-35 was run with 5 wt% CO_2 in a matrix of diopside analogue, and experiment PC-37 was run with 27 wt% CO_2 in a matrix of wollastonite analogue. The surface features that resulted from CO_2 interaction with chromite were significantly different from those which developed from interaction with H_2O fluid. The surface features which resulted from 5 wt% CO_2 are shown in Figure 3.20a-c, and Figure 3.21. After the run, the grain surface was mostly smooth with some small nodular features. The surface features that resulted from interaction with 27 wt% CO_2 are shown in Figure 3.20d-f, and Figure 3.23. The conditions of this experiment lead to a highly textured surface, which included angular depressions and protruding polyhedral features.

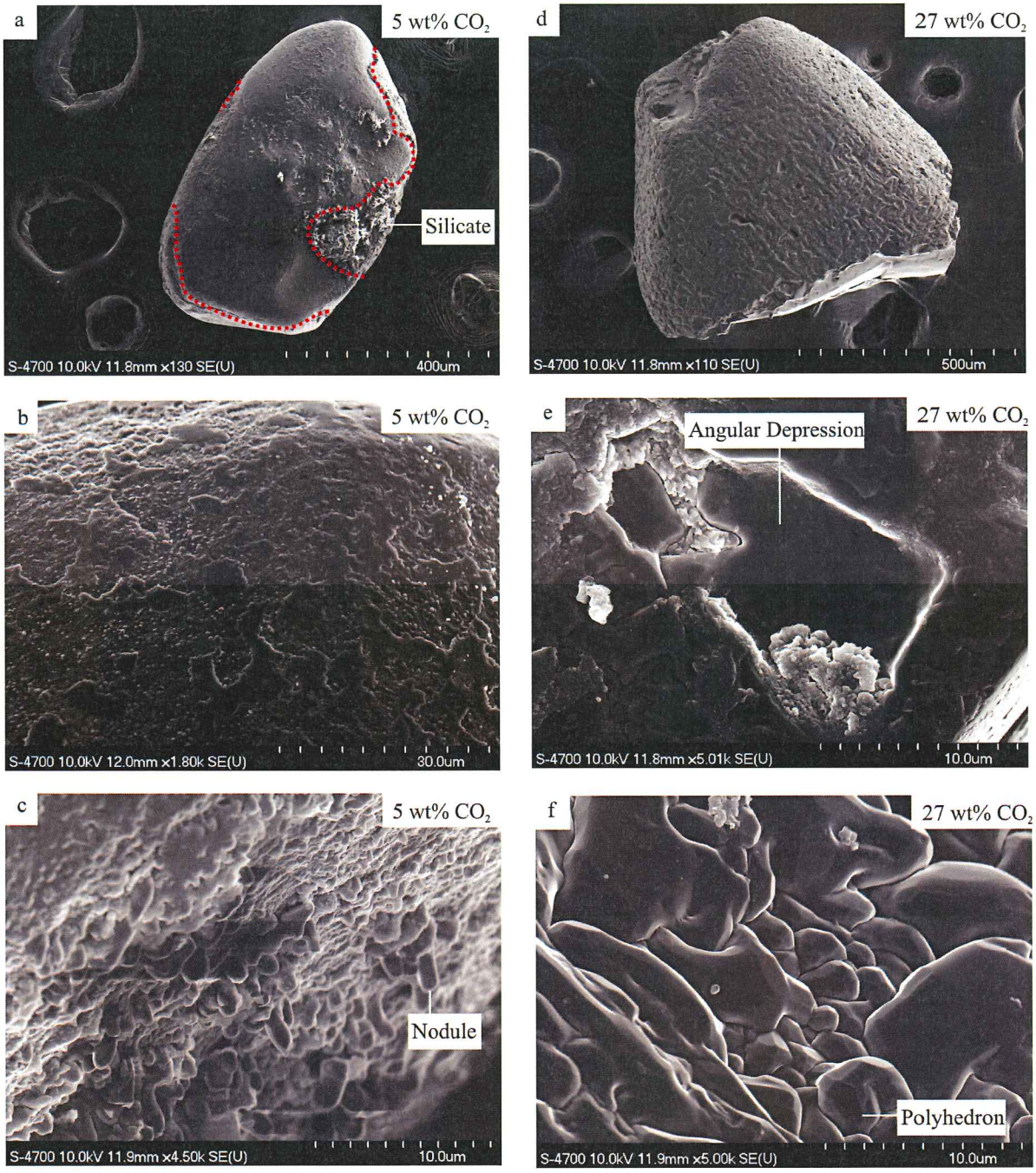

Figure 3.20 Experimentally produced surface features on chromite from interaction with 5 wt% CO_2 (a-c) and 27 wt% CO_2 (d-f). a) Grain view b) Smooth surface c) Rounded nodular surface features. d) Grain with highly textured surface. e) Angular depressions. f) Protruding polyhedrons.

5 wt% CO_2

Experiment PC-35 examined the effect of 5 wt% CO_2 on the surface of chromite. The matrix was green, similar to the experiments that examined the interaction of chromite and water. There were light green quench crystals at the top and bottom of the cut section, and vesicular dark-green glass in the centre (Fig. 3.21a). The chromite was surrounded by quench crystals. A polished section showed clearly the boundary between the glass and quench crystal phase, marked with a red dashed line (Fig. 3.21b-d). The matrix was vesicular, which indicated a free fluid phase during the run (Fig.3.21f).

The surface features on the chromites with CO_2 fluid were significantly different from those that developed in H_2O fluid. The experiment with 5 wt% CO_2 fluid made the chromite surface mostly smooth (Fig. 3.22a,b), with some nodular features at higher magnifications (Fig. 3.22c,d). These nodular features were small, rounded, and did not show any angularity (Fig. 3.22e,f). In addition to the nodules, very fine linear features also were formed across the entire chromite grain (Fig3.22c,d).

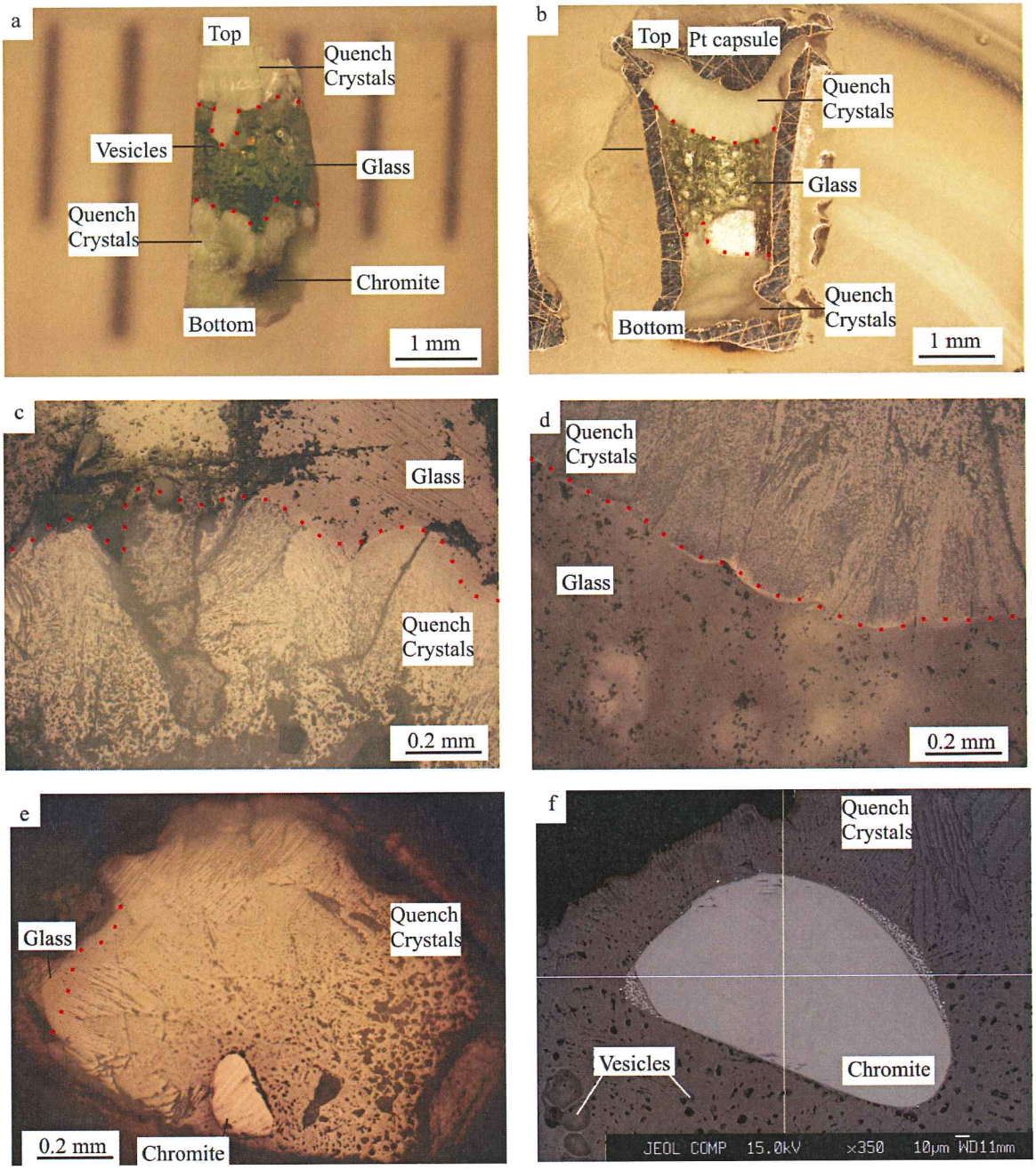

Figure 3.21 Images of experiment PC-35, studying chromite dissolution in diopside melt with 5 wt% CO_2. a) Experimental matrix.b) Polished section of experimental matrix. c,d) A polished section in reflected light, showing glass and diopside quench crystals. e) A polished section in reflected light, showing the chromite grain in diopside quench crystals. f) A back-scattered image of the chromite grain in diopside quench crystals.

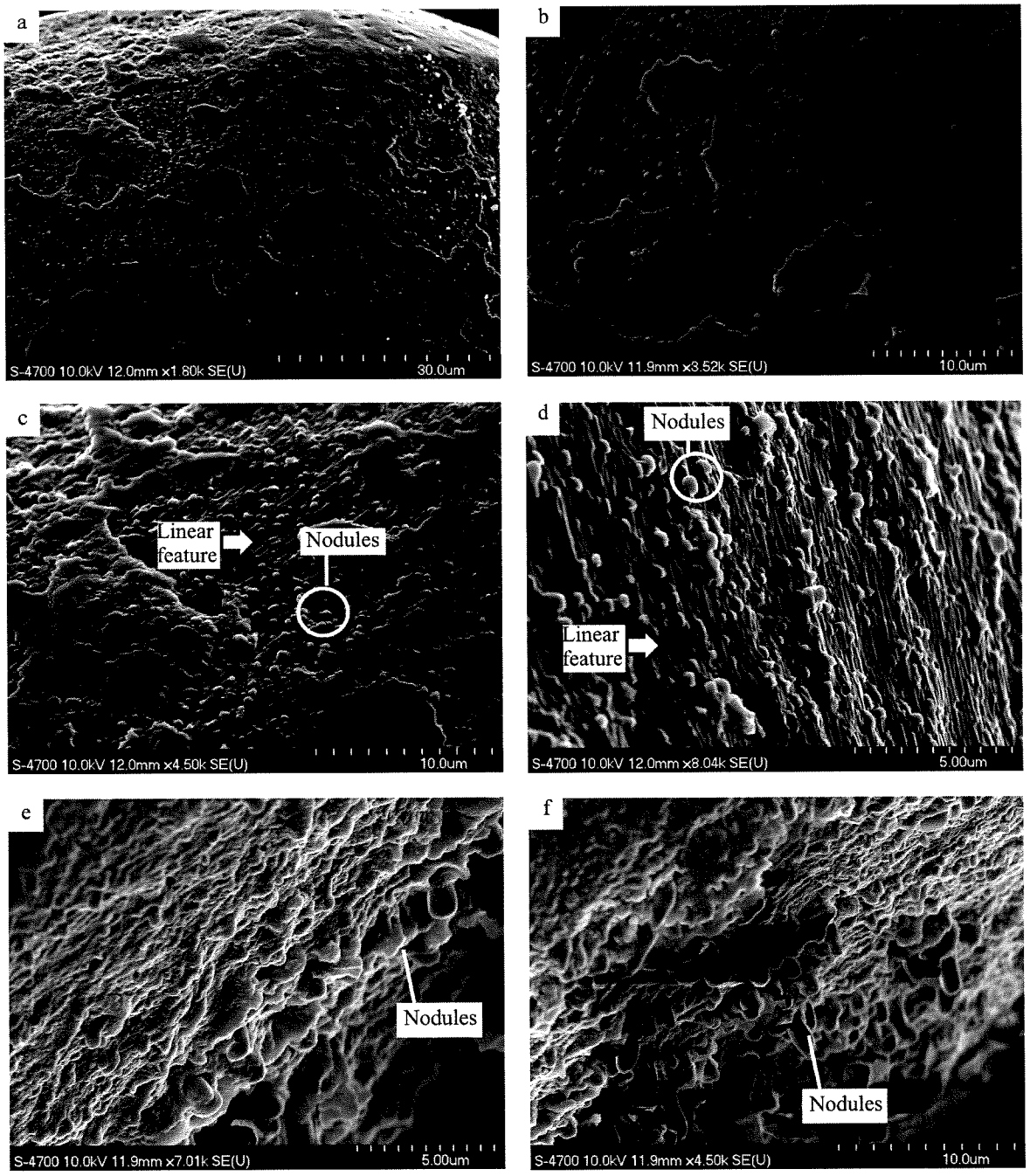

Figure 3.22 SEM images of experimentally produced surface features on chromite in diopside melt with 5 wt% CO_2 (PC-35) a,b) The smooth surface, showing few surface features. c) A closer view of the surface, showing rounded nodular features d) Nodular surface features and linear step-like features. e,f) More rounded, nodular features.

27 wt% CO_2

Experiment PC-37 was performed on a chromite in a matrix of wollastonite analogue with 27 wt% CO_2. When the cell was opened, there was a loud hissing sound, likely caused by the escape of free gas, indicating that a free fluid phase was present during the experiment. Also, there was a large void space at the top of the capsule, between the platinum and the matrix, which could only exist if gas occupied that space during the experiment. The matrix had an interesting profile. There was a gradational change in colour from bottom to top, changing from white to brown to green (Fig. 3.23a,b). The white and brown areas comprised opaque quench crystals, and the green area consisted of a transparent vitreous glass. Figures 3.23c-d show reflected light images of the vesicular quench crystals, and the crystal/glass phase boundary. Back-scattered images of the cell profile show quench crystals, glass, and chromite (Fig. 3.23e,f). The chromite was extensively altered by the free fluid, and showed a thick resorption ring, up to10 μm thick (Fig. 3.23f).

The experimental chromite grain showed a highly textured surface with three types of surface features. First, rounded, protruding surface features were present at low magnification (Fig. 3.24a). The second set of surface features were smaller, but ubiquitous on the grain, and grew on the surface of the first type (Fig. 3.24a,b), as well as on other areas of the grain (Fig. 3.24c-e). These features appeared rounded at low magnification, but when viewed under high magnification, these features were well-formed, orderly polyhedrons (Fig. 3.24f). The third type of surface feature expressed on the surface of this experimental grain was a series of angular depressions which also covered most of the grain. These depressions were well formed, and were interspersed with the aforementioned polyhedral surface features (Fig. 3.24c,d).

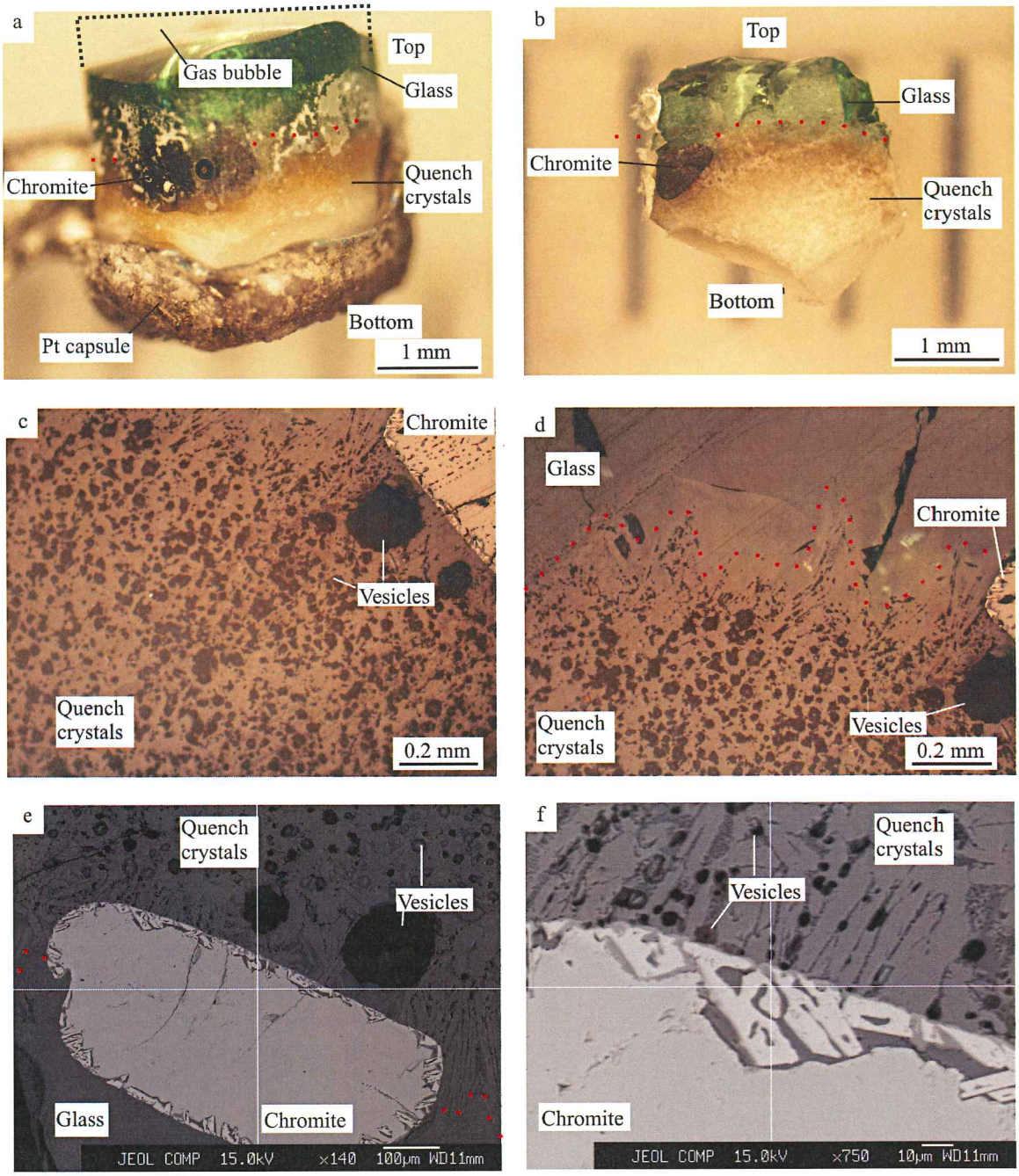

Figure 3.23 Images of experimental results of run PC-35, which studied chromite dissolution in wollastonite analogue melt with 27 wt% CO_2. a,b) Capsule profile, showing quench crystals, glass, and the chromite grain. c) Polished section in reflected light showing quench crystals with vesicles, and the chromite grain. d) Polished section in reflected light showing glass/quench crystal boundary, vesicles, and the chromite grain. e,f) Back-scattered image of the chromite grain, quench crystals, and vesicles.

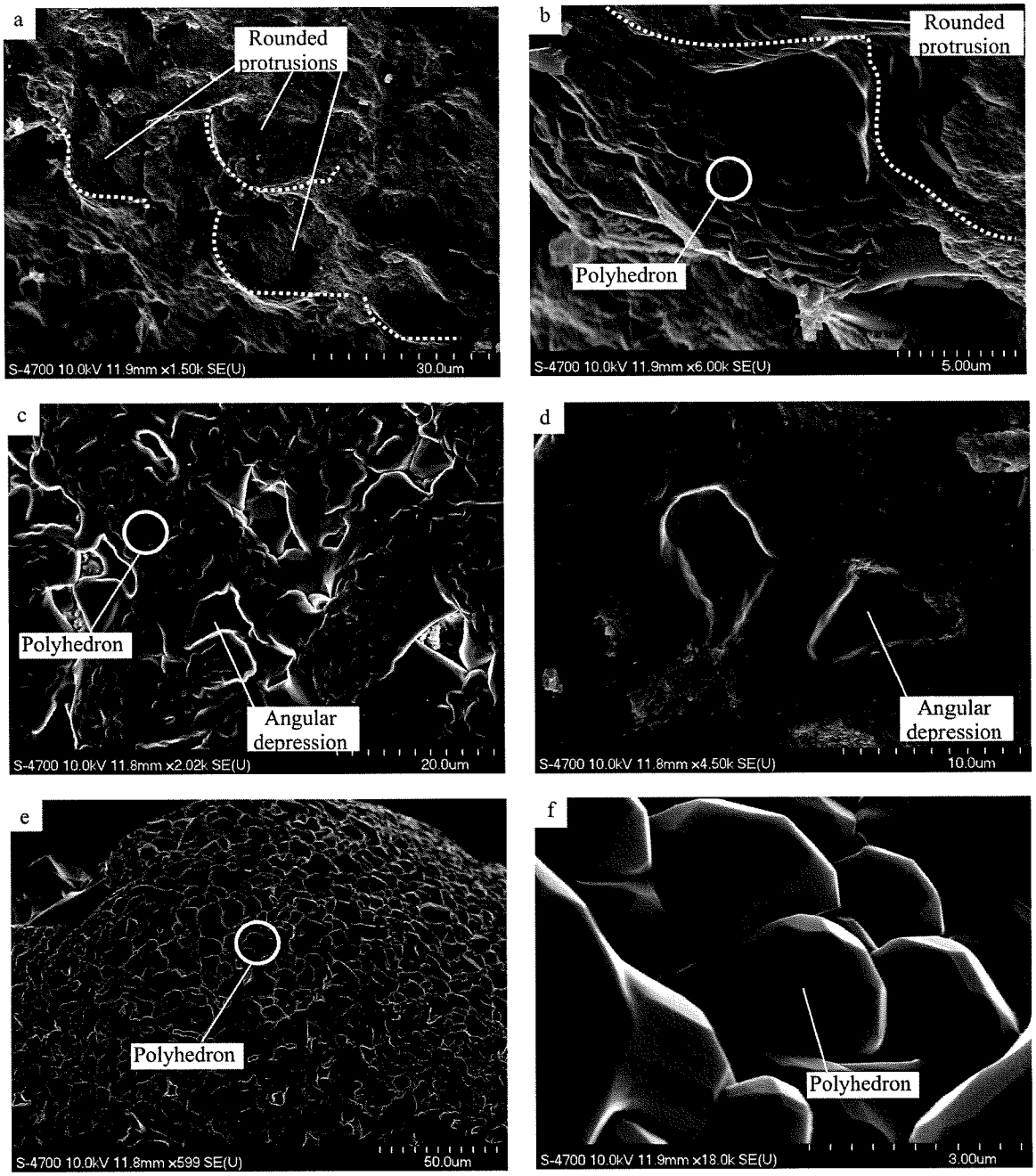

Figure 3.24 SEM images of experimentally produced surface features on chromite in wollastonite analogue with 27 wt% CO_2 (PC-37). a) Large, round surface features. b) Large, round surface features which display smaller polyhedrons. c) Angular depressions, with small polyhedrons. d) Angular depressions e) Polyhedrons. f) Detailed view of polyhedrons.

3.3 Experiments with Ilmenite

3.3.1 Overview

Three experiments investigated the effect of H_2O and CO_2 fluid on ilmenite grains. Experiments PC-39, 42, and 38 were conducted with a diopside analogue plus 5 wt% H_2O, magnesium oxide plus 31 wt% H_2O, and wollastonite analogue plus 27 wt% CO_2, respectively. At the experimental conditions of this study ilmenite had a higher rate of dissolution than chromite. The experimental ilmenite dissolved in all experiments except PC-42, which studied the resorption features caused by MgO with 31 wt% H_2O.

3.3.2 H_2O-Fluid Results

5 wt% H_2O

Experiment PC-39 investigated the effect of 5 wt% H_2O in a matrix diopside analogue on the surface of ilmenite. However, the ilmenite dissolved in the matrix at these experimental conditions. The matrix was almost entirely dark olive-green glass. At the top of the capsule, there were sparse pale-green crystals. A picture of the capsule shows the colouration of the run product (Fig. 3.25a). A back scattered image (Fig. 3.25b) and reflected light images (Fig. 3.25c,d) show the boundaries between the glass and crystalline phases of the matrix.

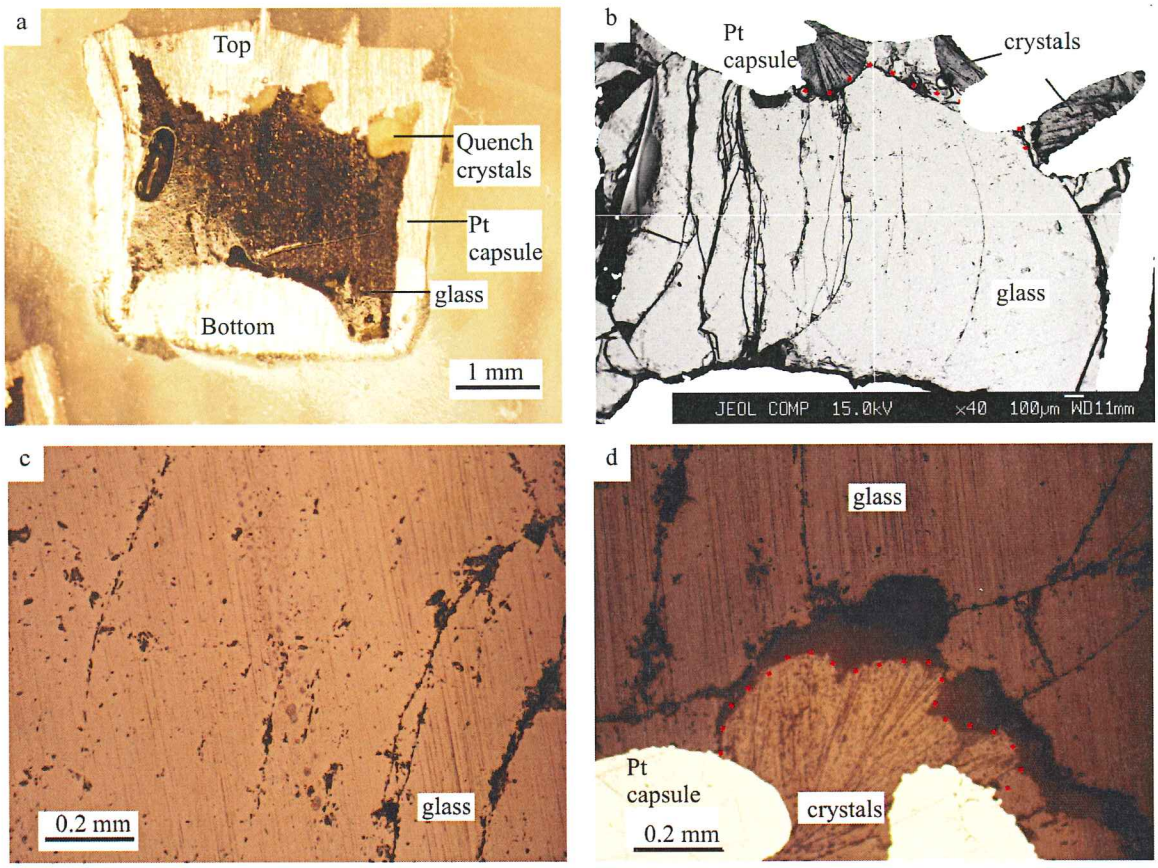

Figure 3.25 Images of experimental results of PC-39, studying ilmenite dissolution in diopside analogue with 5 wt% H_2O. a) Capsule profile, showing light green quench crystals, and olive-green glass. b) Back-scattered image of capsule showing glass and quench crystals. c) Polished section of glassy matrix in reflected light. d) Polished section of glassy matrix and quench crystals in reflected light.

31 wt% H_2O

Experiment PC-42 examined the effect of 31 wt% H_2O in magnesium oxide on the surface-dissolution of ilmenite. The ilmenite was preserved during the run, allowing for the analysis of its surface features. The matrix in this experiment was not like that of the other systems studied in this project. There were euhedral white and black magnesium oxide crystals surrounding the ilmenite grain (Fig. 3.26a), indicating solid-state recrystallization of MgO. The grain itself was brecciated around its edge, and the boundary between the two phases was difficult to define using reflected light images of the polished profile. The matrix here was not as cohesive as in the other experiments. Therefore, many grains of the MgO matrix were lost during the polishing process, and an even surface was never totally achieved. This resulted in poor quality microprobe data.

The grain was almost entirely covered with euhedral crystals of MgO, leaving only a small space available for the analysis surface features (Fig. 3.27a,b). Hydrofluoric acid does not dissolve oxides, so this chemical could not be used for the removal of the matrix as in the other experiments. The surface features were generally angular and irregular (Fig. 3.26c). When the surfaces were examined in greater detail, there were small protrusions, called "micropyramids" that resembled features on natural ilmenite grains from the Misery kimberlite.

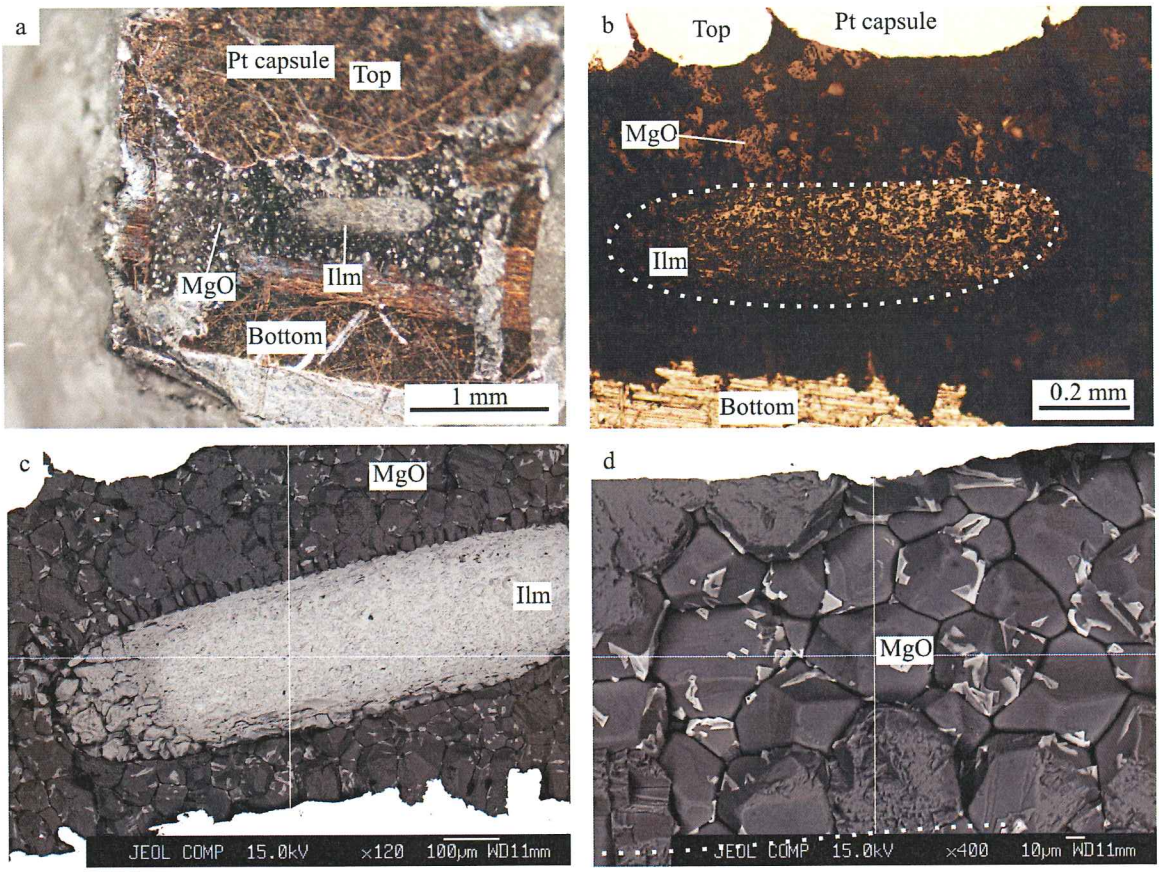

Figure 3.26 Images of experimental results of PC-42, studying ilmenite dissolution in diopside analogue with 31 wt% H_2O. a) Chromite grain and MgO matrix. b) Polished section in reflected light, showing the ilmenite grain and MgO matrix. c) Back-scattered image of the ilmenite in euhedral MgO crystals d) Back-scattered image showing MgO crystals.

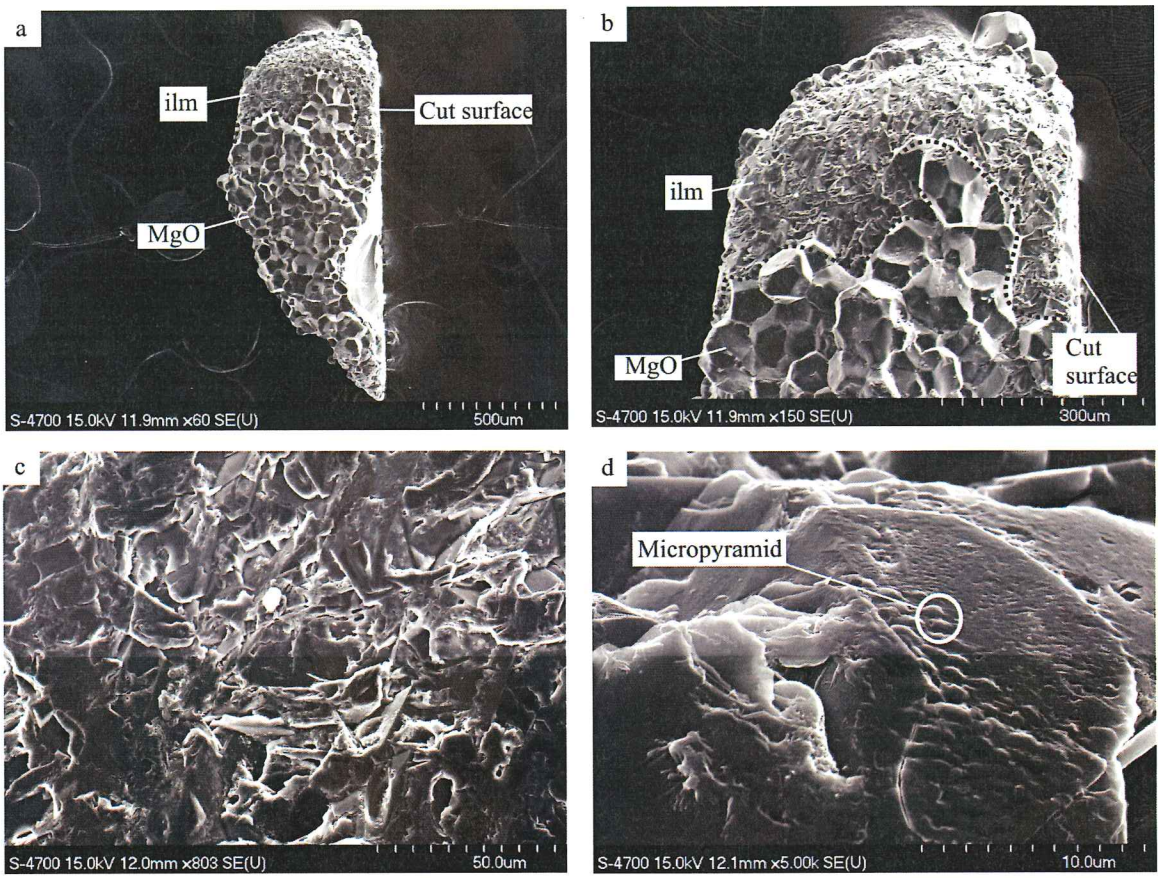

Figure 3.27 Images SEM images of experimentally produced surface features on ilmenite in MgO with 31 wt% H_2O (PC-42). a,b) The experimental grain covered in MgO crystals, with a small area of ilmenite exposed at the top of the images. c) Irregular surface features. d) Micropyrimadal surface features.

3.3.3 CO_2 Fluid Results

27 wt% CO_2

Experiment PC-38 was performed on an ilmenite grain, and studied the effect of a wollastonite analogue with 27 wt% CO_2 on the surface dissolution of chromite. The matrix was black and contained a very large void created during the run by the fluid (Fig 3.27). The grain was not stable at these experimental conditions, and was totally dissolved in the matrix. Images of the capsule and the grain can be found in Figure 3.28.

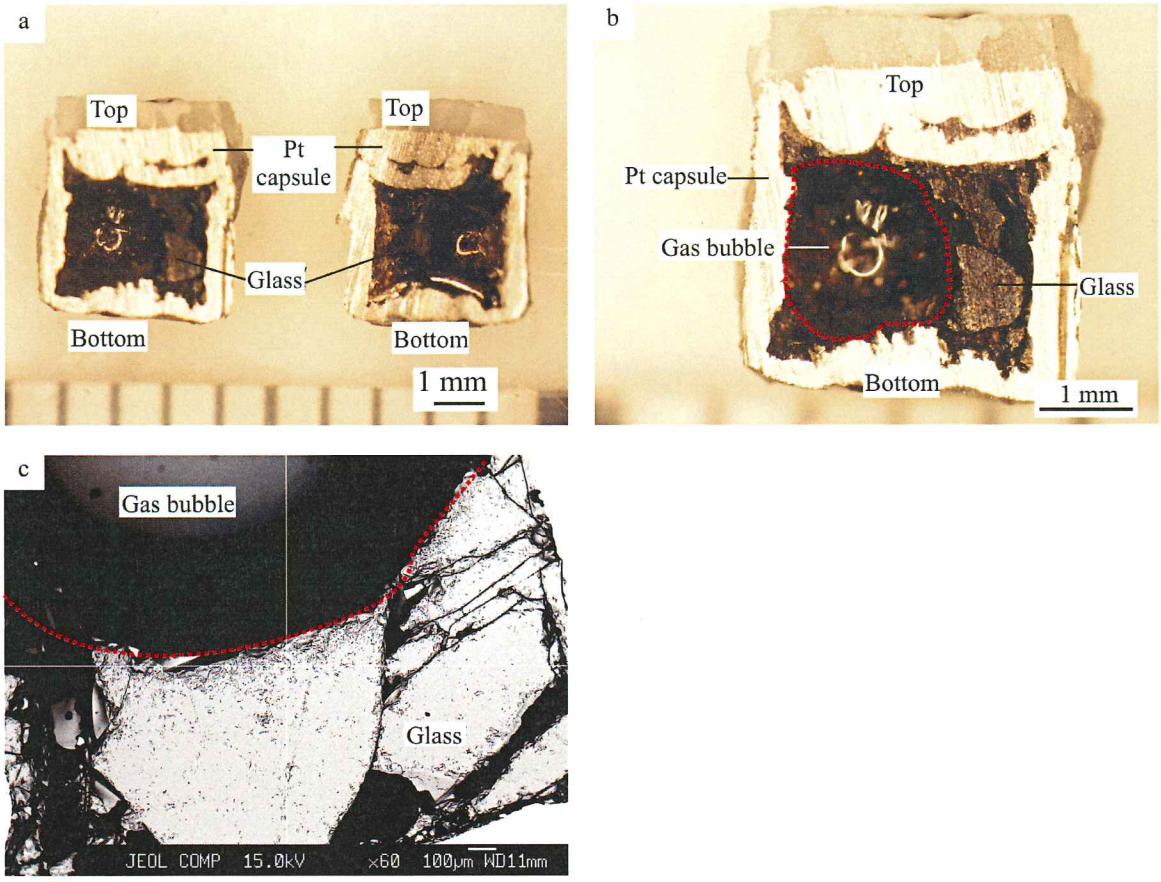

Figure 3.28 Images of experimental results of run PC-38, studying ilmenite in a diopside analogue with 27 wt% CO_2. a) The black glassy matrix. b) The black glassy matrix, and a large void caused by CO_2 in the run. c) Back-scattered image of the cell profile, showing the boundary between the glassy matrix, and the gas bubble.

3.4 Microprobe Analysis

Polished sections of the grain and matrix were analyzed using the electron microprobe (EMP). The analysis showed compositional changes that occurred in the grain and matrix during the experiments. This compositional change in the matrix accounted for the colour change observed in the experiments. Furthermore, this analysis also ensured that the wollastonite and diopside analogues were accurate. The raw data are given in Appendix C.

3.4.1 Matrix Composition

Several analyses, given in Table 3.1, were obtained for the matrix of each experiment, to ensure the matrix composition was consistent with the added oxides.

Table 3.1 Major-Oxide Composition of Experimental Matrix

	wt% CaO		wt% MgO		wt % SiO_2		total wt%	
Run	**Added**	**EMP**	**Added**	**EMP**	**Added**	**EMP**	**Added**	**EMP**
PC-29	25.90	27.47	18.62	17.34	55.49	55.19	100	100
PC-30	25.91	26.87	18.60	17.93	55.49	55.20	100	100
PC-32	25.90	25.69	18.62	16.64	55.49	57.66	100	100
PC-35	25.90	26.15	18.61	18.51	55.49	55.34	100	100
PC-37	48.27	48.93	-	-	51.73	51.07	100	100
PC-38	48.27	48.43	-	-	51.73	51.57	100	100
PC-39	25.91	26.24	18.60	18.31	55.49	55.45	100	100

** The 'added' column reports weight percentages according to the amount of each chemical added when the synthetic melts were made. The 'EMP' column gives the weight percentage of each oxide according to a microprobe analysis of the matrix after the run is complete.*

There was good agreement between the added and microprobe oxide weight-percentages, so the method used to make the matrices is satisfactory.

Experiments PC-38 and PC-39 were performed on ilmenite grains which were completely dissolved during the run. This was reflected in the composition of the glass. Experiment PC-38 yielded a matrix containing approximately 5.5 wt% FeO and 11.5 wt% TiO_2, and experiment PC-39 yielded a matrix containing approximately 2.0 wt% FeO and 4.1 wt% TiO_2. These oxides were not present in the initial synthetic matrix, so their contribution was entirely from the dissolved ilmenite grains.

3.4.2 Diffusion Profiles

The purpose of the graphs given in Figures 3.29-3.31 is to show how the major and minor element concentrations varied with distance from the chromite/matrix boundary. Therefore, chemical diffusion profiles were prepared for those experiments which had a polished section of matrix that contained the experimental grain. Three experiments were analyzed: PC-32, PC-35, and PC-37. These profiles were made from poor-quality EMP data, so trace elements were not included. The data is of sufficient quality to show concentration changes in major and minor elements. The data is poor quality because the polishing method was insufficient to achieve a totally level surface, and because the matrix consisted mainly of quench crystals that are difficult to analyze because they are small.

The chemical composition of chromite was significantly different than that of the silicate matrix, so their data were plotted on separate graphs. These two sets of data were further subdivided according to major and minor elements. The first point of the profile

was taken on the chromite grain, and an analysis was performed every 5 μm, going toward the matrix. On each graph x=0 μm represents the chromite/matrix boundary.

PC-32 Profile

Experiment PC-32 investigated dissolution of chromite in a matrix of diopside analogue with 13 wt% H_2O. The chemical profiles resulting from the microprobe analysis of this experiment are given in Figure 3.29. The chemical profiles showed that the chromite composition was variable only in the outermost 15 μm of the chromite. The compositional changes observed in this area were an increase in CaO, SiO_2, and MgO, and a decrease in FeO. Cr_2O_3 and Al_2O_3 remained relatively constant.

This was likely caused by the mixing of the diopside analogue ($CaMgSi_2O_6$) at the grain/matrix boundary, and the leaching of the major oxides of chromite into the matrix. It is possible that the mixing of the chromite and matrix at the grain boundary was an artefact. The microprobe beam excited an area with a diameter in excess of 3 μm, so while both phases may actually have been distinct, the electron beam may have excited a volume that included both the grain and matrix, causing signal mixing. Nonetheless, at distances greater than 15 μm from the grain/matrix boundary, the chromite grain was unaltered from its pristine composition.

The chemical profiles of the matrix show that there was no notable change in the major oxide composition based on distance from the grain. This was expected because the major oxide bulk composition was chosen to be diopside. As distance from the grain was increased, the concentration of FeO stayed the same, and the concentrations of Cr_2O_3 and Al_2O_3 decreased. Since chromite was the source of these metals, this decrease was

expected. The rapid decrease in concentration within the first 20 μm from the grain boundary indicated that these elements had low diffusivity.

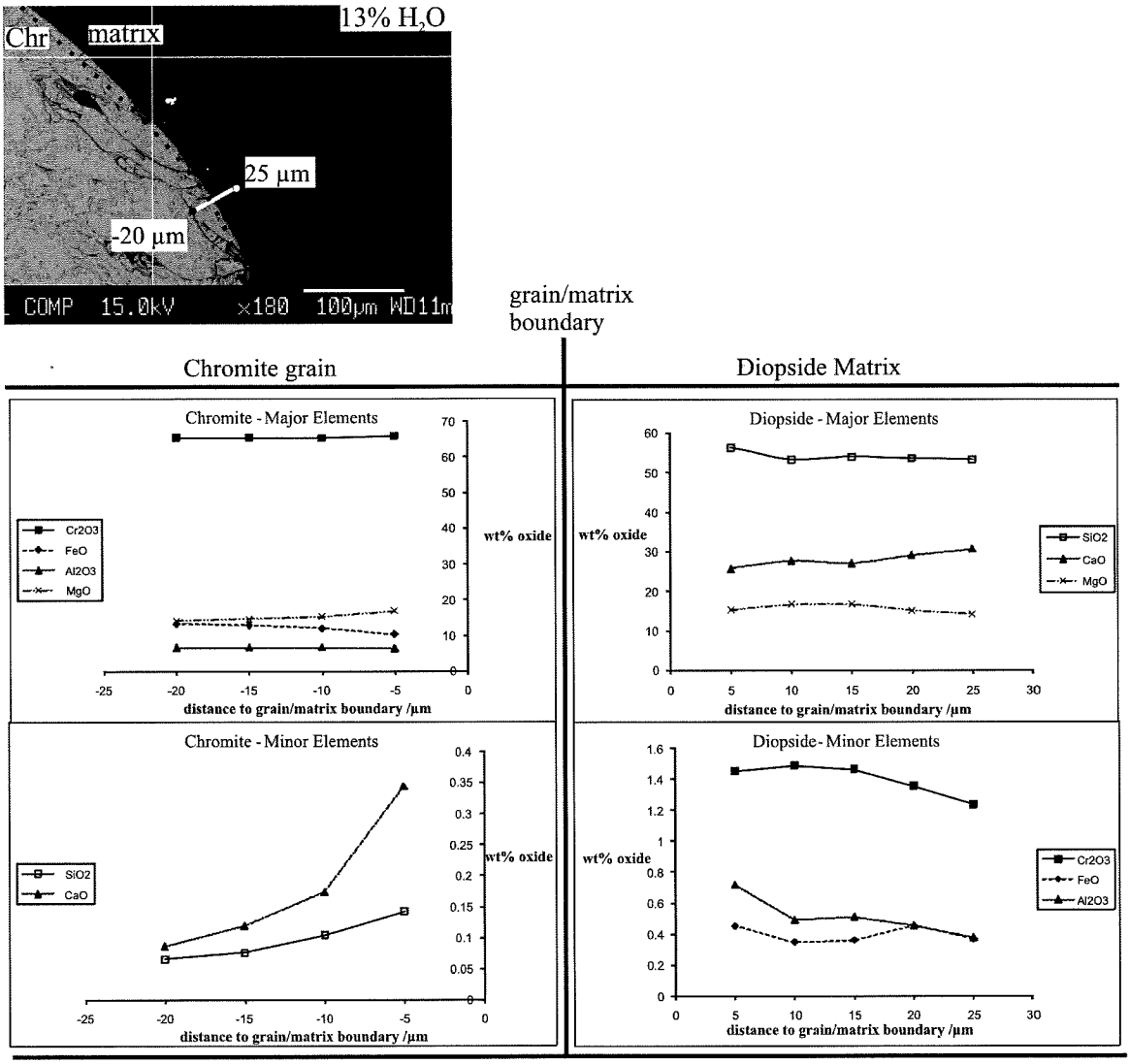

Figure 3.29 Diffusion profile of run PC-32: chromite in diopside analogue with 13 wt% H_2O. This figure shows the chemical changes in the grain and matrix in 5 μm intervals. The profile chosen started in the grain and ended in the matrix, and followed the white line in the back-scattered image at the top of the figure.

PC-35 Profiles

Experiment PC-35 investigated chromite dissolution in a melt of diopside analogue with 5 wt% CO_2. The chemical profile that resulted from the microprobe analysis of this experiment is given in Figure 3.30. The chemical profile indicated that the composition was highly variable in the outermost 15 μm of the chromite grain. This profile was similar to PC-32, in that there was an increase in CaO, SiO_2 and MgO, a decrease in FeO, and a constant amount of Cr_2O_3 and Al_2O_3 in the grain, as the grain/matrix boundary was approached. Again, this could be an artefact, or could be accounted for by mixing in the boundary region.

The chemical profile of the matrix was very similar to that of PC-32. There was no change in the major oxide composition based on the distance from the grain, for the same reasons mentioned previously. As distance from the chromite grain increased, the concentrations of FeO, Cr_2O_3 and Al_2O_3 decreased, which showed that these elements had low diffusivity.

PC-37 Profiles

Experiment PC-37 studies surface dissolution of chromite in a wollastonite analogue with 27 wt% CO_2. The chemical profiles resulting from the microprobe analysis of this experiment are given in Figure 3.31. The chemical profiles of the chromite show that the composition was highly variable in the outermost 10 μm of the grain. In this region SiO_2 and CaO concentrations increased, likely due to interaction with the $CaSiO_3$ melt. The dramatic increase in these oxides may indicate that dissolution of the chromite grain is more important and more rapid than diffusion. In this

region FeO, Al_2O_3 and Cr_2O_3 also decreased slightly, likely because of leaching of these metals into the matrix.

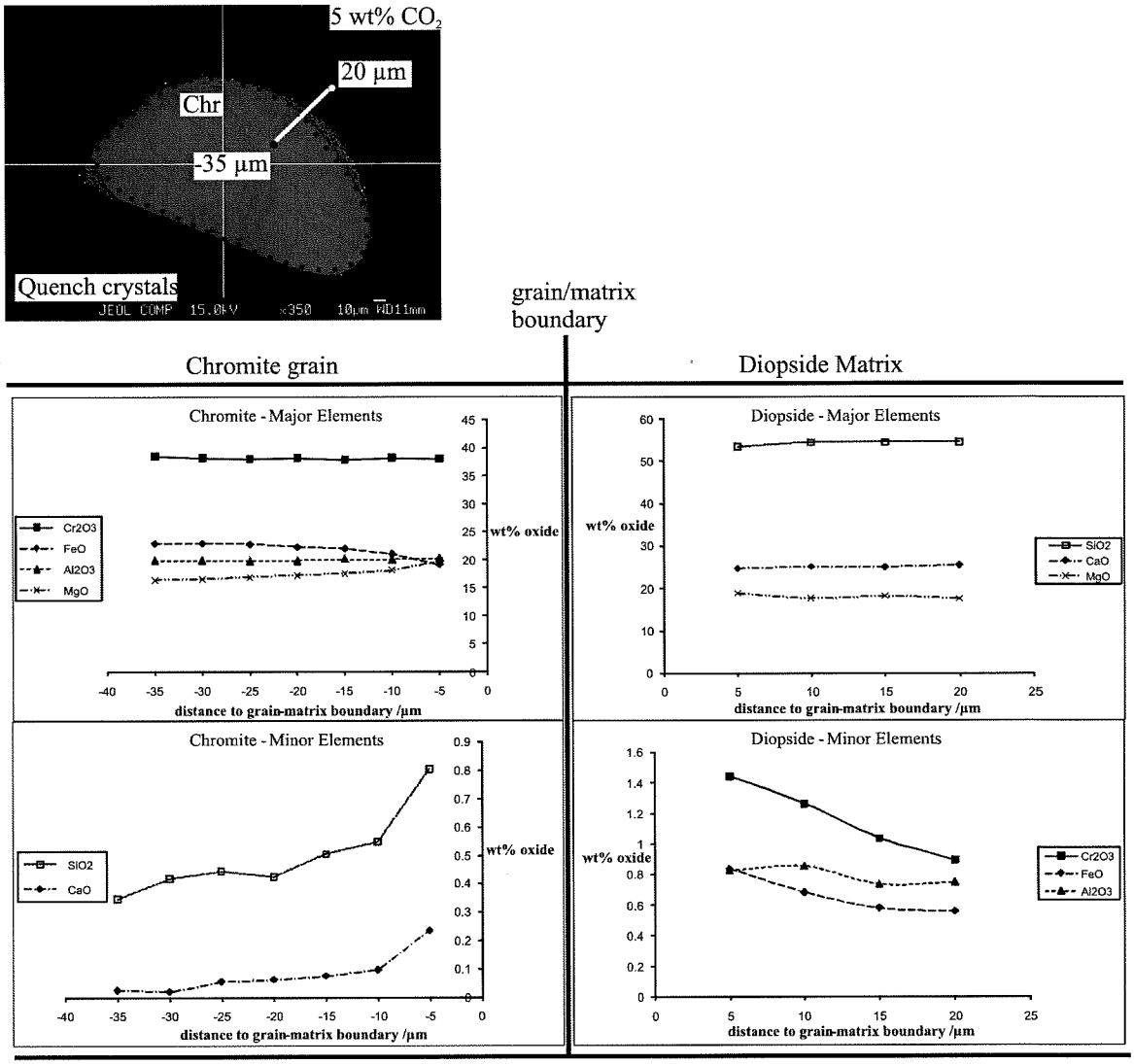

Figure 3.30 Diffusion profile of Experiment PC-35: chromite in diopside analogue with 5 wt% CO_2. This figure shows the chemical changes in the grain and matrix in 5 um intervals. The profile started in the grain and ended in the matrix, and followed the white line in the back-scattered image at the top of the figure.

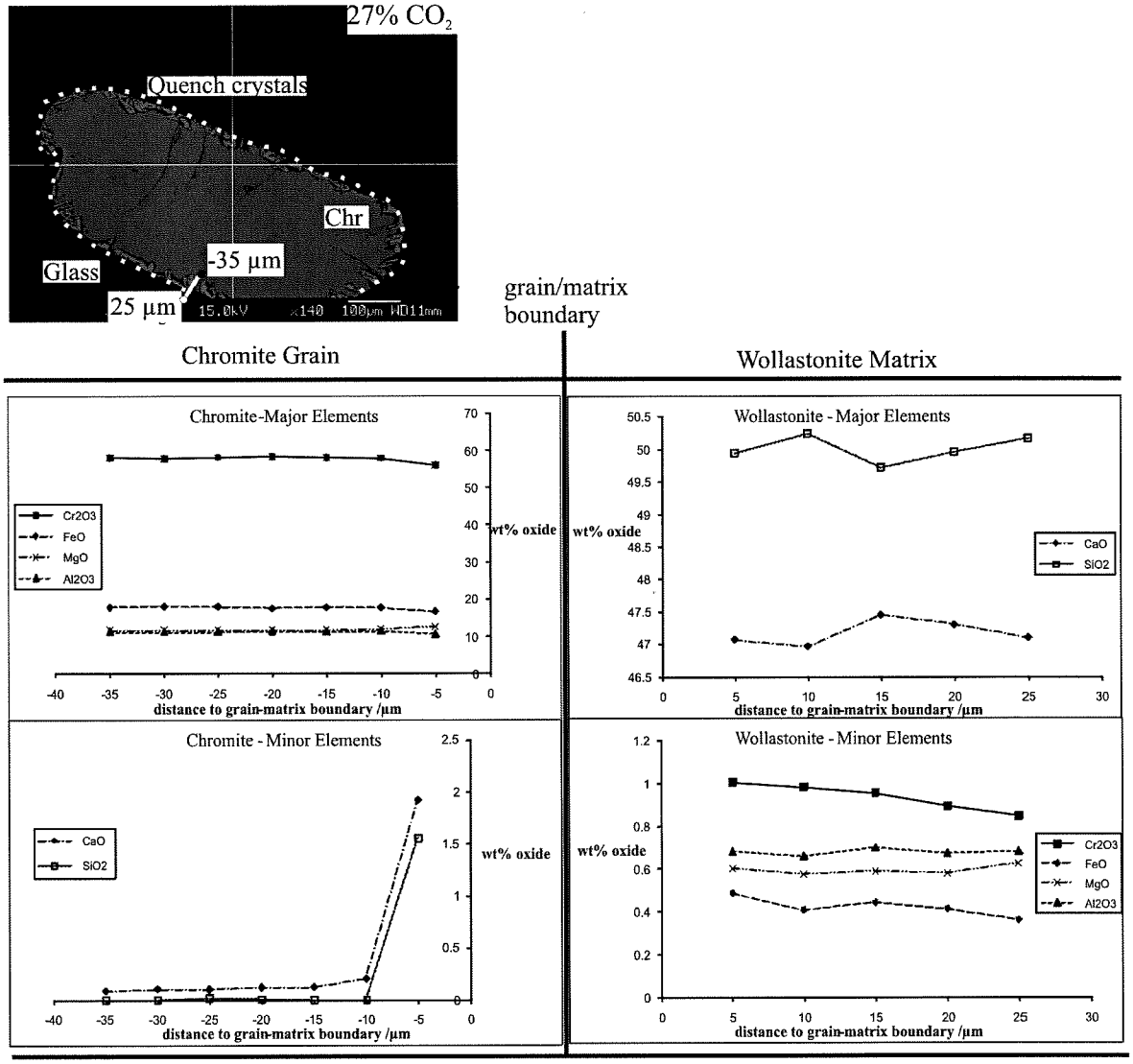

Figure 3.31 Diffusion profile of run PC-37: chromite in wollastonite analogue with 27 wt% CO_2. This figure shows the chemical changes in the grain and matrix in 5 um intervals. The profile started in the grain and ended in the matrix, and followed the white line in the back-scattered image at the top of the figure.

The major-element profile of the wollastonite analogue matrix showed moderate variability, but no overall increase or decrease in concentration of CaO or SiO_2. As distance from the grain increased, the concentrations of FeO and Cr_2O_3 decreased, showing that these elements had low diffusivity. There were no overall changes in the MgO or Al_2O_3 concentrations as distance from the grain was increased. The chromite hosted elements (Cr, Fe, and Al) showed very small decreases along the wollastonite profile, especially when compared to the diopside profiles. This indicated that these elements had a higher rate of diffusion at these experimental conditions.

The microprobe data proved that the interior of chromite, defined here as distances greater than 15 μm from the grain boundary, had a consistent composition. There was no notable compositional change in the grain during the experiments, indicating that there was dissolution with minimal exchange of material. Cr_2O_3, Al_2O_3, and FeO were leached from the outermost 15 μm of the grain, and diffused into the matrix. Table 3.2 gives the major-oxide composition of the unaltered grains, the amount of these oxides in the matrix at a point 15 μm from the grain boundary, and a ratio of these two numbers, giving the proportion of Cr_2O_3, FeO, and Al_2O_3 which diffused 15 μm after 1 hr at the conditions of interest. These values provide a better concept of the diffusivity of these elements.

Table 3.2 Matrix Content of Major Oxides in Chromite

		PC-32	PC-35	PC-37
wt% Cr_2O_3	in pristine chromite	65.52	37.91	58.19
	in matrix after 1 hr	1.46	1.03	0.95
	% leached	**2.24**	**2.73**	**1.64**
wt% FeO	in pristine chromite	12.79	21.99	17.87
	in matrix after 1 hr	0.36	0.58	0.44
	% leached	**2.82**	**2.63**	**2.47**
wt% Al_2O_3	in pristine chromite	6.51	20.13	11.26
	in matrix after 1 hr	0.51	0.73	0.70
	% leached	**7.80**	**3.65**	**6.18**

** Pristine chromite data points are taken -15 μm from chromite/diopside boundary. Matrix data points are taken 15 μm from chromite/diopside boundary.*

These values show that, regardless of the composition of the grain, and composition of the studied fluid, the proportion of the major oxides that leached from the chromite grain, into the surrounding matrix was relatively constant, with the exception of Al_2O_3 in experiment PC-35. Cr_2O_3 and FeO had low diffusivity, since after an hour at the conditions of interest, less than 3% of these metals diffused through a distance of 15 μm. The mobility of Al_2O_3 was slightly higher, since under the same conditions as much as 7.8% of the aluminium diffused the same 15 μm.

CHAPTER 4

DISCUSSION

This study examined natural surface features of chromite and ilmenite, and then used these grains in experiments to observe the dissolution features which resulted from interaction with specific fluid contents and compositions. An EMP analysis was used to track the chemical changes which occurred in the system, and an SEM was used to observe and image the surface features.

4.1 Chromite-Matrix Interaction

The three major oxides in chromite are Cr_2O_3, FeO and Al_2O_3. Al_2O_3 was the least abundant major oxide in the experimental grains examined using EMP, but had the highest proportional diffusion into the matrix (Table 3.2); Cr_2O_3 and FeO had lower diffusion rates from the grain into the matrix. The runs in diopside analogue showed slightly lower diffusion rates than those in wollastonite analogue, but further study is needed to confirm that this relationship is real.

It is likely that the fluids caused varying rates of dissolution. If the fluids caused the grain boundary to recede rapidly, matrix data points may have been taken in a spot that had originally been chromite. This could account for the small slopes in the diffusion profile of wollastonite, especially considering the high fluid content (27 wt% CO_2). More experiments need to be performed, and the length of the diffusion profiles needs to be increased to make firm conclusions concerning diffusion rates.

This analysis also examined how the matrix influenced the composition of the grain. The chemical profile of the grain showed that there was only appreciable mixing of the silicate matrix and the grain in the 15 μm closest to the grain boundary. This may have been an attempt of the system to reach maximum entropy by homogenizing the grain and matrix. Conversely, as described in the results section, this mixing may have been an artefact.

Regardless of the fluid content, the matrix for each experiment done with chromite was green, although the constituent oxides which went into the capsule were white. The colour change was indicative of a chemical change in the system. The most obvious chromophores in the system were the transition metals, which originated from the chromite grains. In these chromites, the only transition metals which occurred in major amounts were Fe and Cr. The other transition metals, Mn, Ni, Ti, and V, were present in trace amounts in the matrix, so it is unlikely that they contributed significantly to the colour of the system.

A literature review indicates that diopside becomes pale green above 1160°C, when chromium is high-spin and occupies octahedral sites (Ikeda and Yagi 1982). In diopside and in wollastonite, the chromophore replaces Ca^{2+} ions. Iron causes a yellow-brown colour in diopside, and a grey-pink or light-brown colour in wollastonite (Pogrebenkov et al. 1996). Also, chromium in diopside causes the diopside to turn green (Pogrebenkov et al. 1996). Although no UV-visible spectroscopic data was collected in this project, the colours observed suggest that chromium was the source of the color in the experiential matrix.

To confirm this, the transition metal content of the green and white areas of the matrix of experiment PC-37 was compared. The bar graph below displays the two analyses (Fig. 4.1). This graph shows that the transition metal content, especially chromium, was significantly higher in the green area than in the white area. This is a good indication that chromium was responsible for the colour observed in the matrix.

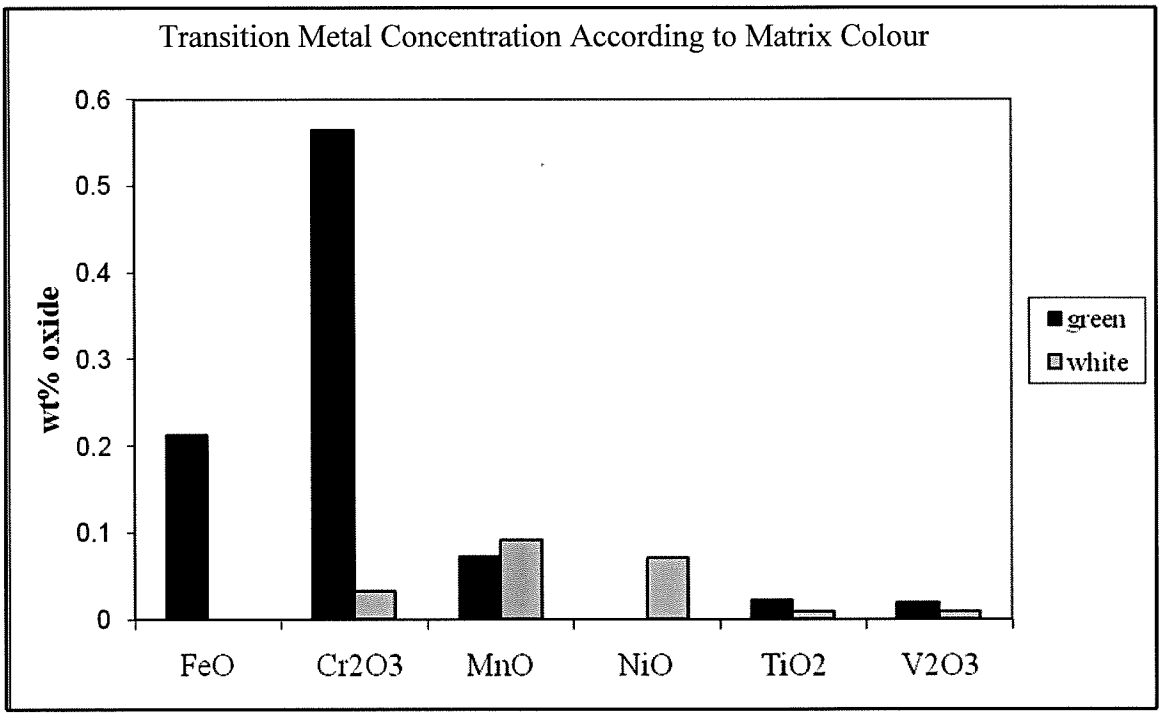

Figure 4.1 Weight percentages of transition metals in the white and green areas of the wollastonite analogue matrix in Experiment PC-37. PC-37 studies chromite in a wollastonite matrix plus 27 wt% CO_2.

4.2 Ilmenite Stability in Kimberlite Magmas

The microprobe analysis also confirmed that the ilmenite grains were totally dissolved during runs PC-38 and PC-39. Three sample points were analyzed using the EMP, from experiment PC-38. The FeO content for the three analyses ranges from 5.4-

5.8 wt%, and the TiO_2 content ranges from 11.4-11.7 wt%. Experiment PC-39 shows similar consistency between sample points. The homogeneity in the composition of the glass in these experiments indicated that the ilmenite grain dissolved rapidly under the specified conditions.

Although two of the experiments with ilmenite did not provide information regarding surface features, they were important for understanding the kinetics of these systems. The complete dissolution of these grains suggests that prolonged exposure to the conditions similar to the experimental pressure, temperature, and system composition is unlikely in a natural kimberlite, otherwise kimberlites would be barren of ilmenite. This may also suggest that chromite/H_2O-fluid interaction is most important at shallow levels.

Furthermore, these results have implications for previous diamond surface-feature studies. Diamonds are thought to be unstable in kimberlitic fluid, but they have been successfully studied at these conditions with only surface dissolution (Fedortchouk 2009. P. Comm). Because diamonds are actually much more stable than other minerals found in kimberlites, it is possible that their weight loss mostly happens in the mantle and not necessarily during kimberlite emplacement. Diamond surface features are still produced in the ascending kimberlite, and do not originate in the mantle.

The analysis of natural ilmenite grains from the Misery kimberlite showed no ubiquitous surface features, such as those expressed on the surface of chromite grains from the same pipe. The most common features on ilmenite grains from the Misery kimberlite were abundant lamellae (Fig. 4.2a), flaky surfaces (Fig. 4.2b), and

micropyramids (Fig. 4.2c). More natural ilmenites need to be analyzed to better understand the surface features present on natural grains, and what pressure, temperature, and fluid conditions these surface features may indicate in subsequent experiments.

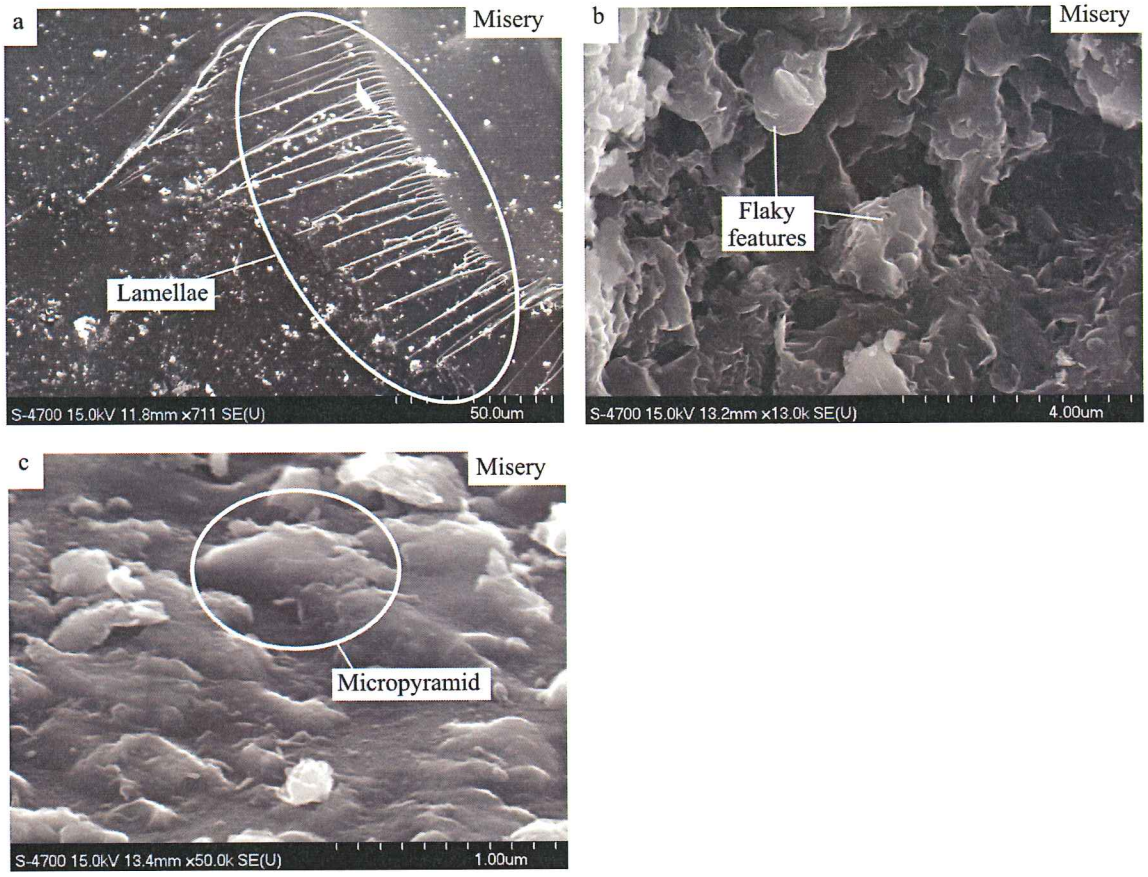

Figure 4.2 Naturally occurring dissolution surfaces in ilmenites from the Misery kimberlite a) Lamellae b) Flaky surface features. C) Micropyramidal features.

The grain in PC-42 may have been conserved because the MgO matrix was solid at the pressure and temperature conditions studied. The matrix formed euhedral crystals, which arose from solid-state recrystallization during the experiment. It may be necessary to have both a melt and a fluid present for mineral dissolution.

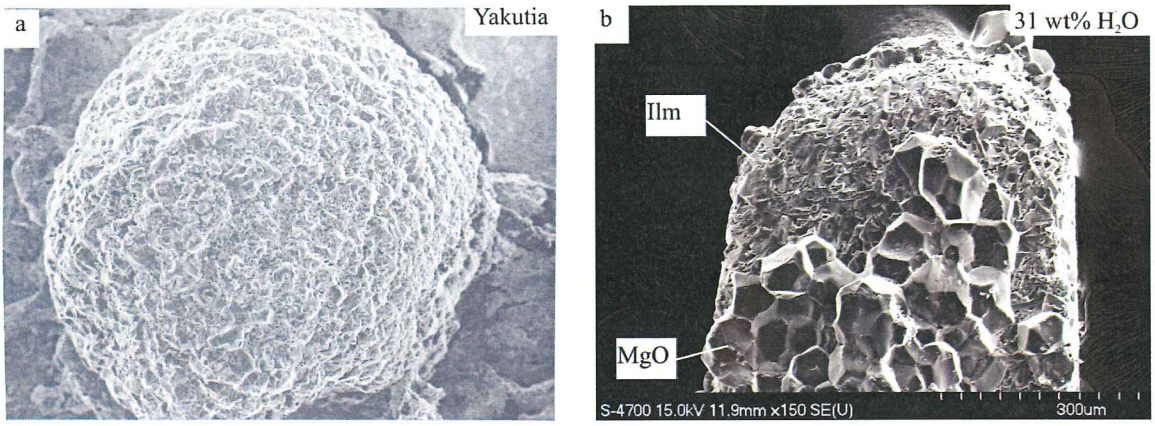

Figure 4.3 a) 75x view of a natural ilmenite grain, from the Yakutia kimberlite, showing an angular surface [reproduced from (Afanasiev et al. 2001)] b) Surface of experimental ilmenite, resulting from exposure to 31 wt% H_2O (PC-42), showing an angular surface.

Figure 4.3 compares the low-magnification surface features of the experimental grain, to surface-dissolution features exhibited on ilmenite from Yakutia kimberlite in Siberia (Afanasiev et al. 2001). Both ilmenite grains are angular and have poorly defined surfaces.

Some comparisons can be made between a natural ilmenite from the Yakutia kimberlite (Fig. 4.4a), the surface of an ilmenite from the Misery kimberlite (Fig. 4.4b), and the surface of the ilmenite resulting from experiment PC-42 (Fig. 4.4c). The common surface feature apparent on each grain is shaped like a pyramid. On the first image these features are large, and the author refers to them as "pyramids". On the following two images these features are on the order of 1 μm, so they are called "micropyramids".

The pyramidal shape is the dominant type of surface feature found on ilmenite, although significant variation in size is reported (Afanasiev et al. 2001). Since water-rich conditions created the micropyramidal surface features of PC-42, and the same type of

feature was expressed on the ilmenite from the Misery kimberlite, the Misery kimberlite may have been water-rich during the time of its emplacement.

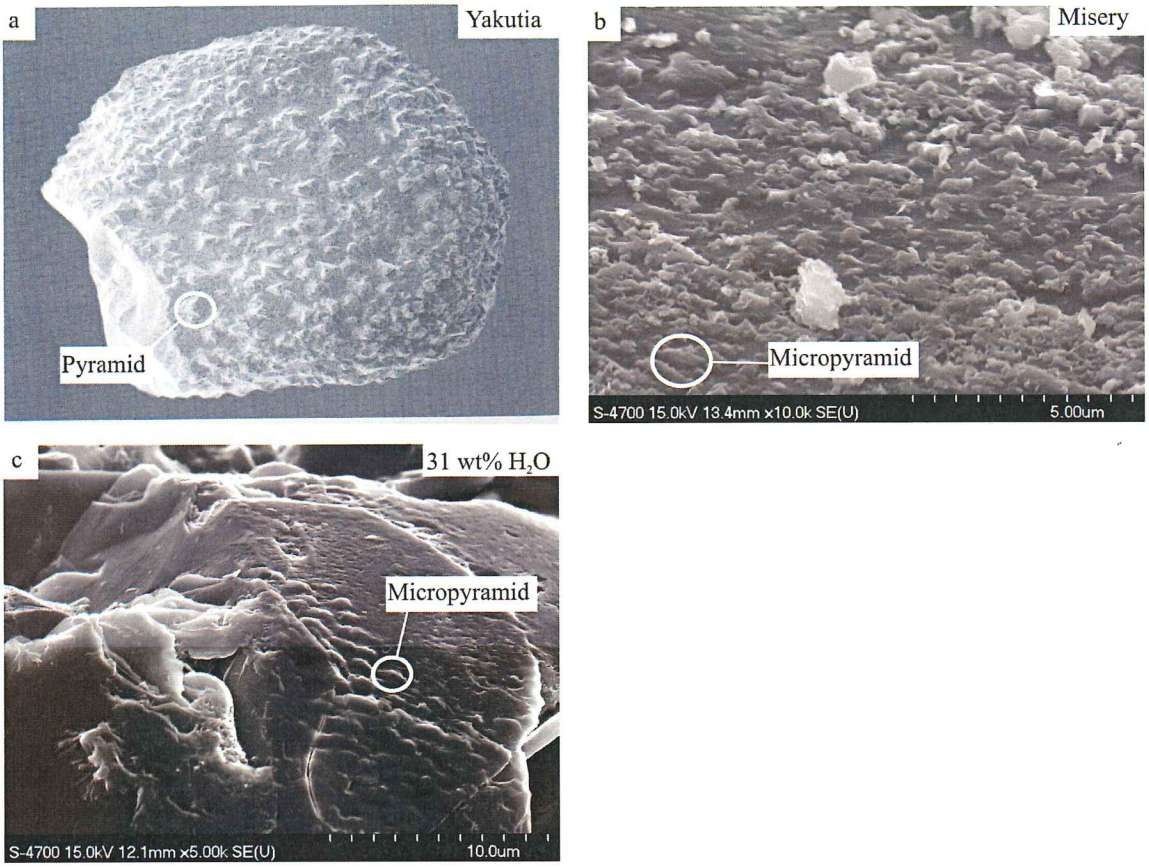

Figure 4.4 a) Image of natural ilmenite grain from Yakutia kimberlite, showing pyramidal surface features (75x). [Reproduced from (Afanasiev et al. 2001)] b) The surface of ilmenite grain R1aG7 from the Misery kimberlite, showing micropyramidal surface features c) Surface of experimental ilmenite, resulting from exposure to 31 wt% H_2O (PC-42), showing micropyamidal surface features

4.3 Dissolution Features on Chromite

4.3.1 Naturally Occurring Dissolution Features

Misery and Grizzly kimberlites were chosen for investigation of surface features on chromites because diamond data indicates that the Misery kimberlite had high fluid content at the time of emplacement, and that the Grizzly kimberlite had fluid loss at depth (Fedortchouk et al. 2008). Surface features of chromites from the Misery kimberlite were very consistent, and almost always triangular. Under high magnification, three types of surface features were observed: protruding triangles, shallow triangles, and triangular depressions. These three types of surface features are shown in Figure 4.5.

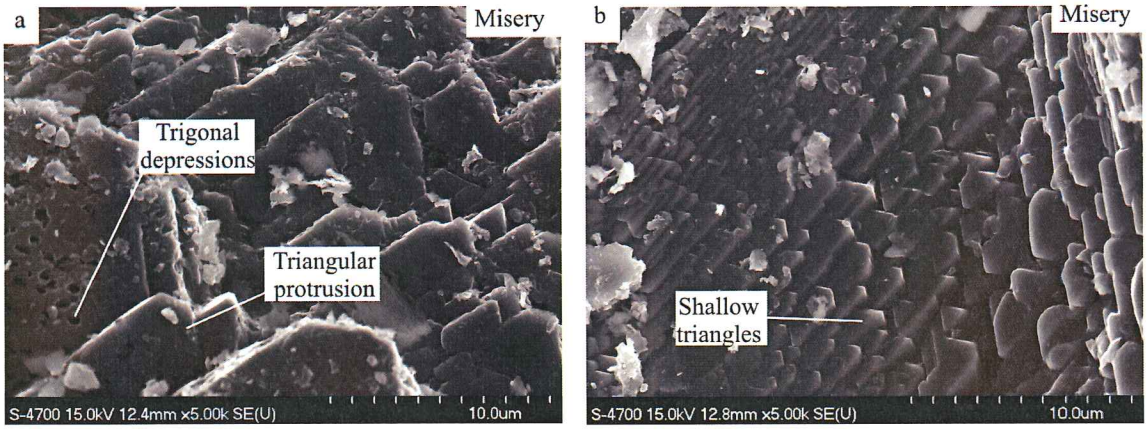

Figure 4.5 a) Image of natural chromite surface features, from the Misery kimberlite, showing trigonal depressions and triangular protrusions. b) Image of natural chromite surface features, from the Misery Pipe, showing shallow triangular features.

Chromites from the Grizzly kimberlite had surface features which were less ordered than those from the Misery kimberlite (Fig. 4.6). Angular surface features were almost entirely absent on these grains, and any surface features which existed were round or poorly formed. Experimental chromites exhibit the step-like features displayed on the surface of chromite grains from the Yakutia kimberlite in Siberia (Fig. 4.9).

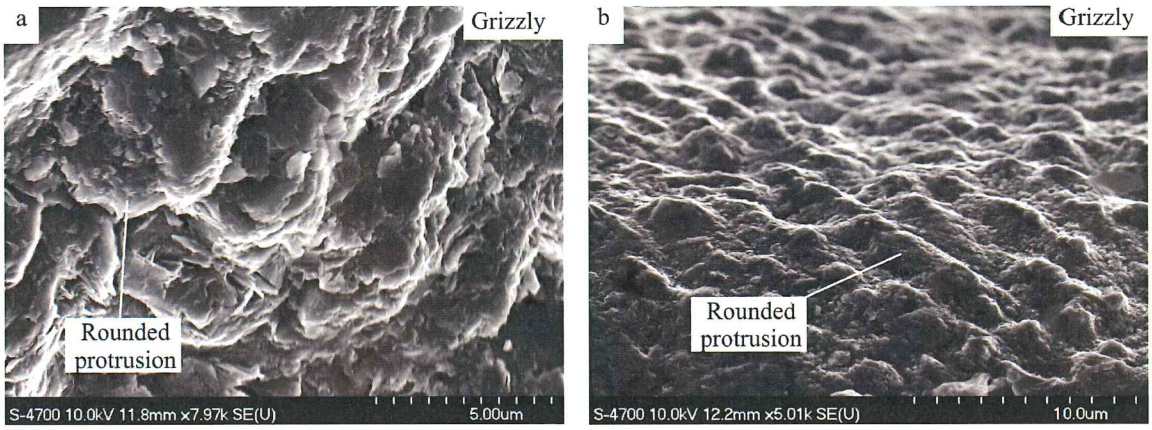

Figure 4.6 Image of natural chromite surface features from the Grizzly kimberlite. a) Rounded protrusions b) Rounded protrusions with a common orientation.

4.3.2 Experimental Dissolution Features

The interaction of CO_2 and chromite produced very interesting surface features. At 5 wt% CO_2 the surface was mostly smooth, but was covered in very fine linear-features and small nodules. Neither feature had an analogue on the natural chromite grains studied.

The effect of 27 wt% CO_2 on the surface features of chromite was also studied. The entire grain was covered in very small protruding polyhedrons. The polyhedrons were not observed on the natural grains from the Misery or Grizzly Kimberlites. Further work is needed to investigate intermediate fluid compositions of CO_2.

With increasing CO_2 content the proportion and regularity of the surface features increases. Through resorption, the polyhedrons have started to develop small crystal faces. These polyhedrons reflect the internal crystallography, and provide greater surface order, reflecting the internal crystal structure. If resorption causes the development of a few large crystal faces the surface energy will be greatly decreased. Further

investigations into natural kimberlites, and experimental runs with CO_2 may tell more about the effect of CO_2.

A schematic representation of the surface features produced in the CO_2 experiments is shown in Figure 4.7.

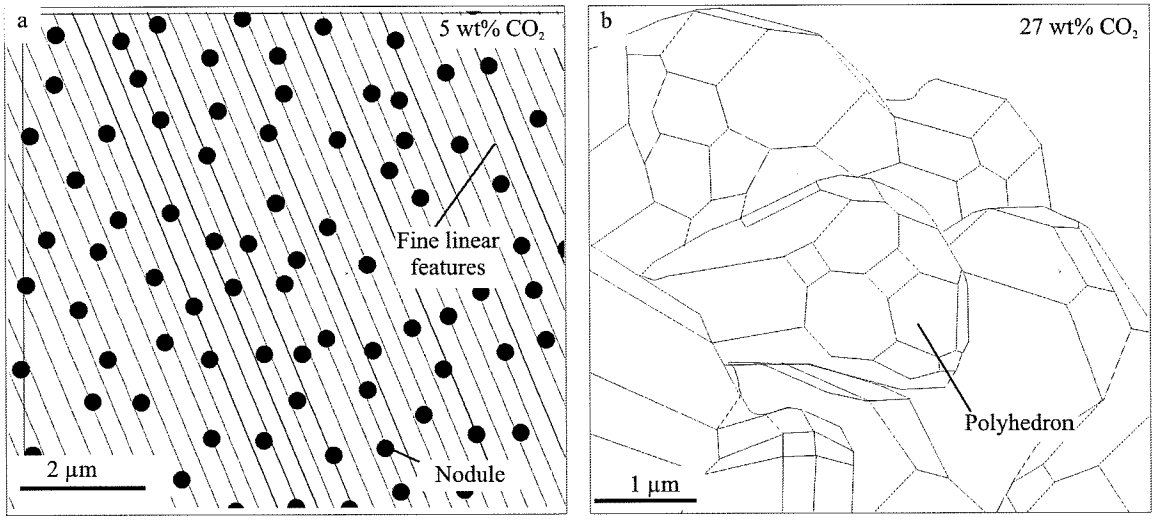

Figure 4.7 a) Schematic representation of the chromite surface resulting from PC-35, diopside analogue plus 5 wt% CO_2, showing fine linear features and nodules b) Schematic representation of the chromite surface resulting from PC-37, diopside plus 27 wt% CO_2, showing polyhedral on its surface.

Chromite dissolution features did not develop in a dry matrix of diopside analogue, suggesting that the surface features observed in experiments arose only from interaction with fluid or volatiles in the melt. Additional experiments are needed to confirm this, because the matrix in run PC-45 was not melted during the experiment, while the matrices in the other H_2O runs were melted.

When 5 wt% H_2O was added, sparse surface features appeared in the form of protruding, rounded trigons. As an increased proportion of water is added, at 13 and 15

wt% H_2O, the protruding trigons became increasingly angular and well ordered, and small trigonal depressions formed on the surface of the protruding triangles.

Figure 4.8 shows an interpretation of the surface features of chromite, based on the proportion of water in the melt. This figure shows clearly that triangular protruding surface features on chromite indicate exposure to H_2O. The natural surface features on chromites from the Yakutia kimberlite resemble the step-like chromite dissolution surfaces developed in run PC-32, from exposure to 13 wt% H_2O (Fig. 4.9).

It is proposed that the first step in the formation of the trigonal surface features is the development of flat wavy features. Figure 4.10a shows the development of these features at 5 wt% H_2O. These features may then develop more into wavy-step features, and then into rounded trigons. Fig. 4.10b shows these features developing together, at 5 wt% H_2O. With the addition of more water, these features may progress into linear steps and triangular protrusions. Figure 4.10c shows these features developing at 13 wt% H_2O. The triangular features are also expressed when the chromite is exposed to 15 wt% H_2O.

The morphology of the surface features on experimental chromites was dependent on the water content. Surface features became more abundant with increasing H_2O. Furthermore, surface features produced in a melt that contained dissolved water (5 wt% H_2O) produced rounded trigonal surface features, while melts that were equilibrated with free-H_2O fluid produced sharp, triangular surface features.

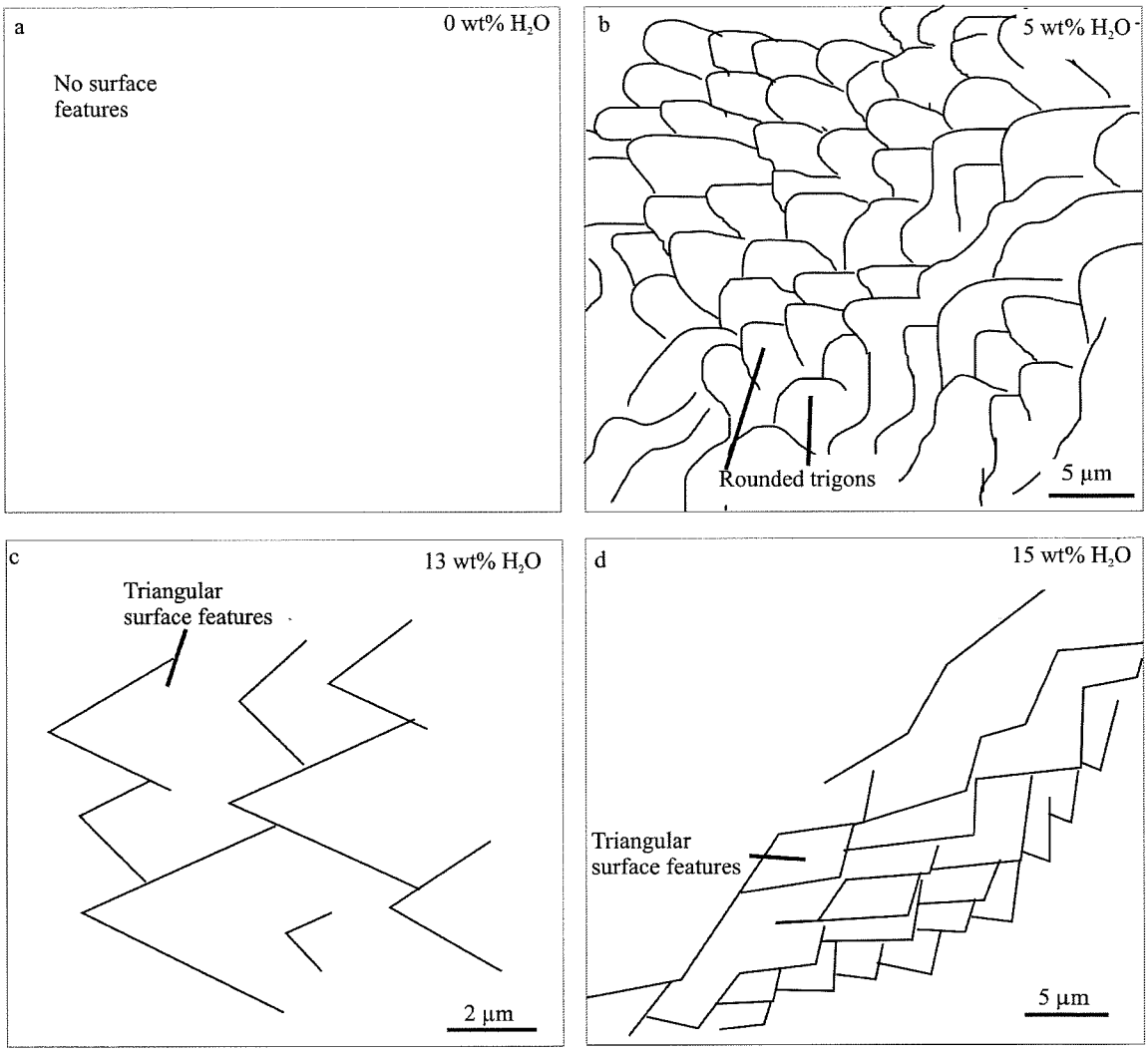

Figure 4.8 A schematic diagram showing how the shape of surface features of chromite change with increasing water content.

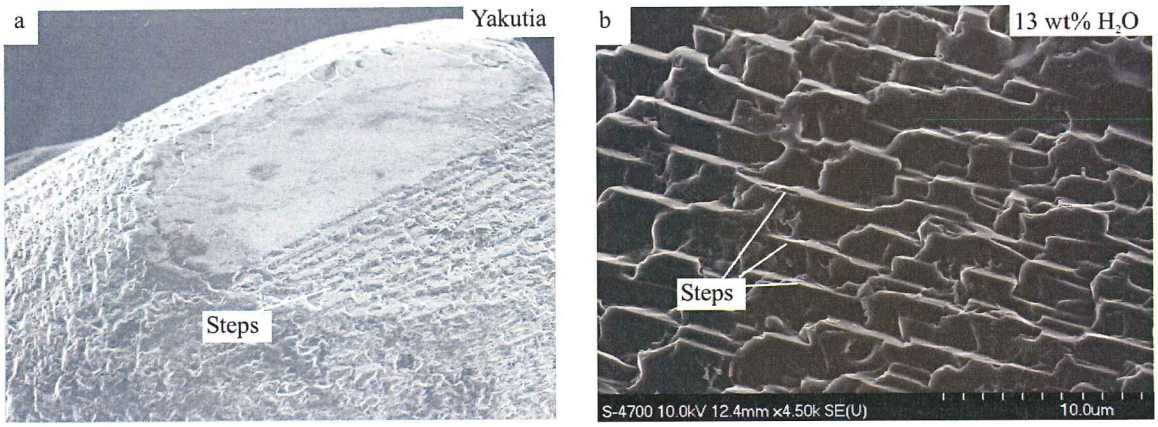

Figure 4.9 a) Angular step features on chromite (180x), from Yakutia kimberlite, from (Afanasiev et al. 2001) b) Angular step features on the chromite grain from Experiment PC-32, studying the effect of 13 wt% H_2O.

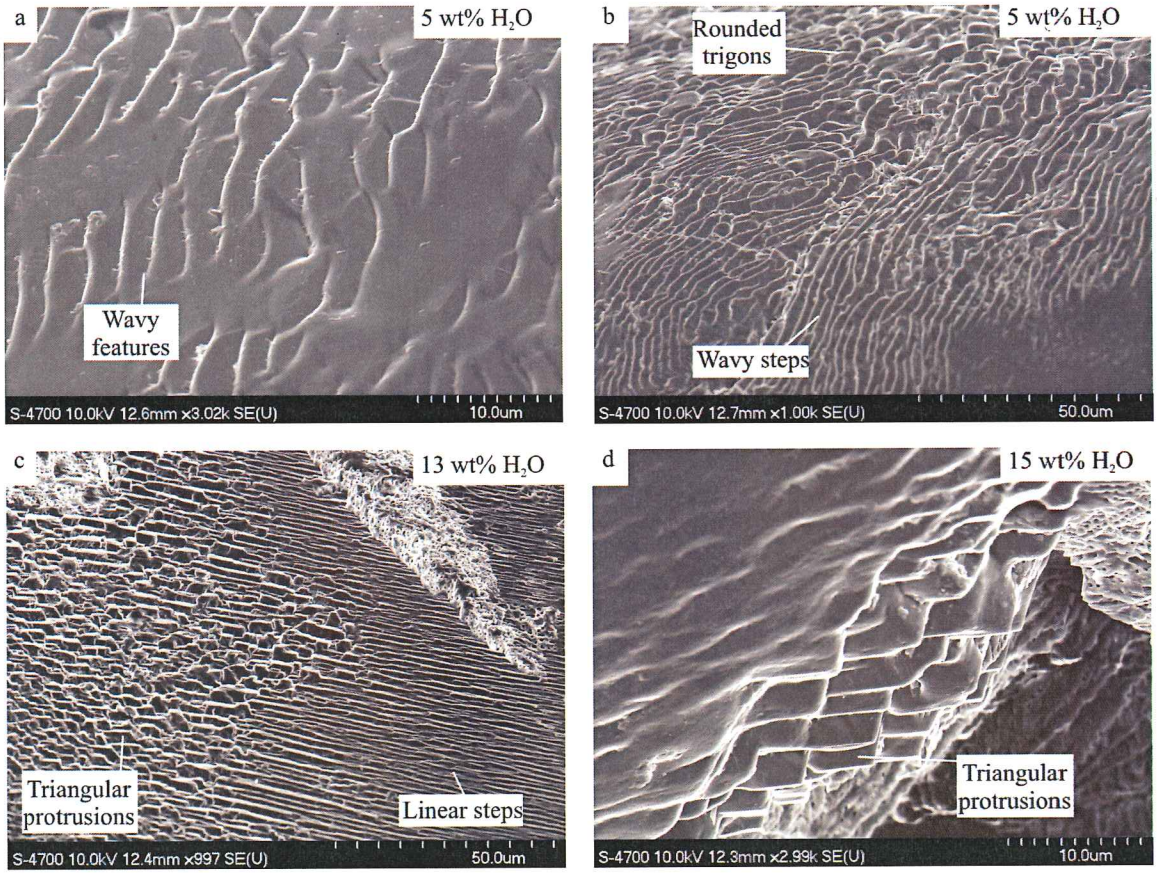

Figure 4.10 a) Flat, wavy features, developed at 5 wt% H_2O b) Wavy steps and rounded trigonal protrusions, developed at 5 wt% H_2O. c) Triangular protrusions, and linear steps developed at 13 wt% H_2O. d) Large triangular protrusions developed at 15 wt% H_2O.

4.4 Implications for the Fluid Systems of Kimberlite Magmas

The Misery kimberlite shows the same triangular surface features on chromite which are created in experiments that contained a free water phase. When chromite is examined without fluid dissolved in the melt or present as a free phase, or with CO_2 fluid, the surface features do not resemble any natural surface features. This indicates that the Misery kimberlite was water rich during emplacement, and the Grizzly kimberlite was water poor during emplacement. This inference agrees with previous studies of the fluid composition of the Misery and Grizzly Kimberlites. Diamond data indicates that the Grizzly kimberlite lost its fluid at depth, and the Misery kimberlite had high water content at the time of its emplacement (Fedortchouk et al. 2008).

Another method of determination of fluid content is the Fourier-Transform Infrared spectroscopic analysis of water in phenocrystic olivine (Matveev and Stachel 2007). Phenocrystic olivines in the Grizzly kimberlite have a much lower concentration of water than olivines from the Misery kimberlite (Fedortchouk et al. 2008).

Thus, two separate scientific methods corroborate the conclusion that the Misery Pipe was water rich, and the Grizzly Pipe was water poor at the time of emplacement.

The analysis of surface features of chromite from other diamond-bearing kimberlites has potential economic implications. The fluid content of kimberlites determines the resorption features on diamonds. Diamonds with low amounts of resorption features are desirable, and may be preferentially found in kimberlites with high water contents. In kimberlite, chromite is much more abundant than diamond, so the chromite surface features can be easily analyzed. Since chromite surface features

indicate water content, this method may provide a prediction of the grade of diamond which may be extracted from a kimberlite.

For example, the Grizzly kimberlite hosts diamond that exhibit severe surface etching affecting their quality. This is because the low fluid content caused a slow emplacement, providing the time necessary to make these surface features. The Misery kimberlite contains diamonds which are rounded and show minimal weight loss during emplacement. The preliminary results of this study suggest that kimberlites with chromites showing triangular protruding forms may have a large potential for containing high-quality diamonds, free of severe and intensive surface etching.

CHAPTER 5

CONCLUSIONS

5.1 Conclusions

1. Experiments that studied the effect of H_2O on chromite produced step-like and trigonal surface features that increased in angularity and order as the water content was increased. Highly angular and ordered surface features were produced in the presence of a free H_2O phase (*i.e.* when water composed 13 and15 wt% of the matrix/fluid system). Interaction with H_2O dissolved in the melt (5 wt% H_2O) produced rounded surface features, and interaction with dry diopside produced no surface features.

2. Experiments that studied the effect of CO_2 on chromite produced smooth surfaces at low CO_2 contents (5 wt % CO_2), and angular and polyhedral surface features at high CO_2 contents (27 wt% CO_2). During both experiments, there was a free CO_2 phase.

3. Natural chromite surfaces resemble experimental surface features from H_2O experiments, and do not resemble those from experiments in CO_2 fluid. CO_2 fluid caused angular polyhedral features to form on the surface of chromite. This indicates that the majority of kimberlites have a free H_2O fluid phase during the last stages of emplacement.

4. The correlation of experimental surface features with naturally-occurring dissolution surfaces on chromites from the Misery and Grizzly kimberlites

indicates that Misery had high H_2O content at the time of emplacement, and Grizzly had much lower H_2O content at the time of emplacement. This agrees with previous conclusions made using diamond data (Fedortchouk et al. 2008).

5. Ilmenite from the Misery kimberlite showed highly variable surface features at low and high magnification. Three types of surface features were visible at high magnification: micropyramids, lamellae, and flaky surfaces. The most common surface features were lamellae, and micropyramids. The experiment that studied the effect of 31 wt% H_2O on ilmenite reproduced the micropyramidal surface features found on natural ilmenite grains, suggesting that the Misery kimberlite was water rich during emplacement.

6. Ilmenite is very unstable in a silicate melt with CO_2 or H_2O fluid, when compared to the stability of diamond. Since all kimberlites have abundant ilmenite preserved, this study raises a question about how much diamond resorption occurs during ascent in kimberlite magma. This study suggests that diamond may be more stable during kimberlite ascent than previously thought, so natural diamond surface features may be acquired at greater depths, even during residence in the mantle.

7. The matrix in chromite experiments contained minor and trace amounts of transition metals that diffused from the grain. Of these elements, chromium had the highest concentration in the matrix. Other studies used UV-visible spectroscopy to determine that diopside and wollastonite with significant

chromium turn green (Ikeda and Yagi 1982; Pogrebenkov et al. 1996), accounting from the colour of the matrix in this study.

8. This study provides a new, preliminary method for kimberlite exploration; kimberlites with angular trigons and step-like features on chromites may indicate emplacement in fluid-rich conditions, which may lead to good quality diamonds, free from severe surface etching.

5.2 Future Work

A more detailed study of natural surface features of ilmenite is recommended. Parcels from other kimberlites, including more representation from Grizzly, should be examined for any regular surface features at high and low magnification. In addition, ilmenite should be examined at lower pressure and temperature conditions to provide a greater assessment of kinetic stability in kimberlitic melt. More fluid compositions should be examined at conditions where ilmenite shows kinetic stability, and these results can be compared to natural grains.

Additional H_2O experiments should be performed on chromite to constrain the transition from rounded-trigonal to triangular surface features. Also, CO_2 experiments should be expanded to examine the effect of intermediate concentrations, 10-20 wt%, on the surface of chromite. Since the CO_2 experimental features are not observed on natural grains, experiments should be performed containing both CO_2 and H_2O to see which type of surface feature dominates.

Chromite experiments should be performed at varying durations, to further explore the proposed development path of angular surface features, and to further examine the diffusion of metals from chromite into the silicate matrix.

It is recommended that chromites from other water-rich and water-poor kimberlites be examined to see if the predicted surface features are displayed. Heavy-mineral concentrates from diamondiferous kimberlites can be examined to see if triangular chromite surface features can be correlated with good diamond quality.

This method of study may also be expanded to other mantle indicator minerals found in kimberlites, such as garnet, to provide additional constraints on the fluid compositions during emplacement.

Afanasiev, V.P., Zinchuk, N.N., and Pokhilenko, N.P. 2001: Morphology and Morphogenesis of Kimberlite Indicator Minerals.*Edited by* N.V. Sobolev, Novosibirsk. pp. 95-139.

Boyer, J.S. 1995: Measuring the Water Status of Plants and Soils.*Edited by* Academic Press, Inc., San Diego. pp. 54.

Brearley, M., and Scarfe, C.M. 1986. Dissolution Rates of Upper Mantle Minerals in an Alkali Basalt Melt at High-Pressure - an Experimental-Study and Implications for Ultramafic Xenolith Survival. Journal of Petrology, **27**:1157-1182.

Canil, D., and Bellis, A.J. 2008. Phase equilibria in a volatile-free kimberlite at 0.1 MPa and the search for primary kimberlite magma. Lithos, **105**:111-117.

Canil, D., and Fedortchouk, Y. 1999. Garnet dissolution and the emplacement of kimberlites. Earth and Planetary Science Letters, **167**:227-237.

Dalton, J.A., and Presnall, D.C. 1998. The continuum of primary carbonatitic-kimberlitic melt compositions in equilibrium with lherzolite: Data from the system CaO-MgO-Al_2O_3-SiO_2-CO_2 at 6 GPa. Journal of Petrology, **39**:1953-1964.

Dawson, J.B. 1980. Kimberlites and Their Xenoliths. Springer-Verlag Berlin Heidelberg.

Eckstrand, O.R. 2002. March. Distribution of kimberlites worldwide in relationship to Archaean cratons. MINEX: Greenland Mineral Exploration Newsletter: No. 22. Geological Survey of Denmark and Greenland.

Edgar, A.D., Arima, M., Baldwin, D.K., Bell, D.R., Shee, S.R., Skinner, E.M.W., and Walker, E.C. 1988. High-Pressure High-Temperature Melting Experiments on a SiO_2-Poor Aphanitic Kimberlite from the Wesselton Mine, Kimberley, South-Africa. American Mineralogist, **73**:524-533.

Eggler, D.H., and Burnham, C.W. 1984. Solution of H_2O in Diopside Melts - a Thermodynamic Model. Contributions to Mineralogy and Petrology, **85**:58-66.

Fedortchouk, Y. 2009. P. Comm.

Fedortchouk, Y., Canil, D., and Semenets, E. 2007. Mechanisms of diamond oxidation and their hearing on the fluid composition in kimberlite magmas. American Mineralogist, **92**:1200-1212.

Fedortchouk, Y., and Hilchie, L. 2008. Unpublished Work.

Fedortchouk, Y., Matveev, S., Charnell, C., and Carlson, J.A. 2008. Kimberlitic fluid as recorded by dissolving diamond and crystallizing olivine phenocrysts in five Lac de Gras kimberlites, Northwest Territories, Canada. IXth International Kimberlite Conference: Extended Abstract.

Field, M., and Scott Smith, B.H. 1998: Contrasting geology and near-surface emplacement of kimberlite pipes in Southern Africa and Canada. Proceedings of the VIIth International Kimberlite Conference, University of Cape Town, South Africa 1:214-237.

Ikeda, K., and Yagi, K. 1982. Crystal-field spectra for blue and green diopsides synthesized in the join $CaMgSi_2O_6$-$CaCrAlSiO_6$. Contributions to Mineralogy and Petrology, **81**:113-118.

Kelley, S.P., and Wartho, J.A. 2000. Rapid kimberlite ascent and the significance of Ar-Ar ages in xenolith phlogopites. Science, **289**:609-611.

Kopylova, M.G., Matveev, S., and Raudsepp, M. 2007. Searching for parental kimberlite melt. Geochimica Et Cosmochimica Acta, **71**:3616-3629.

Matveev, S., and Stachel, T. 2007. FTIR spectroscopy of OH in olivine: A new tool in kimberlite exploration. Geochimica Et Cosmochimica Acta, **71**:5528-5543.

Mitchell, R.H. 1986. Kimberlites: Mineralogy, Geochemistry, and Petrology. Plenum Press, New York.

Mitchell, R.H. 1995. Kimberlites, Orangeites, and Related Rocks. Plenum Press, New York.

Mitchell, R.H. 1996a. Classificaion of undersaturated and related alkaline rocks. Pp. 1-22. Mineralogical Association of Canada Short Course Series: Undersaturated Alkaline Rocks: Mineralogy, Petrogenesis, and Economic Potential.

Mitchell, R.H. 1996b. The Orangeite Clan. Pp. 245-255. Mineralogical Association of Canada Short Course Series. Undersaturated Alkaline Rocks: Mineralogy, Petrogenesis, and Economic Potential Winnipeg.

Mitchell, R.H. 2004. Experimental studies At 5-12 GPa of the Ondermatjie hypabyssal kimberlite. Lithos, **76**:551-564.

Mitchell, R.H. 2008. Petrology of hypabyssal kimberlites: Relevance to primary magma compositions. Journal of Volcanology and Geothermal Research, **174**:1-8.

Pogrebenkov, V.M., Sedelnikova, M.B., and Vereshchagin, V.I. 1996. Ceramic pigments based on calcium-magnesium silicates. Glass and Ceramics, **53**:30-32.

Price, S.E., Russell, J.K., and Kopylova, M.G. 2000. Primitive magma from the Jericho Pipe, NWT, Canada: Constraints on primary kimberlite melt chemistry. Journal of Petrology, **41**:789-808.

Scott Smith, B.H. 1996. Kimberlites. Pp. 217-243. Mineralogical Association of Canada Short Course Series: Undersaturated Alkaline Rocks: Mineralogy, Petrogenesis, and Economic Potential.

Scott Smith, B.H. 2008. Canadian kimberlites: Geological characteristics relevant to emplacement. Journal of Volcanology and Geothermal Research, **174**:9-19.

Skinner, E.M.W., and Marsh, J.S. 2004. Distinct kimberlite pipe classes with contrasting eruption processes. Lithos, **76**:183-200.

Watson, E.B., Wark, D.A., Price, J.D., and Van Orman, J.A. 2002. Mapping the thermal structure of solid-media pressure assemblies. Contributions to Mineralogy and Petrology, **142**:640-652.

Winter, J.D. 2001. An Introduction to Igneous and Metamorphic Petrology. Pp. 363. Prentice Hall, Upper Saddle River, New Jersey.

APPENDIX A
ENERGY DISPERSIVE X-RAY SPECTRA: STARTING GRAINS

Misery Kimberlite Cr Spinel EDS spectra were collected using a JEOL 8200 electron microprobe, except R1bG2, which was collected using an Oxford Inca Energy Dispersive X-ray analysis system on a Hitachi S-4700 Scanning Electron Microscope. Grizzly Kimberlite EDS spectra were collected using an Oxford Inca Energy Dispersive X-ray analysis system on a Hitachi S-4700 Scanning Electron Microscope.

Grizzly kimberlite
Chromium Spinel

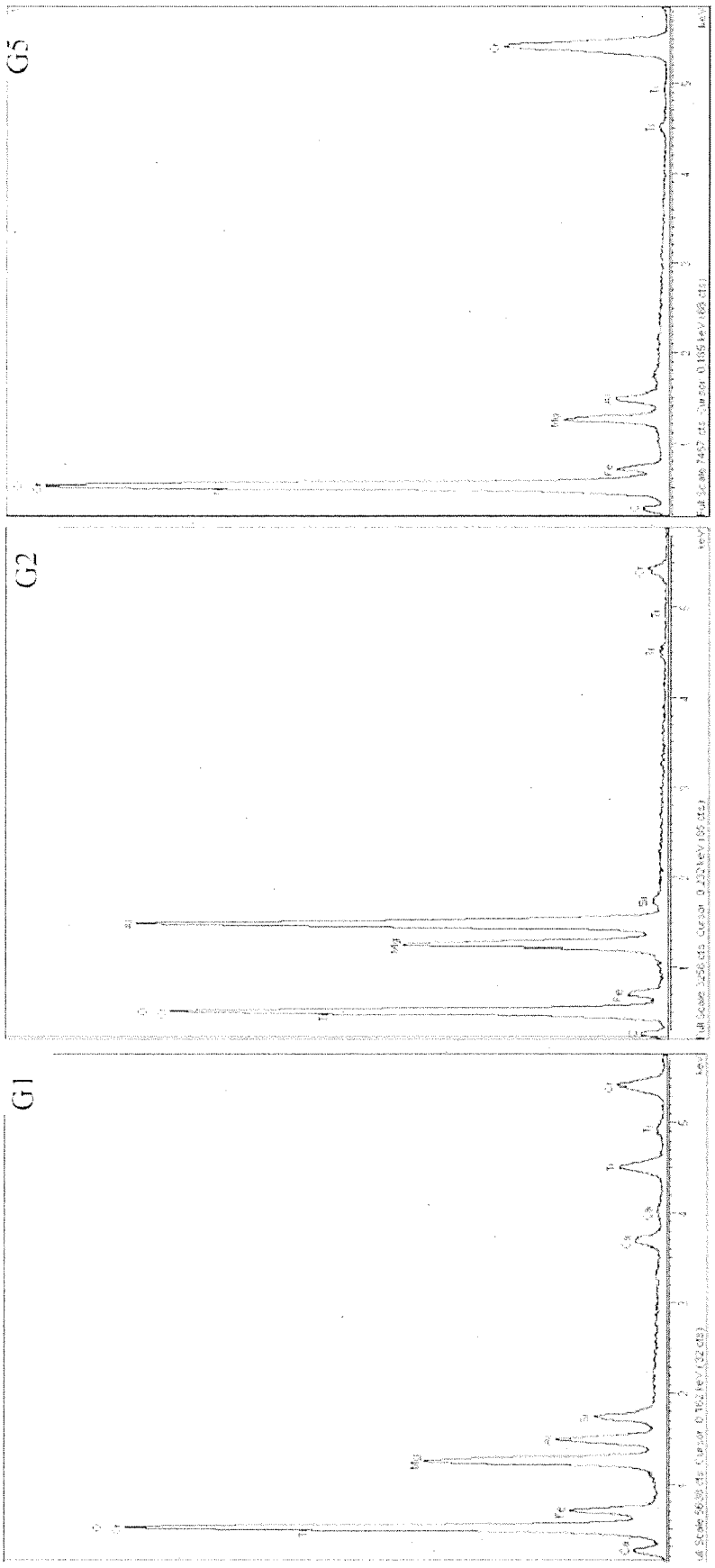

Misery Kimberlite
Group 1: high-chromium spinel

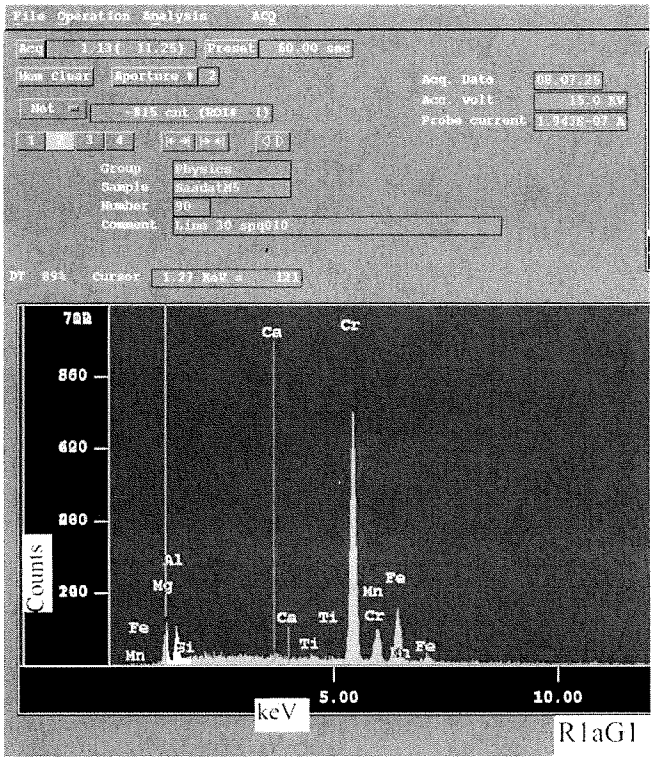

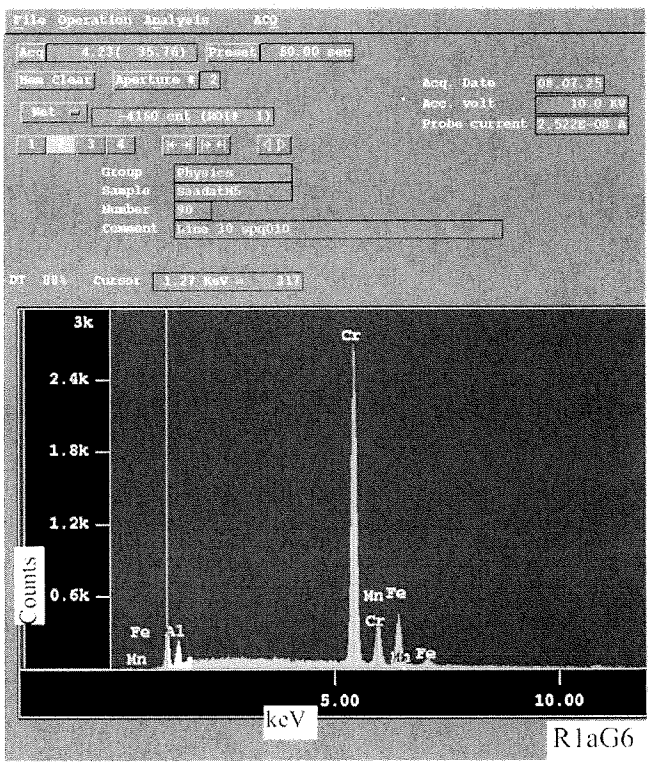

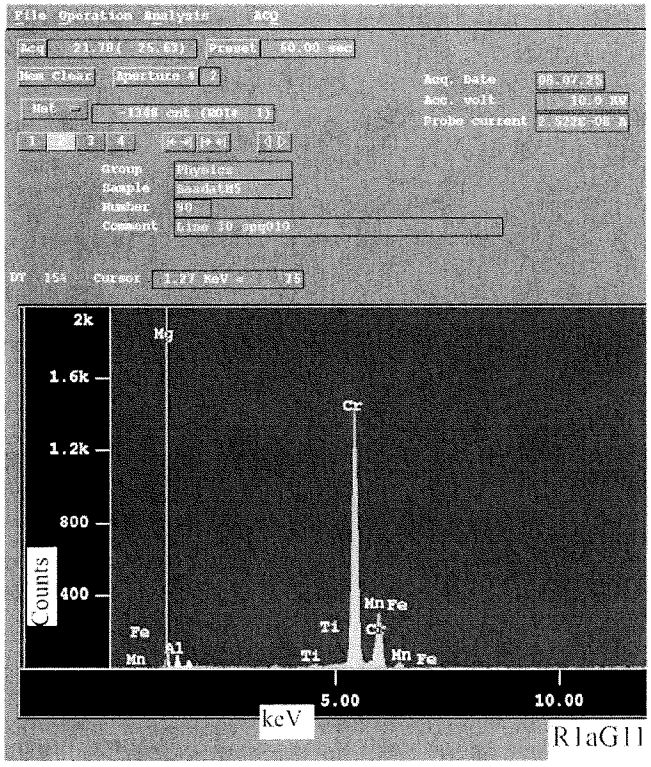

Group 2: medium-chromium spinel

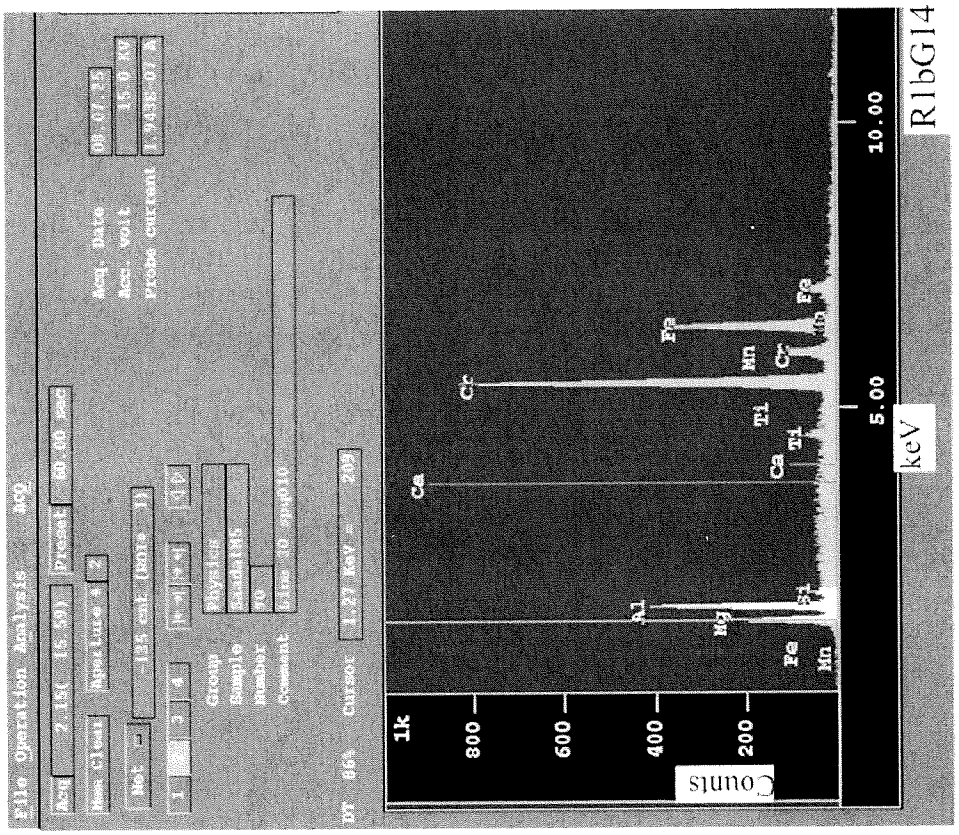

R1bG14

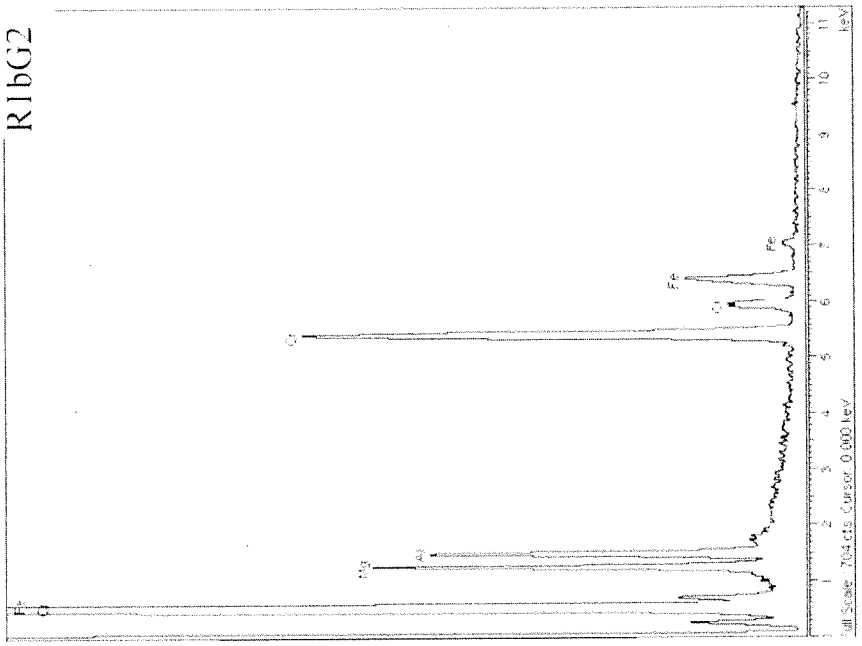

R1bG2

Group 3: low-chromium spinel

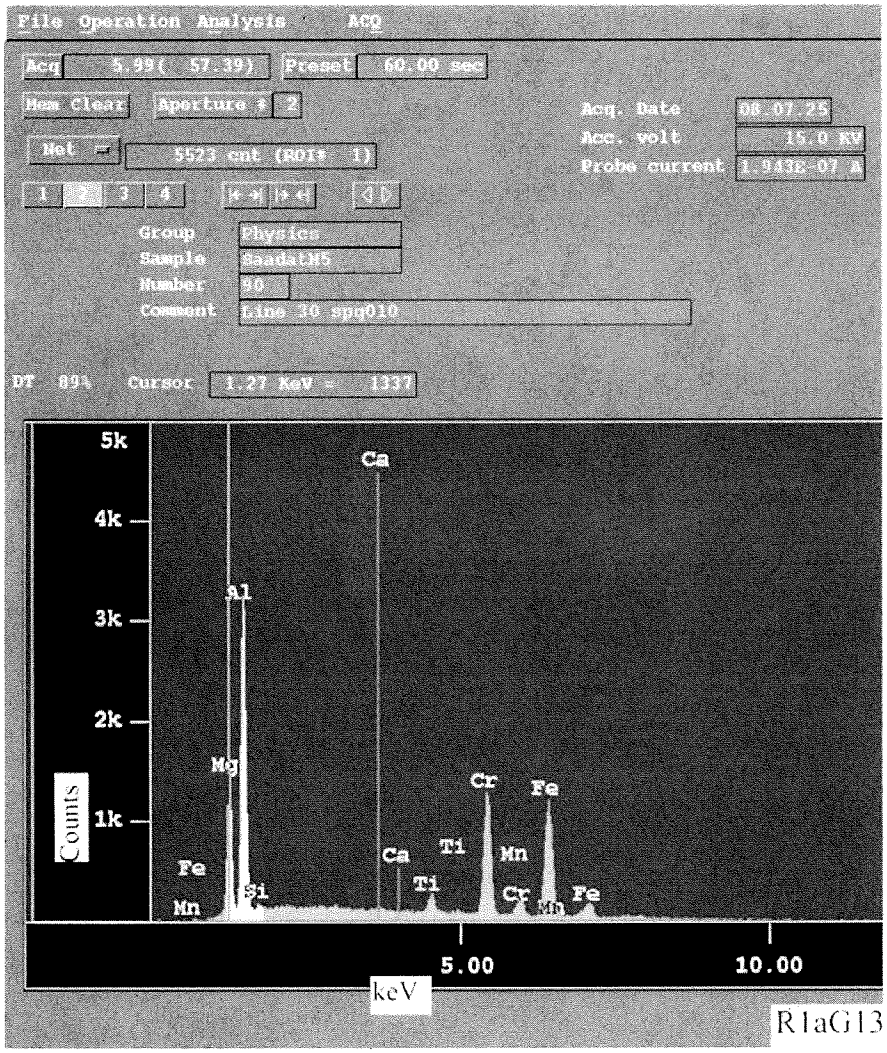

Ilmenite

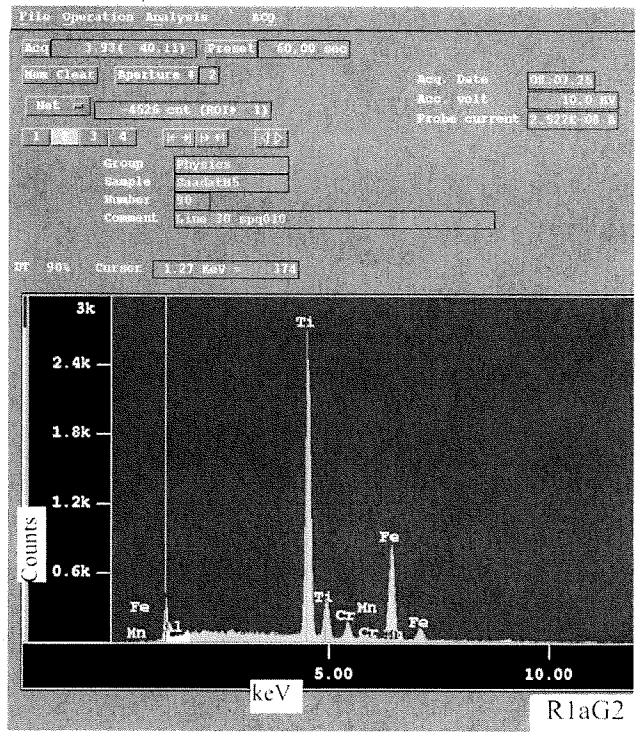

R1aG2

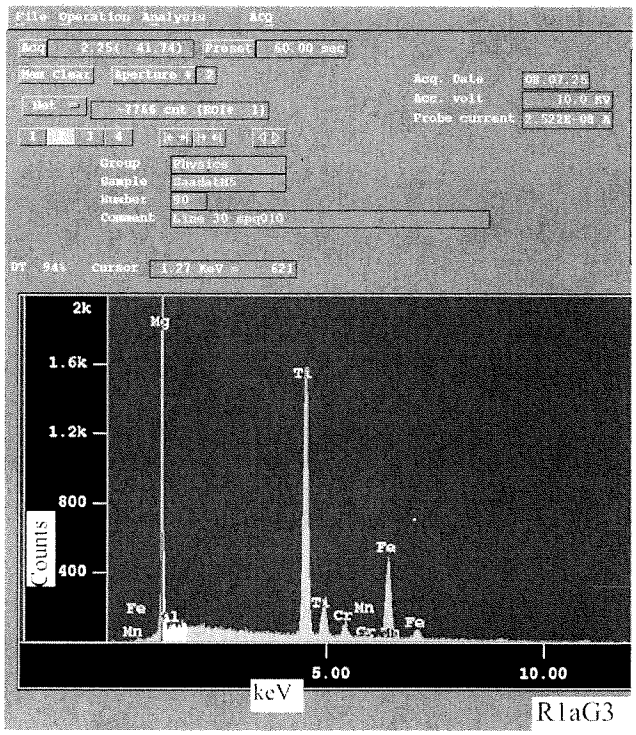

R1aG3

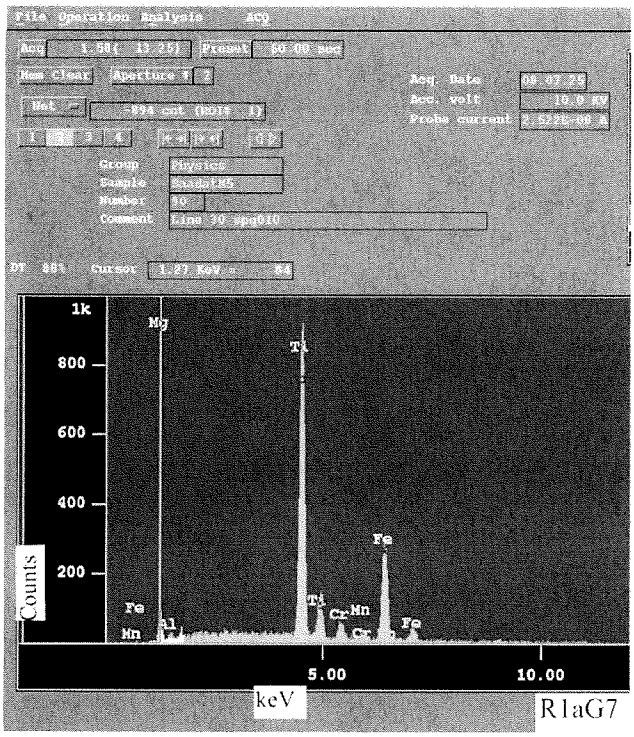

R1aG7

Appendix B: Electron Microprobe Standards

The silicate analysis used the following materials as standards:

Element	Material
Fe	Garnet12442
Cr	Cr_metal
Na	Jadeite
Al	Sanidine
Mn	Pyrolusite
Ca	K_kaersutite
Mg	K_Kaersutite
Si	Sanidine
Ni	Ni_metal
K	Sanidine
Ti	K_Kaersutite
V	V_metal

The silicate analysis uses an accelerating voltage of 15.0 kV, a 2 μm beam width, and a probe current of 1.998×10^{-8} A. The silicate analysis is not corrected for the V-Ti overlap.

The oxide analysis used the following materials as standards:

Element	Material
Fe	Pyrr_239
V	V_metal
Mg	Mg_metal
Si	Sanidine
Mn	Pyrolusite
Cr	Cr_metal
Al	Sanidine
Ti	Rutile
Ca	K_Kaersutite

The oxide analysis used an accelerating voltage of 15.0 kV, a 3 m beam width, and a probe current of 1.998×10^{-8} A. These analyses are corrected for the V-Ti and Cr-V overlaps.

APPENDIX C: MICROPROBE DATA

Nd- not detected
quench – quench crystals
xtals - crystalline

Table C1. Composition of Matrix

Run	FeO	Cr_2O_3	Na_2O	Al_2O_3	MnO	CaO	MgO	SiO_2	NiO	K_2O	TiO_2	V_2O_3	Total	phase	Analysis
PC-29	0.543	1.20	0.030	0.428	0.055	25.99	16.40	52.21	0.104	0.012	0.036	0.006	97.02	quench	61
PC-30	0.272	0.704	0.035	0.466	0.089	26.07	17.65	53.74	0.057	0.013	0.033	Nd	99.13	quench	63
PC-30	0.291	0.736	0.100	0.516	0.046	26.11	17.18	53.06	0.016	0.056	0.039	0.001	98.16	quench	65
PC_30	0.353	0.716	0.053	0.499	Nd	25.94	17.33	53.24	0.042	0.049	Nd	0.024	98.25	quench	70
PC_30	0.381	0.745	0.049	0.532	Nd	26.13	17.42	54.13	0.068	0.044	0.009	0.024	99.53	quench	71
PC-32	0.345	1.24	0.067	0.73	Nd	23.40	15.33	54.48	Nd	0.065	Nd	0.051	95.70	quench	21
PC-32	0.384	1.23	0.114	0.584	0.017	23.88	15.30	51.67	0.099	0.068	Nd	Nd	93.34	quench	19
PC-35	Nd	0.022	Nd	0.026	Nd	25.65	20.21	53.92	Nd	Nd	Nd	0.049	99.88	quench	1
PC-35	Nd	Nd	Nd	0.029	0.030	25.44	19.74	53.59	0.068	0.010	Nd	0.044	98.95	quench	2
PC-35	0.143	0.392	0.091	0.768	Nd	26.10	14.80	55.84	Nd	0.047	0.034	0.026	98.23	glass	8
PC-37	0.198	0.525	0.045	0.575	0.068	44.48	0.538	46.39	Nd	0.061	0.020	0.018	92.92	glass	44*
PC-37	Nd	0.033	Nd	0.011	0.093	50.03	0.182	52.09	0.073	Nd	0.009	0.009	102.53	xtals	45*
PC-37	0.004	0.016	Nd	0.014	0.068	49.39	0.132	51.73	0.119	0.011	0.002	0.024	101.50	xtals	46
PC-38	5.45	0.830	0.025	0.348	0.227	36.64	3.02	39.20	0.062	0.047	11.67	1.08	98.60	glass	51
PC-38	5.83	0.809	0.030	0.336	0.193	36.41	3.01	39.11	0.108	0.048	11.41	1.04	98.32	glass	52
PC_38	5.70	0.871	0.050	0.359	Nd	36.92	2.92	38.78	0.031	0.055	11.60	1.20	98.47	glass	77
PC-39	2.03	0.204	0.029	0.375	0.029	23.81	16.62	50.17	0.036	0.031	4.12	0.368	97.83	glass	55
PC-39	1.97	0.250	0.037	0.374	0.152	23.64	16.49	50.08	0.187	0.040	4.14	0.381	97.74	glass	57

**Data used in Figure 4.1: Transition Metal Concentration According to Matrix Colour*

Table C3. Compositional Profiles in Chromite from Run PC-37

Distance/ μm	FeO	V_2O_3	MgO	SiO_2	MnO	Cr_2O_3	Al_2O_3	TiO_2	CaO	Total	Analysis
-35	17.98	0.311	11.83	Nd	0.423	58.44	11.31	0.021	0.088	100.40	17
-30	18.24	0.342	11.84	Nd	0.419	58.25	11.28	0.050	0.110	100.53	18
-25	18.13	0.300	11.81	0.023	0.404	58.72	11.28	0.038	0.106	100.81	19
-20	17.66	0.351	11.83	0.007	0.334	58.62	11.36	0.053	0.124	100.34	20
-15	17.97	0.297	11.90	Nd	0.384	58.52	11.32	0.048	0.130	100.57	21
-10	17.82	0.263	12.14	0.003	0.349	58.39	11.50	0.047	0.209	100.71	22
-5	16.91	0.239	12.88	1.59	0.460	57.03	10.74	0.039	1.96	101.85	23

Table C4. Compositional Profile of Silicate Matrix from Run PC-37

Distance/ μm	FeO	Cr_2O_3	Na_2O	Al_2O_3	MnO	CaO	MgO	SiO_2	NiO	K_2O	TiO_2	V_2O_3	Total	Analysis
5	0.454	0.943	0.025	0.638	Nd	44.20	0.564	46.88	0.067	0.064	Nd	0.047	93.88	35
10	0.379	0.918	0.041	0.614	Nd	43.89	0.534	46.95	Nd	0.073	0.006	0.041	93.45	36
15	0.413	0.895	0.040	0.653	Nd	44.52	0.550	46.64	Nd	0.069	0.001	0.032	93.81	37
20	0.386	0.833	0.054	0.628	Nd	44.27	0.539	46.76	Nd	0.066	Nd	0.052	93.59	38
25	0.339	0.794	0.037	0.639	Nd	44.23	0.586	47.11	Nd	0.077	0.039	0.053	93.91	39

Table C5. Compositional Profile of Chromite from Run PC-32

Distance/ μm	FeO	V_2O_3	MgO	SiO_2	MnO	Cr_2O_3	Al_2O_3	TiO_2	CaO	Total	Analysis
-20	13.18	0.230	13.89	0.066	0.321	65.11	6.36	0.054	0.085	99.29	33
-15	12.73	0.220	14.40	0.077	0.260	65.19	6.47	0.042	0.118	99.50	34
-10	11.85	0.239	15.15	0.104	0.318	65.26	6.54	0.037	0.172	99.67	35
-5	10.00	0.193	16.60	0.140	0.210	65.07	6.15	0.023	0.339	98.73	36

Table C6. Compositional Profile of Silicate Matrix from Run PC-32

Distance/ μm	FeO	Cr_2O_3	Na_2O	Al_2O_3	MnO	CaO	MgO	SiO_2	NiO	K_2O	TiO_2	V_2O_3	Total	Analysis
5	0.411	1.33	0.045	0.657	nd	23.47	13.88	51.53	nd	0.075	nd	0.026	91.41	29
10	0.313	1.35	0.082	0.441	nd	24.98	15.01	48.21	nd	0.041	0.014	0.023	90.47	28
15	0.327	1.33	0.051	0.461	nd	24.46	15.06	48.97	nd	0.050	Nd	0.045	90.74	27
20	0.402	1.21	0.058	0.401	nd	25.81	13.39	47.71	0.010	0.053	Nd	0.030	89.07	26
25	0.329	1.11	0.047	0.334	0.009	27.36	12.61	47.66	0.078	0.034	0.008	0.014	89.59	25

Table C7. Compositional Profile of Chromite from Run PC-35

Distance/ μm	FeO	V_2O_3	MgO	SiO_2	MnO	Cr_2O_3	Al_2O_3	TiO_2	CaO	Total	Analysis
-35	22.91	0.339	16.41	0.347	0.204	38.61	19.93	1.34	0.025	100.11	1
-30	22.88	0.311	16.57	0.417	0.204	38.21	19.82	1.34	0.019	99.77	2
-25	22.92	0.307	17.06	0.448	0.240	38.45	19.98	1.43	0.056	100.89	3
-20	22.51	0.322	17.42	0.428	0.209	38.68	19.99	1.33	0.063	100.96	4
-15	22.33	0.317	17.83	0.512	0.177	38.50	20.44	1.36	0.076	101.54	5
-10	21.21	0.337	18.30	0.551	0.276	38.52	20.19	1.33	0.096	100.81	6
-5	19.45	0.311	20.16	0.820	0.170	38.87	20.64	1.27	0.238	101.93	7

Table C8. Compositional Profile of Silicate Matrix from Run PC-35

Distance/ μm	FeO	Cr_2O_3	Na_2O	Al_2O_3	MnO	CaO	MgO	SiO_2	NiO	K_2O	TiO_2	V_2O_3	Total	Analysis
5	0.865	1.49	0.057	0.850	Nd	25.43	19.36	55.30	Nd	0.001	0.103	0.062	103.52	13
10	0.699	1.30	0.088	0.873	Nd	25.73	18.01	55.94	Nd	0.023	0.064	0.044	102.76	12
15	0.602	1.07	0.054	0.763	Nd	25.91	18.75	56.57	Nd	0.009	0.053	0.041	103.83	11
20	0.572	0.915	0.121	0.767	Nd	26.22	17.95	56.19	Nd	0.036	0.061	0.041	102.87	10